THESIS

AIR CONCENTRATION AND BULKED FLOW ALONG A CURVED, CONVERGING STEPPED CHUTE

Submitted by

Blake W. Biethman

Department of Civil and Environmental Engineering

In partial fulfillment of the requirements

For the Degree of Master of Science

Colorado State University

Fort Collins, Colorado

Spring 2020

Master's Committee:

Advisor: Robert Ettema

Co-Advisor: Christopher Thornton

Ellen Wohl

ABSTRACT

AIR CONCENTRATION AND BULKED FLOW ALONG A CURVED, CONVERGING STEPPED CHUTE

This thesis focuses on the air-entrainment performance of a stepped spillway of unique form. The performance was determined using a hydraulic model constructed at a length scale (prototype length/model length) of 24. The new stepped spillway is part of the Gross Reservoir Expansion (GRE) project, which by 2025 is expected to raise the existing Gross Dam about a third of its current height. The stepped spillway will be the tallest stepped spillway in the United States. The model spillway consisted of a chute whose step dimensions, vertical to horizontal, were 0.051 m by 0.025 m, resulting in a chute slope (V:H) of 2.0 and a chute angle of 63.4°. Additionally, the chute conformed, in planform, to the curved planform of raised Gross Dam. At the spillway's crest, that radius of curvature, at model scale, was 22.2 m. The chute width converged by about 20% from the top of the chute to the stilling basin at the base of the chute. The chute's steepness, height, curvature and convergence made the chute's geometry unique among existing stepped spillways.

The evaluation involved measurements of air entrainment and flow velocity along the stepped chute, for which the skimming flow regime prevailed for discharge larger than about 9% of the spillway's design discharge. To date, the effect on water flow and air entrainment of chute curvature in stepped spillways had not been investigated. The investigation was facilitated from measurements obtained using a dual-tip conductivity probe, which detected the instantaneous

void fraction of the air-water mixture. The probe also enabled measurement of the velocity of the bulked flow along the chute.

The study showed that, when the chute conveyed the design discharge (at model scale, 0.347 m^3/s), streamwise values of air concentration and flow depth (bulked with entrained air) were basically constant near the bottom of the chute. Additionally, the chute's planform curvature resulted in non-uniform flow across the chute. At the design discharge, and near the bottom of the chute, the flow depth along the chute's centerline was nominally about 30% greater than the flow depth at the sidewall. When the chute's curvature was accounted for, the water surface along the centerline of the chute was approximately level with the water surface near the sidewall. Further, the depth-averaged concentration of entrained air near the bottom of the chute decreased with increasing water discharge. The chute's converging sidewalls mildly affected the flow near the sidewalls, causing slight increases in flow depth and reductions in flow velocity. These changes, though noticeable, were negligible in terms of spillway performance because of their magnitude.

ACKNOWLEDGEMENTS

The research conducted as part of this thesis would not have been possible without the support and mentorship of my advisor and co-advisor, Drs. Robert Ettema and Christopher Thornton, to whom I am most grateful for giving me the opportunity to participate in the hydraulic model study of the Gross Dam spillway. Additional thanks are given to the laboratory staff at the ERC for their expertise and assistance. I am thankful for the funding provided by Denver Water, and to those individuals with whom I worked during the completion of this work: Dr. Ed Kempema, Ali Reza Nowrooz Pour, Alireza Fakhri, Selina Tasdelen, Taylor Hogan and all other graduate- and undergraduate-staff at the ERC. Thanks, also, to Dr. Ellen Wohl for serving on my committee. Finally, a special thanks to my friends and family for their love and support during my graduate studies.

TABLE OF CONTENTS

LIST OF TABLES

LIST OF FIGURES

LIST OF SYMBOLS

θ	angle of chute inclination with respect to the horizontal
δ	boundary-layer thickness
γ	specific weight of water
τ	bed-shear stress
ρ	density of water
ν	kinematic viscosity of water
σ	surface tension of water
b	chute position measured from right sidewall
B	local chute width (from left to right sidewall)
C	volumetric air concentration
$\bar{C}$	depth-averaged air concentration
$\bar{C}_e$	depth-averaged, equilibrium air concentration
d_c	critical flow depth
f	Darcy-Weisbach friction factor
F_*	roughness Froude number
F_r	Froude number
g	gravitational acceleration
h	vertical step dimension
k_s	step roughness height
l	horizontal step dimension
L_i	crest-relative length to incipient aeration

L_r	length-dimension ratio of prototype to model scale
R_e	Reynold's number
q	unit discharge
Q	volumetric discharge
T_w	a sub-interval over which data are averaged
V	bulk-flow velocity
V_w	equivalent clear-water flow velocity
Q	volumetric discharge
W_e	Weber number
x	longitudinal downstream distance from the crest
Y	flow depth measured normal to the chute invert
Y_c	critical flow depth
Y_w	equivalent clear-water flow depth
$Y_{0.90}$	the flow depth where $C = 90\%$
z	the vertical axis

1 INTRODUCTION

1.1 Motivation

This thesis concerns the hydraulic and air-entrainment performance of a unique, ungated stepped spillway. The performance was determined using a hydraulic model constructed at length scale (prototype length/model length) of 24. The new stepped spillway is part of the Gross Reservoir Expansion (GRE) project, which by 2025 is expected to raise the existing Gross Dam about a third of its current height.

The hydraulic model presented a unique opportunity to evaluate the characteristics of flow aeration and energy dissipation along a large-scale, stepped chute of unique geometry. The stepped spillway, which will be the tallest stepped structure in the United States (Ettema et al., 2019), consists of a chute whose step dimensions at model scale, vertical to horizontal, were 0.051 m by 0.025 m, resulting in a chute slope (V:H) of 2.0, and a corresponding chute angle of 63.4^{o}. Additionally, the chute conformed, in planform, to the curved planform of raised Gross Dam. At the spillway's crest, that radius of curvature was 22.2 m (model scale). Also, the chute's sidewalls converged at an angle of 2.2^{o} from the top of the chute to the stilling basin at the base of the chute. The chute's steepness, height, curvature and convergence make the chute's geometry unique among existing stepped spillways.

1.2 Objectives of Thesis

The set of objectives for this thesis was as follows:

1. Determine how the concentration of flow-entrained air varied along and across the spillway's chute. This objective had several specific objectives:
    a) Evaluate (for the chute's design discharge) the streamwise variations of air concentration within a region of the chute where flow transitioned from gradually varied (i.e. actively bulking) to nominally equilibrium;
    b) Measure in a section of nominally equilibrium flow near the right sidewall and along the chute centerline, the variations of air concentration for water discharges less than the design discharge;

c) Ascertain the effects of chute curvature on air concentration;
d) Assess for the chute's design discharge the lateral variations of air concentration across the chute; and relatedly, the water surface, defined in this study as $Y_{0.90}$, the flow depth where $C = 0.90$;
e) Ascertain the effects of chute convergence on air concentration along the chute; and,
f) Examine what a time-series of air concentration fluctuations looks like, both for the design discharge and for a low discharge where roll waves were present along the chute.

2. Obtain profiles of bulk-flow velocity throughout the chute. This objective had several specific objectives:
   a) Evaluate (for the spillway's design discharge) the streamwise variations of bulk-flow velocity along the right descending sidewall of the chute; and,
   b) Ascertain what effect the chute curvature had on the measured flow-velocity distributions.

1.3 Background

Gross Dam, owned and operated by Denver Water and built in 1954, is an existing concrete gravity-arch dam located in Boulder County, Colorado. As presently constructed, the dam impounds the South Boulder Creek to a water-surface elevation that is 103.6 m above the natural stream bed (with a water-storage volume of about 51.8 million cubic meters). Figure 1.1 shows the current lay of the reservoir and dam.

Figure 1.1. A panoramic view of Gross Reservoir and Dam.

1.4 Gross Reservoir Expansion

The Gross Dam Expansion (GRE) Project will raise the existing Gross Dam by 40.0 m to an ultimate height of 143.6 m, thereby increasing the water-storage capacity to about 146.8 million cubic meters. The raised dam will be a thick-arch type of dam and will be constructed using roller-compacted concrete (RCC). The face of the structure will be laid using conventionally vibrated concrete (CVC).

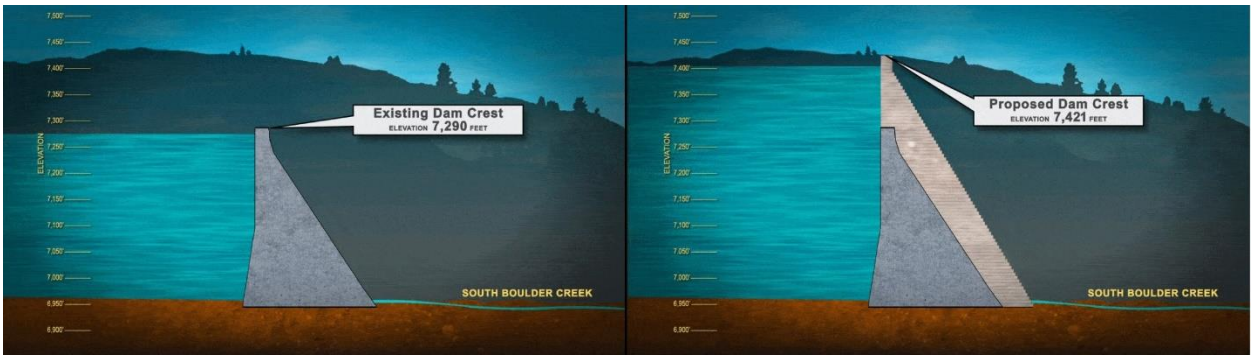

Figure 1.2: A comparison of the existing Gross Dam and proposed Gross Dam. On left, the existing structure with crest elevation of 2221.9 m, and on right, the proposed structure with crest elevation of 2261.9 m. [*https://grossreservoir.org/construction/raising-a-dam/]*

With the completion of the GRE, Gross Dam's new ungated stepped spillway will be the tallest stepped structure in the United States (Ettema et al., 2019). In addition to the spillway's height, the steepness, length and curved form of the spillway's chute make the spillway unique. As such, a model study was undertaken by Colorado State University's Hydraulics Laboratory to investigate the hydraulic performance of the design.

At model scale, the chute's nominal step dimensions, vertical to horizontal, were 0.051 m by 0.025 m, resulting in a chute slope (V:H) of 2.0 and angle of 63.4º. The chute was imparted with horizontal curvature, with radius of 22.2 m. The spillway crest featured two piers, each 0.032 m wide, at the one-third points along the crest width. The chute's sidewalls converged from a width of 2.23 m at the crest to 1.78 m at the stilling basin, a convergence angle of 2.2º. The spillway was designed to convey the watershed's Probable Maximum Flood (PMF), which at model scale was 0.347 m^3/s.

The hydraulic model of the spillway was constructed within the hydraulics laboratory of CSU's Engineering Research Center (ERC), at a length scale of 24. The model was operated in accordance with the principle of Froude number similitude. The components of the model are discussed in greater detail in Section 3.2, which includes plan and profile drawings of the model.

The model was constructed in order to assess the performance of the overall structure, with particular focus on the flow transition from the crest to the stepped chute (i.e., to verify that jet deflection does not occur); to determine the requisite sidewall height; to evaluate the amount of flow energy dissipated along the chute; to evaluate the performance of the stilling basin design; and to measure pressures throughout the model to check for incipient cavitation. The results of these investigatory objectives can be found within the model study report by Ettema et al. (2019)

1.5 Format of Thesis

The Table of Contents lists the format of this thesis. In brief, this thesis includes the following features: in Chapter 2, a review of literature related to aeration, stepped spillway hydraulics and similitude principles; in Chapter 3, an overview of the hydraulic model, the measurements obtained throughout the chute, and the instrumentation used; in Chapter 4, a presentation of the results pursuant to the objectives of the thesis (Section 1.2), with discussions and analyses; and, in Chapter 5, concluding remarks and thoughts regarding future work.

2 LITERATURE REVIEW

2.1 Introduction

In recent decades, extensive amounts of experimental studies have been undertaken to evaluate the characteristics of aerated flows along stepped chutes. Such evaluations have typically been in terms of measured values of air concentration and water surface, bulk-flow velocity, pressure, and overall energy dissipation along the chute. From those studies, guidelines have been formulated to aid in the design of stepped chutes (e.g., Chanson, 2001; Boes & Hager, 2003b; Frizell & Frizell, 2015). This chapter reviews the extant literature regarding the various aspects of air entrainment by water flows down spillway chutes. Included in the review are suggested scale limits for laboratory models of water and air flow down chutes.

A knowledge gap still exists for the influences on air entrainment of certain geometric features of chutes. As noted in the literature (Geringer & Officer 1995, Matos & Meireles 2014), chute curvature and its effects on air-water flows within stepped chutes are issues requiring further investigation. To date, no experimental study has evaluated those effects, in large part because of economic considerations. For example, Wolwedans Dam in South Africa is a gravity-arch type of dam, whose spillway conforms to the planform curvature of the dam; the spillway chute of Wolwedans Dam is nearly identical in design to the new spillway for Gross Dam. However, in the hydraulic-model study that was undertaken to assess that spillway's design, the chute model was constructed to be prismatic (i.e., without the feature of planform curvature) so that the chute model could be repurposed for later investigations (van Staden, 1991). Given the large number of gravity-arch dams which have been constructed, and the emergent trend of raising existing dams for additional water-storage capacity, knowledge of the effects of chute curvature on air-water flows should be determined.

Also, most experimental studies of stepped spillways have featured chutes whose slopes were equal to or less than the slope typical of RCC dams (θ = 53.1°, or chute slope = 1.33). While there are some notable exceptions (e.g., Straub & Anderson, 1958; van Staden, 1991; Chamani & Rajaratnam, 1999; Ohtsu, Yasuda & Takahashi, 2004; Takahashi & Ohtsu, 2012), data concerning steep, stepped chutes are scant and have not been incorporated into many of the existing, empirical relationships found in the literature.

Figure 2.1 is a plot of flow regimes, taken from a design guideline by the USBR. Along the abscissa, the ratio *h/l* represents, for a given chute, the ratio of the steps' riser and tread dimensions (i.e., the chute slope). Gross Dam, whose chute slope is 2.0, lies beyond the plotted data, and even beyond the figure's margins.

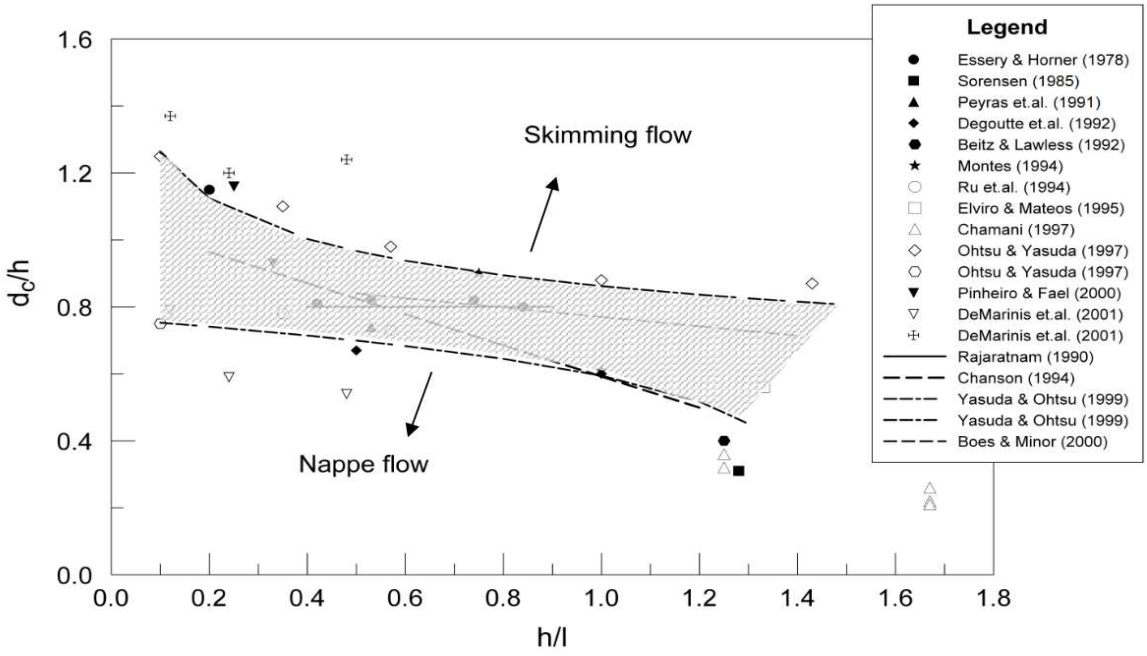

Figure 2.1: A plot of stepped chute flow regimes, with experimental data sources given in the legend (Frizell & Frizell, 2015). Along the ordinate, d_c refers to the critical flow depth, herein referred to as Y_c.

This literature review outlines the key measurements typically undertaken to evaluate aerated flows along stepped chutes. In the present thesis, those measurements are used to assess the flow, and to ascertain the effect of the chute's curvature on flow within the chute. Included in this review are pertinent, empirical relationships from the literature. Yet, most relationships (formulated for lesser chute slopes) do not conform to the data obtained along the steep chute model of Gross Dam spillway.

2.2 Air Entrainment and Concentration

The entrainment of air is a common occurrence in turbulent, open-channel flows. Along steep spillway chutes, air entrainment is a prominent feature of the flow. Air entrainment occurs when

the thickness of the turbulent boundary layer (δ) of water flow extends to the free surface. When that condition is met, the forces associated with water's surface tension and air-bubble buoyancy are overcome, and air can be entrained into the water column (Chanson, 1995).

The process of air entrainment in a stepped spillway depends on several factors, e.g., step dimensions and corresponding roughness along a stepped chute's invert, the boundary layer along a chute's sidewall, and the presence of flow obstructions that induce turbulence in flow down a spillway; notably, bridge piers along a spillway's crest.

Air concentration, *C*, is a measure of the volume of air per unit volume of total discharge. In air-water flows, air concentration is typically measured intrusively from an Eulerian perspective by analyzing the instantaneous void fraction through time at a fixed point location (Felder & Chanson, 2015). By measuring air concentration at successive flow depths and streamwise locations, the distribution of *C* and representative flow depths can be defined for a spillway.

A representative flow depth relates to a prescribed value of air concentration. It is common practice (e.g., Straub & Anderson, 1958) to relate flow depth to a prescribed value of *C*. The water surface of skimming flow[1] along a spillway chute is commonly taken to be $Y_{0.90}$; i.e. *Y* at which $C = 0.90$. This flow depth has been found to satisfy continuity analyses for air-water mixtures (Wood, 1991). Up to a flow depth of $Y_{0.95}$, the mixture is said to be quasi-homogenous wherein the slip velocity between the water surface and the air surface is negligible (Chanson, 2013).

From a measured profile of air concentration, the depth-averaged value of air concentration, $\bar{C}$, is obtained as:

$$\bar{C} = \frac{1}{Y_{0.90}} \int_{y=0}^{y=Y_{0.90}} C \, dy \tag{2.1}$$

A similar integral calculation yields Y_w, the equivalent clear-water flow depth. This theoretical value of flow depth omits all entrained air from the water-column; i.e.,

[1] Appendix B gives further details regarding the flow regimes of stepped chutes (skimming, nappe and transition flow).

$$Y_w = \frac{1}{Y_{0.90}} \int_{y=0}^{y=Y_{0.90}} (1 - C)\, dy \tag{2.2}$$

From Eq. 2.1 and Eq. 2.2, Y_w also can be calculated as:

$$Y_w = Y_{0.90}(1 - \bar{C}) \tag{2.3}$$

Just as flow depth can be expressed in terms of the bulk value of the air-water mixture ($Y_{0.90}$) and a clear-water equivalent (Y_w), so too can flow velocity be expressed in terms of the measured, bulk value of the mixture (V) and a clear-water equivalent (V_w).

From continuity, the clear-water flow velocity can be calculated, for a prismatic channel, by the following expression:

$$V_w = \frac{q_w}{Y_w}, \tag{2.4}$$

where q_w is the unit-water discharge.

The bulk-flow velocity is measured using a dual-tip conductivity probe. The values are obtained by performing a cross-correlation analysis on two voltage time-series, measured simultaneously at an offset distance in x (the streamwise coordinate). The cross-correlation analysis (Section 3.4.2) yields the travel time of the mixture, t, which is then used to calculate the bulk-flow velocity using the known offset in x (i.e., $V = x/t$).

In many applications (e.g., calculating the Darcy-Weisbach friction factor coefficient), clear-water parameters (both of flow depth and velocity) are used in lieu of the bulk-flow parameters.

2.3 Friction Factor

In skimming flows, form drag is the primary mechanism of energy dissipation (Chanson, 2006). Commonly, such energy dissipation is expressed in terms of the Darcy-Weisbach friction factor coefficient, f, calculated using Eq. 2.5, which uses the clear-water flow parameters:

$$\tau_o = \gamma\, Y_w\, \sin\theta = \frac{f}{8} \rho_w {V_w}^2, \tag{2.5}$$

where γ is the specific weight of water and ρ is the density of water. The friction factor is alternatively given by Takahashi & Ohtsu (2012) as

$$f = 8 \left(\frac{Y_w}{Y_c}\right)^3 \sin\theta \tag{2.6}$$

The Darcy-Weisbach friction factor has been found to be independent of chute slope for $\theta < 12^o$ (Chanson, 1994; Chamani & Rajaratnam, 1999). For $\theta > 25^o$, a large amount of scatter is noted within experimental data (Christodoulou, 1999).

Prior to the assemblage of empirical data sets along steep, stepped chutes, Chanson (1995) suggested $f \sim 1$ as an order-of-magnitude approximation. Shortly thereafter, Chamani & Rajaratnam (1999) provided the following expression, based on experimental data for $50^o < \theta < 60^o$:

$$\frac{1}{\sqrt{f}} = 2.16 + 1.24 \log\left(\frac{y}{k_s}\right) \tag{2.7}$$

Matos (1999) and Matos & Meireles (2014) suggest that f is a function of water discharge in steep, stepped chutes, because the overall flow resistance reduces in consequence of drag reduction with increasing discharge. This point is discussed by Boes & Hager (2003b). Figure 2.2 shows that, in steep stepped spillways, $f \sim 1$ is not a good approximation, as data show values of f as low as 0.05:

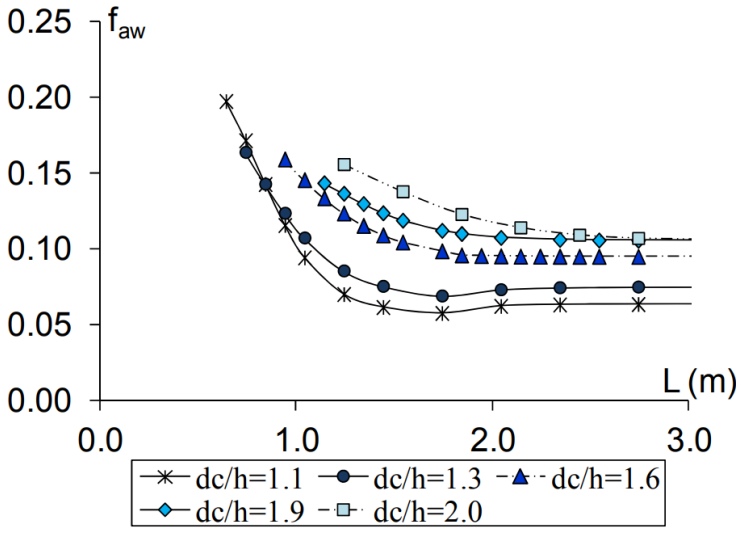

Figure 2.2. Reduction in f with increase in Y_c/h for θ=53.1° (Matos & Meireles, 2014).

Takahashi & Ohtsu (2012) give the following regression equation for $19^o < \theta < 55^o$ to calculate the effective f along a stepped channel as a function of θ, S and the smooth-chute equivalent f.

$$f = [-9.2\,\theta * 10^{-4} + 0.12]\tanh(4S) + f_{smooth} \quad (2.8)$$

where $S = h/Y_c$ and $f_{smooth} = 3.8\theta^2 * 10^{-5} - 4.4\theta * 10^{-3} + 0.135$.

2.4 Equilibrium Flow Conditions

The chute of a stepped spillway conveying a skimming flow may attain equilibrium conditions of flow, whereupon the measured values of air concentration and water surface become step invariant. The literature reports that values of equilibrium, depth-averaged air concentration ($\bar{C}_e$) are not affected by chute roughness (Ruff & Frizell, 1994; Chanson, 1994; Boes & Hager, 2003b; Matos & Meireles, 2014). Further, the prevailing notion is that equilibrium air content is not affected by the magnitude of water discharge, but by chute slope only. Hager (1991) gives the following relationship for $\bar{C}_e$ as a function of chute slope:

$$\bar{C}_e = 0.75(\sin\theta)^{0.75} \quad (2.9)$$

Christodoulou (1999) gives a similar expression, which predicts higher values:

$$\bar{C}_e = 0.9\sin\theta \quad (2.10)$$

The basis of Hager & Christodoulou's formulations is the air concentration data collected by Straub & Anderson (1958), who used a variable-slope, smooth-invert chute artificially roughened with sand. The measure of flow uniformity adopted by Straub & Anderson was successive equality of air-concentration profiles measured streamwise along the chute. When that condition of equality was met, they considered the flow to be in equilibrium. Hence their measured value of $\bar{C}$ was taken to be the equilibrium value for that configuration of slope and water discharge.

The results of their measurements showed that $\bar{C}_e$ was constant at low water discharges, but, for steep chutes ($\theta > 30^o$), $\bar{C}_e$ began to decrease with increasing discharge. Accordingly, from their data, Straub & Anderson produced a relationship for $\bar{C}$ that is dependent on slope and discharge: $\bar{C} = f(S, q^{1/5})$, where $S = \tan(\theta)$.

While Straub & Anderson considered every one of their measurements to have met this equality condition, Wood (1983) later argued that equilibrium flow conditions may not have been attained for some of their measurements. Figure 2.3 was produced by Wood, and it plots the data from

Straub & Anderson. Each chute-slope configuration (7.5°, 15°… 60°, 75°) was plotted as a separate contour, $\bar{C} = \mathrm{f}(Q)$. Wood demonstrated his argument by showing a horizontal parabola that delineated a region of constant $\bar{C}_e$ from a region where $\bar{C}$ decreased for a given slope of chute.

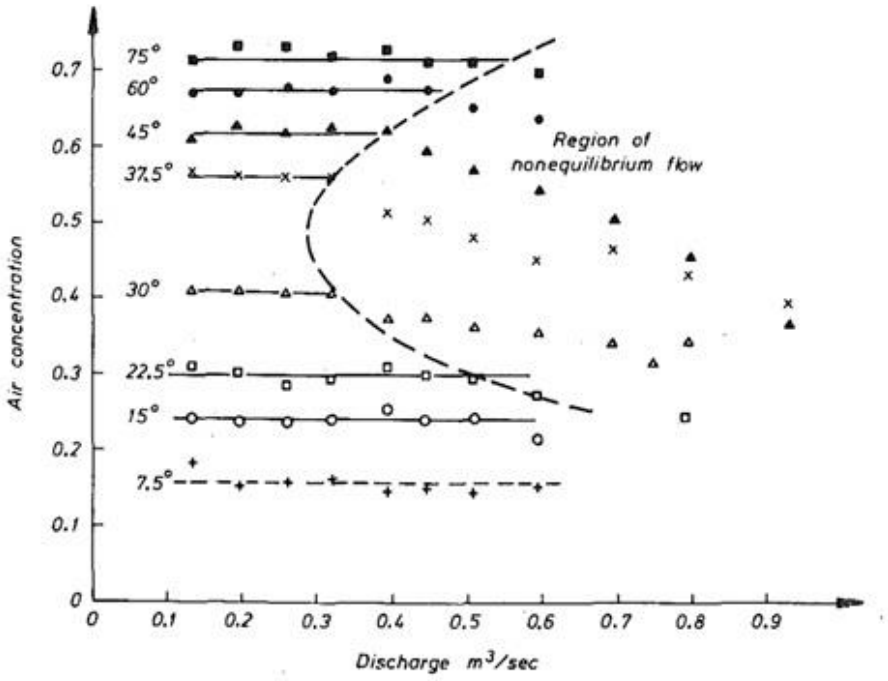

Figure 2.3. Conjectured regions of non-equilibrium flow (Wood, 1983, based on data from Straub & Anderson, 1958).

The basis of Wood's argument is that, all data points to the right of the curve labeled "region of non-equilibrium flow" must have been measured in gradually varied flow; because, for each chute-slope configuration, $\bar{C}$ should be constant for every water discharge, as suggested by the trend of constant $\bar{C}$ for water discharges which fall to the left of the curve.

However, later researchers' findings seem to agree with Straub & Anderson; e.g., the data set collected by Chamani & Rajaratnam (1999) on a chute with θ=53.1° (chute slope = 1.33) and 59.0° (chute slope = 1.66). Chamani and Rajaratnam characterize the flow region at the bottom of their chute as being a "region of fully developed (skimming) flow" – and in this region, $\bar{C}$ consistently decreased with increasing Q. Figure 2.4 shows a plot of their data, where $\bar{C} = \mathrm{f}(Q)$ in a similar fashion to the trend in Figure 2.3.

A useful comparison is to apply the equation proposed by Hager to the spillway used by Chamani & Rajaratnam. The comparison gives $\bar{C}_e(\theta$=53.1°) = 0.634, and $\bar{C}_e(\theta$=59.0°) = 0.668. Similarly, applying the equation by Christodoulou gives $\bar{C}_e(\theta$=53.1°) = 0.720, and $\bar{C}_e(\theta$=59.0°) = 0.771.

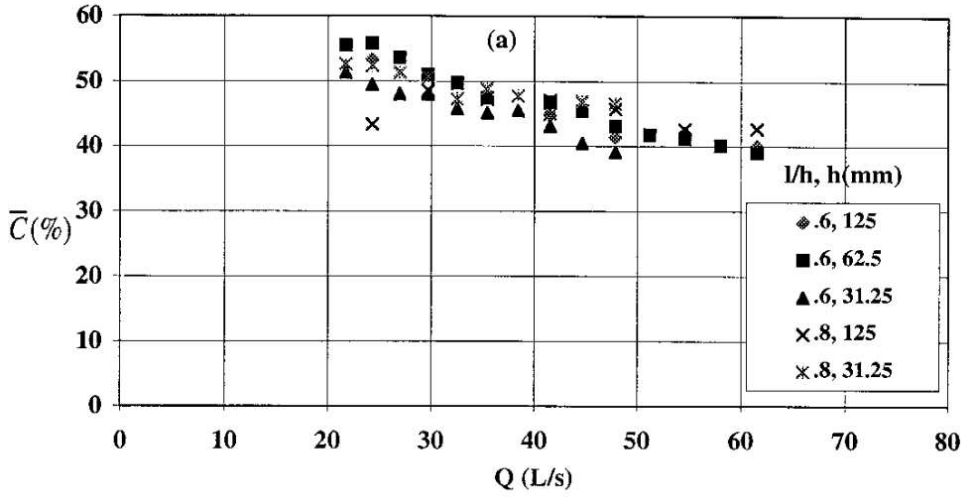

Figure 2.4. $\bar{C}_e$ as function of Q for θ = 59° (Chamani & Rajaratnam, 1999).

Accordingly, Chamani & Rajaratnam saw fit to include in their regression equation the parameter of unit-water discharge. The resulting equation is similar to that produced by Straub & Anderson:

$$\bar{C}_e = 0.93 \log\left(\frac{(\sin\theta)^{0.1}}{q^{0.3}}\right) + 1.05 \qquad (2.11)$$

Similarly, Ohtsu, Yasuda & Takahasi (2004) observe the influence of water discharge on $\bar{C}_e$. These authors, rather than dichotomizing skimming flow as being either equilibrium or non-equilibrium, consider the flow as being either quasi-uniform (developed) or non-quasi-uniform (developing). They give a relationship for $\bar{C}_e$ in quasi-uniform flow as a function of the reciprocal of Y_c/h:

$$\bar{C}_e = D - 0.30 \exp\left(-5\left(\frac{h}{Y_c}\right)^2 - 4\frac{h}{Y_c}\right), \qquad (2.12)$$

where D = 0.300 for 5.7° < θ < 19°, and $D = -2.0{*}10^{-4}{*}\theta^2 + 2.14{*}10^{-2}{*}\theta - 3.57{*}10^{-2}$

for 19° < θ < 55°.

A simpler formulation by Takahashi & Ohtsu (2012) is:

$$\bar{C}_e = \left(\frac{6.9}{\theta} - 0.12\right) S + 0.656\{1 - \exp[-0.0356\ (\theta - 10.9)]\} + 0.073\ , \qquad (2.13)$$

where $S = Y_c/h$, valid for $19^o < \theta < 55^o$.

Boes & Hager (2003a) note the use of three approaches to confirm uniform flow conditions. The first approach, used by Straub & Anderson (also Chamani & Rajaratnam, and others), is to compare profiles of air concentration measured at successive cross-sections to show equality. A second approach is to examine the longitudinal water-surface profiles of both Y_w and $Y_{0.90}$. The third approach is to calculate the friction factor, wherein Y_w is raised to third power ($f = 8\left(\frac{Y_w}{Y_c}\right)^3 \sin\theta$), thereby causing deviations to be more pronounced.

The data collected in the Gross Dam stepped spillway (Section 4.3.3) agrees with the findings of Straub & Anderson; Chamani & Rajaratnam; Ohtsu, Yasuda & Yakahasi, and others – that $\bar{C}_e$ is in fact influenced by water discharge.

2.5 Vertical Distribution of Air Concentration

The vertical distribution of air concentration has been described in both developing and equilibrium flow regions by numerous models. Wood (1984) formulated the following distribution, intended for smooth-invert chutes (although it works suitably well when applied to stepped spillways, because air concentration is not a function of chute roughness (Ruff & Frizell, 1994)):

$$C = B'/(B' + \exp[-G' \cos\theta * (\frac{Y}{Y_{0.90}})^2])\ , \qquad (2.14)$$

where the coefficients are given in Table 2.1, from Chanson (1993) based on re-analysis of data by Straub & Anderson (1958):

Table 2.1. Coefficients for Wood's distribution (Chanson, 1993).

θ	$\bar{C}$	$G' \cos\theta$	B'
30.0	0.410	0.3825	0.19635

37.5	0.569	2.675	0.6203
45.0	0.622	2.401	0.8157
60.0	0.680	1.894	1.354
75.0	0.721	1.574	1.864

Chanson & Toombes (2002) provide an alternative model, based on the bubble-diffusion equation:

$$C = 1 - \tanh\left(k' - \frac{\frac{Y}{Y_{0.90}}}{2*D_o} + \frac{\left[\frac{Y}{Y_{0.90}} - 1/3\right]^3}{3*D_o}\right)^2, \tag{2.15}$$

where the integration constants *k'* is given by Eq. 2.17, from D_o which is solved for iteratively using Eq. 2.16 and a known value of $\bar{C}$:

$$\bar{C} = 0.7622\{1.0434 - \exp(-3.614 * D_o)\} \tag{2.16}$$

$$k' = \operatorname{atanh}(\sqrt{0.1}) + \frac{1}{2 * D_o} - \frac{8}{81 * D_o} \tag{2.17}$$

Takahashi & Ohtsu (2012) give a simplified form of the bubble-diffusion equation:

$$C = 1 - \tanh\left(k' - \frac{\frac{Y}{Y_{0.90}}}{2 * D'}\right)^2 \tag{2.18}$$

$$k' = \operatorname{atanh}(\sqrt{0.1}) + \frac{1}{2 * D'} \tag{2.19}$$

$$D' = (0.848\,\bar{C} - 0.00302)/(1 + 1.1375\,\bar{C} - 2.2925\,\bar{C}^2) \tag{2.20}$$

2.6 Longitudinal Development of Air Concentration

The development of $\bar{C}$ as a function of *x* (the longitudinal distance from the spillway crest) is chute specific, and depends on the slope, and possibly water discharge. A common approach to expressing $\bar{C}(x)$ is in terms of the height relative to the spillway crest, H_d, defined positive in $-\hat{z}$; normalized by the critical flow depth. The following figure from Matos & Quintela (1995) shows empirical data for θ=53.1° assembled in this form:

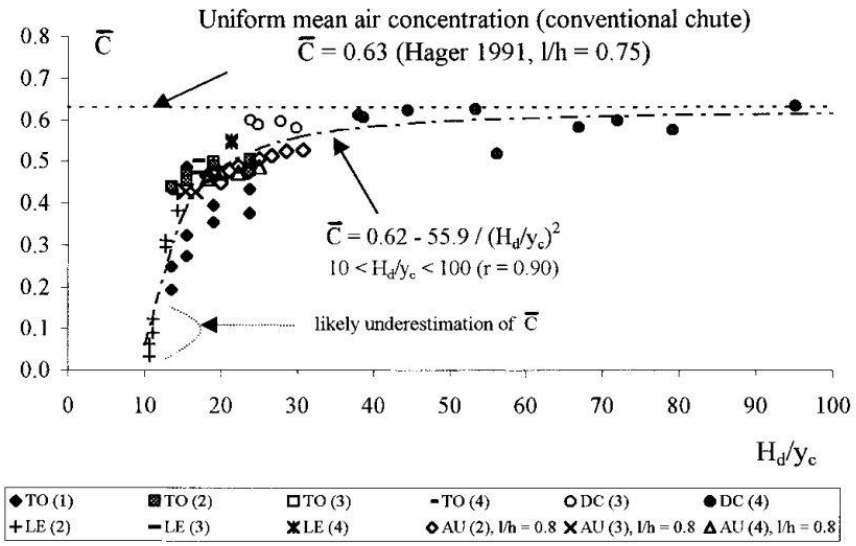

Notes:
TO - Tozzi (1992); DC - Diez-Cascon et al. (1991); Lejeune, Lejeune and Lacroix (1994); AU - Authors
(1) $k/D_h \leq 0.1$; (2) $0.1 < k/D_h \leq 0.2$; (3) $0.2 < k/D_h \leq 0.3$; (4) $k/D_h > 0.3$.

Figure 2.5. $\bar{C}$ as function of H_d/Y_c (Matos & Quintela, 1995).

For θ = 53.1° (typical of RCC dams), Matos (2000) gives the following equation to predict $\bar{C}(x)$:

$$\bar{C} = 0.210 + 0.297 \exp\{-0.497(\ln s' - 2.972)^2\} \quad (2.21)$$

$$\bar{C} = \left(0.888 - \frac{1.065}{\sqrt{s'}}\right)^2 \quad (2.22)$$

Here, the normalized parameters $s' = \frac{x - L_i}{Z_i}$ and $Z_i = \frac{z - z_i}{h_c}$. The first equation is intended for 0 < *s'* < 30 and the second for *s'* > 30.

Boes & Hager (2003a) present an alternative equation for 26° < θ < 55°, where air concentration is expressed in a normalized form, c_i:

$$c_i = [\bar{C}(Z_i) - \bar{C}_i]/(\bar{C}_e - \bar{C}_i) \quad (2.23)$$

$$c_i = [\tanh (5x10^{-4}(100° - \theta)Z_i]^{1/3} \quad (2.24)$$

Here, $\bar{C}_i$ is the mean air concentration at some point downstream the incipient point of aeration; $\bar{C}(Z_i)$ is the mean air concentration *at* the point of incipience; and Z_i is the elevation below the spillway crest of incipience. The uniform value $\bar{C}_e$ is calculated from the expression by Hager (1991).

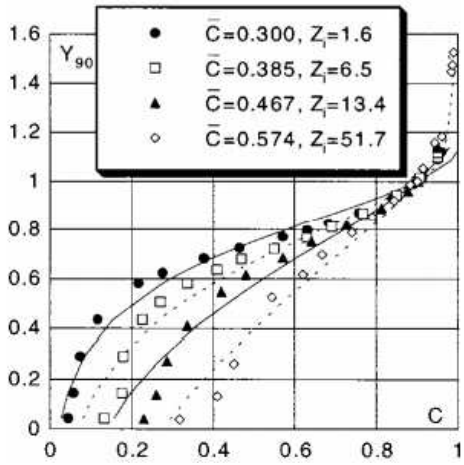

Figure 2.6. Normalized air-concentration distribution $C(Y_*)$ for $\theta = 50°$, $F_o = 3.5$, $K = 20$ mm and $h_o/s = 1.06$ (Boes & Hager, 2003a).

Boes & Hager (2003b) give an expression for the height below the spillway crest where uniform flow conditions are attained.:

$$\frac{H_{dam,u}}{Y_c} = 25.52\left[1 - 0.055(\sin\theta)^{-1/3}\right](\sin\theta)^{2/3} \qquad (2.25)$$

Here, the subscript u refers to "uniform" and is synonymous with the subscript e implying equilibrium.

Meireles et al. (2007) present plots of $\bar{C}$ as a function of x (expressed in terms of step no.) for θ = 53.1°, for different values of ψ, where ψ is the characteristic flow depth at which the water surface is defined: 0.90, 0.95, or 0.99. For each characteristic flow depth, $\bar{C}$ is evaluated for two sets of flow conditions: on left, h = 4 cm and q_w = 0.080 m^2/s; and on right, h = 8 cm and q_w = 0.140 m^2/s (in each case, θ = 53.1°, or chute slope = 1.33).

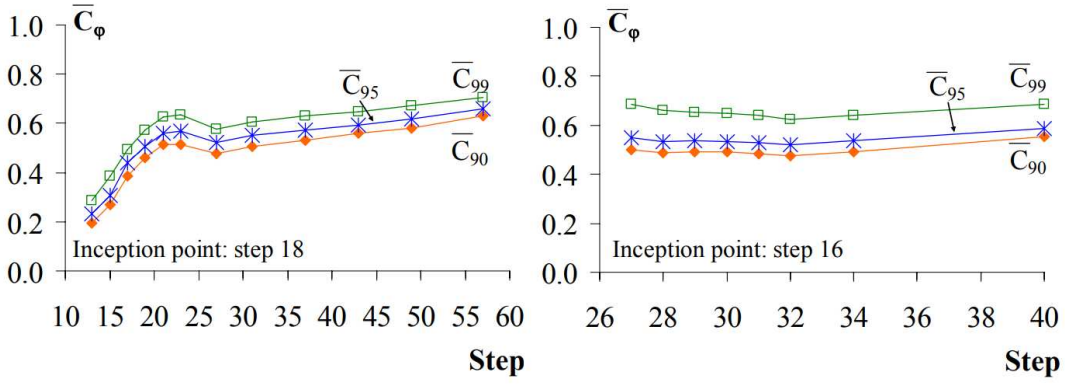

Figure 2.7. $\bar{C}(x)$ for θ = 53.1° (Meireles et al., 2007)

In Figure 2.8 (Meireles et al. 2007) the bulk flow depth is shown for each value of ψ, and the respective trends (within each plot) are independent of ψ (flow conditions are the same as for Figure 2.7).

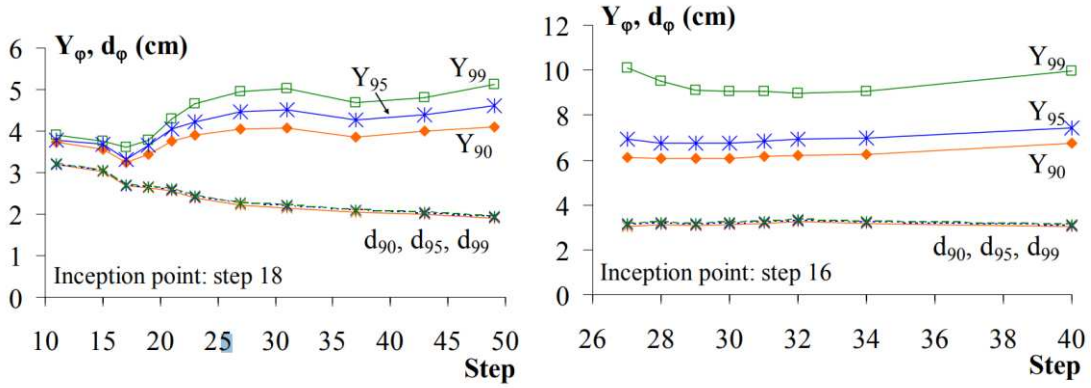

Figure 2.8. $Y_\psi(x)$ and $d_\psi(x)$ for θ = 53.1° (from Meireles et al., 2007)

Here, the clear-water flow depth Y_w is expressed as d_ψ.

Similar to Figure 2.8, Figure 2.9 from Matos & Meireles (2014) shows $\bar{C}$ as function of x (step number) for additional flowrates (for the same spillway slope):

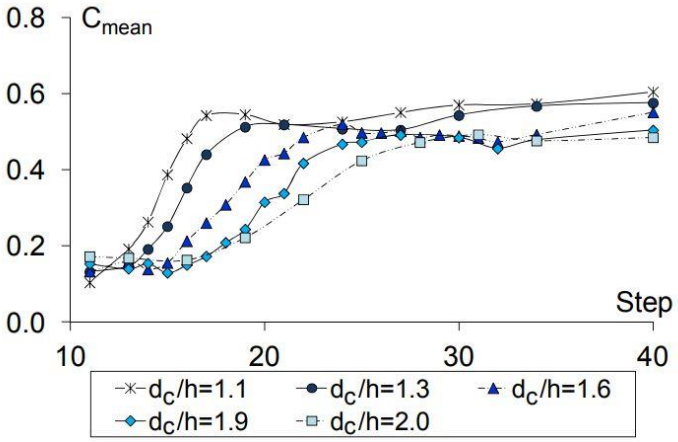

Figure 2.9. $\bar{C}(x)$ for various values of Y_c/h for θ = 53.1° (Matos & Meireles, 2014)

When normalized in x as $(L-L_i)/d_i$, as in Figure 2.10, $\bar{C}$ varies rapidly downstream the inception point, then, for some flow conditions, is seen to rooster-tail as the flow transitions into to gradually-varied.

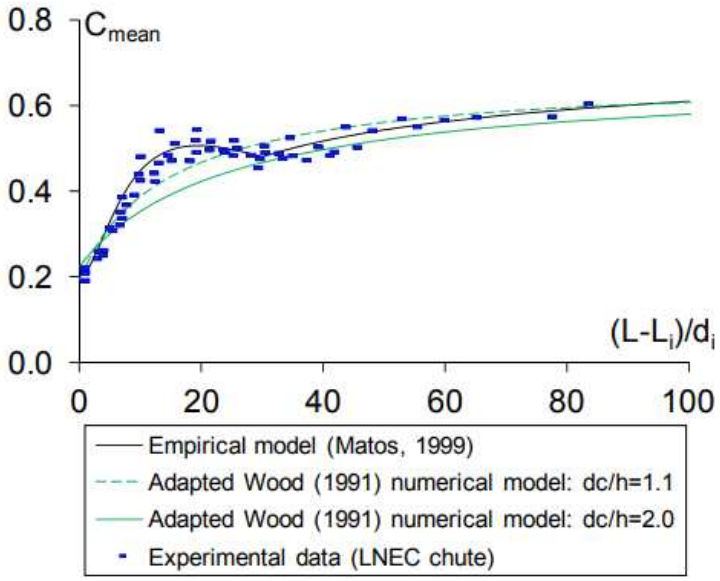

Figure 2.10. $\bar{C}(x)$ for Y_c/h = 1.1 & 2.0, θ = 53.1° (Matos & Meireles, 2014).

2.7 Bulk-Flow Velocity

The velocity distribution of aerated, skimming flows has been found to be approximated by a power-law function up to 80% of the flow depth $Y_{0.90}$, above which the magnitude of the bulk-flow velocity is constant (Boes & Hager, 2003a). The general form of the power-law function is

$$\frac{V}{V_{0.90}} = a\left(\frac{Y}{Y_{0.90}}\right)^{1/N} \text{ for } \frac{Y}{Y_{0.90}} < 0.8 \tag{2.26}$$

$$\frac{V}{V_{0.90}} = 1 \text{ for } \frac{Y}{Y_{0.90}} > 0.8 \tag{2.27}$$

These equations include an exponent N and a scalar a, though a is generally close to unity and is frequently omitted in the literature.

Boes & Hager (2003a) evaluated a number of experimental data sets and found the coefficients are best approximated as a = 1.05 and N = 4.3 for 26° < θ < 55°. For flatter slopes, they note that N generally increases. Yasuda & Chanson (2003) found that N = 9 for θ = 15.6°.

Boes & Hager (2003a) further state that to model the velocity distribution of skimming flow without scale effects the limiting values of R_e and W_e are $R_e > 10^5$ and $W_e > 100$. In their study,

they found that N was unaffected by chute slope or water discharge within the range of slopes that they tested.

On the whole, a large amount of scatter exists among values of N reported by different researchers, ranging from $N = 3.5$ by Chanson (1994), to $N = 6.3$ by Cain (1978), to, as previously cited, as high as $N = 9$ by Chanson & Yasuda (2003). The reference by Andre, Boillat, & Schleiss (2004) provides a review of additional, discrepant values of N from various researchers, and the flow conditions and chute configurations for which they were collected.

Takahashi & Ohtsu (2012) give a regression equation for the exponent of the form:

$$N = 14\theta^{-0.65} S \left(\frac{100}{\theta} S - 1 \right) - 0.041\theta + 6.27 \tag{2.28}$$

where $S = h/Y_c$, and for $19^o < \theta < 55^o$.

2.8 Sidewall Height

When flow along a spillway chute becomes aerated, the flow depth bulks. For the design engineer, quantifying the degree of bulking is an important consideration because it dictates how high the chute sidewalls must be to contain the flow.

Many design guidelines have suggested that a safety factor η can be applied to $Y_{0.90}$, yielding the design height of sidewall. Boes & Hager (2003b) suggest $\eta = 1.2$ for concrete dams and $\eta = 1.5$ for embankment dams. A different value of $\eta = 1.4$ is suggested by Ohtsu et al. (2004), informed by the measured ratio of characteristic flow depths $Y_{0.99}/Y_{0.90}$.

Following the same approach as Ohtsu et al., Meireles et al. (2007) examined the ratios $Y_{0.95}/Y_{0.90}$ and $Y_{0.99}/Y_{0.90}$ as functions of Y_c/h for stepped chutes with slopes typical of RCC dams (i.e. θ=53.1°), and found an inverse relationship given by the following expressions:

$$\eta = \left(\frac{Y_{0.95}}{Y_{0.90}} \right)_{max} = 1.061 + 0.1322 \left(\frac{Y_c}{h} \right)^{-1.034} \tag{2.29}$$

$$\eta = \left(\frac{Y_{0.99}}{Y_{0.90}} \right)_{max} = 1.140 + 0.8143 \left(\frac{Y_c}{h} \right)^{-1.499}, \tag{2.30}$$

where the latter equation servers as the more conservative guideline.

2.9 Similarity

In the design and operation of hydraulic models, similarity considerations set the proportions of lengths and forces between prototype and model-scale values.

Geometric similarity describes the ratio of lengths between the prototype structure and the model structure. If L_r represents that ratio of L_p/L_m where p refers to prototype and m refers to model, then the scale factor is defined as $1{:}L_r$. For example, the Gross Dam hydraulic model was constructed at a length scale $L_r = 24$, which corresponds with a scale factor of 1:24.

Kinematic similarity describes the proportions of motion between prototype and model, expressed in terms of velocity and acceleration. To achieve kinematic similarity, the velocity at model-scale should be proportional to the velocity at prototype-scale in the same homologous location; and, that same proportionality should hold for the ratio of accelerations. By maintaining kinematic similarity, the flow behavior in the model, in terms of velocity and acceleration, replicates exactly the behavior at prototype scale.

Dynamic similarity describes the ratio of forces between prototype and model. Typically, water flowing in an open-channel experiences three forces: gravity, viscosity, and surface tension. To maintain dynamic similitude in a hydraulic model, the forces of gravity, viscosity, and surface tension are evaluated in terms of three dimensionless numbers:

- The Froude number, which represents the ratio of inertia to gravity:
  - $F_r = \frac{V}{\sqrt{g\,Y}}$
- The Reynolds number, which represents the ratio of inertia to viscosity:
  - $R_e = \frac{V\,Y}{\nu}$
- The Weber number, which represents the ratio of inertia to surface tension:
  - $W_e = \frac{\rho V^2 L}{\sigma}$

For true dynamic similarity between the prototype and model structures, the ratios of all three dimensionless numbers must be equal – i.e., $\frac{(F_r)_p}{(F_r)_m} = \frac{(R_e)_p}{(R_e)_m} = \frac{(W_e)_p}{(W_e)_m}$. Yet, simultaneous similarity of all three dimensionless numbers is not realistic between prototype and model scale (Boes & Hager, 2003). Therefore, a common approach in the design of hydraulic models which simulate

open-channel flow processes is to maintain only similarity of the Froude number. But, because similarity is not strictly enforced for the Reynolds and Weber numbers, the modeled proportions of viscosity and surface tension do not reflect exactly the proportions at prototype scale. Generally, the viscous effects incurred by incomplete similarity of the Reynolds number can be neglected if the flow is fully turbulent at model scale. However, incomplete similarity of the Weber number is problematic in the modeling of two-phase, aerated flows, because unduly high surface tension may affect the physical processes of entrainment and mixing.

2.9.1 Scale Effects

In open-channel flows, the process of air entrainment occurs when surface-tension forces at the free-surface are overcome by turbulence. When that process is simulated in a hydraulic model scaled according to Froude number similitude, the incorrect proportions of viscosity and surface tension induce unavoidable scale effects in the model. These problems, of viscosity and surface tension, owe to incomplete dynamic similitude.

Another consideration in the true replication of air entrainment processes at model scale is the geometric length scale at which the model is constructed. Boes & Hager (2003) state that because the size of entrained air bubbles cannot be scaled proportionally to the geometric length scale, they are proportionally too large in models where Froude number similitude is used. Thus, at model scale, the transport capacity of entrained air is lower, and the rate of bubble detrainment is higher than they should be.

To limit the scale effects associated with transport and detrainment as described by Boes & Hager, recommendations suggest limits for the geometric length scale. Pinto et al. (1982) showed that a length scale between 10 and 15 is needed to properly model the entrainment of air in free-surface open channel flows. Later research by Boes (2000) confirmed that a length scale of 10 is optimum. It's noted that, when the length scale is kept within this range, the forces of surface tension and viscosity do not hinder the process of entrainment (Wood, 1991).

However, some hydraulic models cannot be constructed at such a length scale. For example, the Gross Dam stepped spillway was constructed at a length scale of 24, and very nearly does not fit inside the testing hall of CSU's hydraulics laboratory. In such models, air entrainment may still be correctly modeled by maintaining minimum values of the Reynolds and Weber numbers.

Chanson and Pfister (2013) indicate these limits to be $W_e^{0.5}$>140 and R_e > 2x10^5 to 3x10^5, when F_r ranges between 5 and 15.

3 EXPERIMENTAL MODEL & METHODOLOGY

3.1 Introduction

This chapter gives information regarding the design and operation of the hydraulic model, which was constructed at a length scale (prototype length/model length) of 24. The model's dimensions and underlying similitude principles are presented here. Also discussed are the methods whereby data were collected, and the instrumentation used in these methods.

3.1.1 Model Dimensions and Layout

The Gross Dam hydraulic model was constructed in a horizontal-bed, concrete-lined flume of plan dimensions 6.93 m by 30.48 m, and sidewalls 1.00 m high.

Table 3.1 gives the general dimensions of the model. Figure 3.1 and Figure 3.2 show plan and profile drawings of the model's layout, respectively.

Some key components of the model are as follow:

- The head tank, which simulated a portion of Gross Reservoir centered on the spillway. The head tank had planform dimensions of 4.67 m by 4.67 m, and a depth of 1.52 m. The tank contained a flow-distributor (diffuser) box. The diffuser featured several layers of semi-permeable mesh, through which flow was forced to pass on its approach to the spillway crest. By this means, the flow within the head tank was made to be uniform as it approached the spillway crest.
- The crest, which had an ogee form and featured two piers, spaced at positions of *1/3* and *2/3* of the crest's width.
- The chute, which was curved and consisted of 118 steps with dimensions (*V:H*) of 0.051 m by 0.025 m ($\theta = 63.4^{o}$). The chute included a transitional sub-reach immediately downstream the crest, consisting of eleven steps whose dimensions increased until the nominal values were attained. The chute was buttressed by converging sidewalls, which converged at an angle of 2.2^{o}. The model-scale width of the chute was 2.28 m at the crest, and 1.78 m at the entrance of the basin.
- The stilling basin, which was a modified design custom-developed for the spillway (Ettema et al., 2019).

- The sidewalls along the chute had dimensions vertical to the step treads of 0.33 m, which measured normal to the chute invert were 0.14 m in height.

In addition, the hydraulic model was constructed with scaffolding along the length of the spillway. The scaffolding, not shown in the plan or profile drawings but visible in Figure 3.3, was constructed of 80/20 Aluminum, and enabled for close access to the chute during model operation. 80/20 Aluminum was also used to construct a frame which spanned across the chute and supported a point-gage assembly during measurements of air concentration and bulk-flow velocity (Section 3.5.1).

The following table gives noteworthy model dimensions:

Table 3.1. Model dimensions

Model Component	**Dimensions**
Height of ogee crest	5.94 m
Height of bottom of head tank	4.95 m
Chute width at crest	2.23 m
Chute width at stilling basin	1.78 m
Chute angle	63.4^{o}
Step riser	0.051 m
Step tread	0.025 m
Design head over crest	0.169 m
Design discharge	0.347 m^3/s

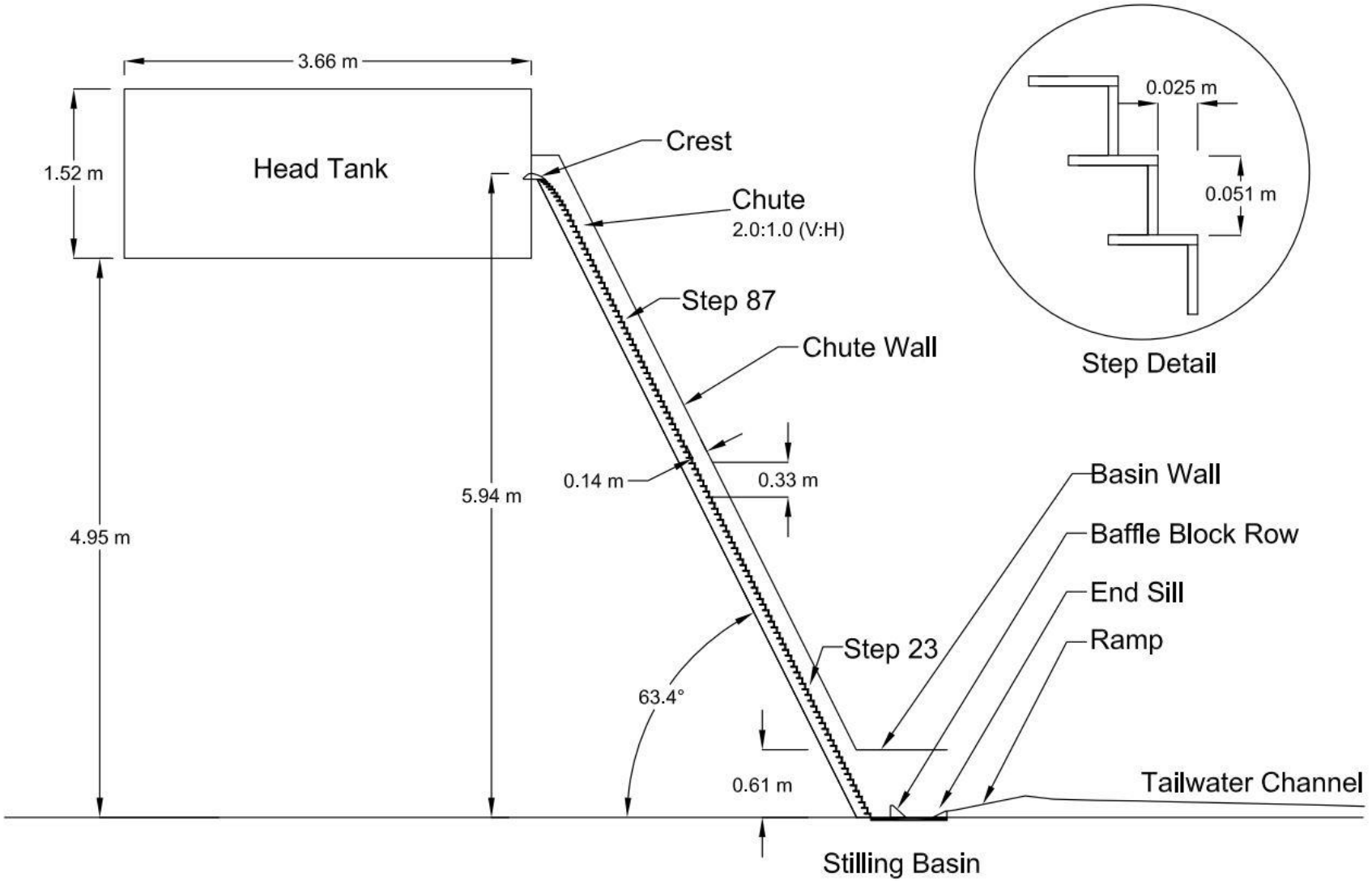

Figure 3.1. A profile view of the model of the spillway

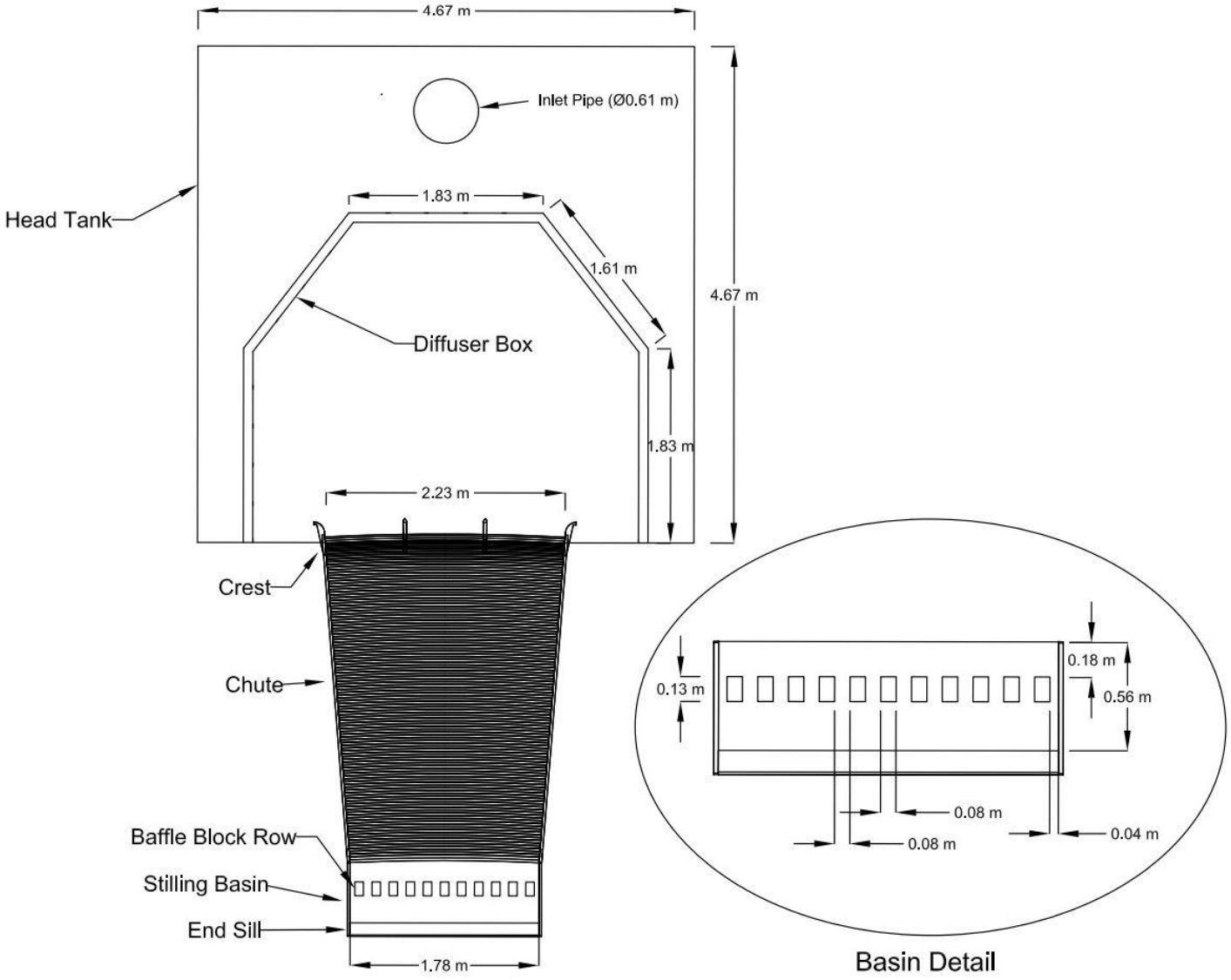

Figure 3.2. A plan view of the model of the spillway

3.2 Similitude and Model Scaling

The hydraulic model was constructed at a length scale of 24, and the model was operated in accordance with the principle of Froude number similitude. Table 3.2 gives various parameters and their model-scale values for the prototype structure.

Table 3.2. Values of variables at model scale

Variable	Scale	Scale Value
Length	L_r	24.0
Velocity	$L_r^{1/2}$	4.9
Discharge	$L_r^{5/2}$	2,821.8
Pressure	L_r	24.0
Time	$L_r^{1/2}$	4.9
Frequency	$L_r^{-1/2}$	0.2
Force	L_r^{3}	13,824.0
Reynolds No.	$L_r^{3/2}$	117.6
Webers No.	L_r^{2}	576.0

3.3 Measurements

Extensive amounts of data were measured throughout the physical model pursuant to the objectives of the model study – in the head tank, stilling basin, terminal tailwater channel, and along the chute. Generally, measurements consisted of flow velocities, both clear-water and air-entrained; air concentrations; water-surface elevations; pressures; flow-streak lines; as well as general, visual assessment of the overall hydraulic performance: e.g., in optimizing the placement of the baffle blocks within the stilling basin.

Data pertaining to air concentration and flow velocity were recorded systematically throughout the spillway, beyond the scope of the GRE model study, specifically to investigate the nature of aeration in the geometrically unique stepped chute.

This section explains where the measurements of air concentration and flow velocity (both measured using the same instrument) were taken along the spillway chute, and for what flow conditions. Also explained are the flow conditions used for the measurements.

3.3.1 Air Concentration

Measurements of air concentration were recorded point-wise and assembled into profiles normal to the chute, for a variety of discharges and in several locations (see Figure 4.1 for a definition sketch of the measured profile orientations).

The measurement instrument, a conductivity probe, functioned as a bubble detector when submerged in an air-water mixture. Each sample of air concentration data was collected for a minimum of 30 seconds, some sets for 60 seconds. The probe was affixed to a point gage which let profiles originating from the invert to be measured precisely along the gage's major divisions at increments of 0.01 ft = 3.05 mm.

Air concentration was used as the basis for defining the water surface ($Y_{0.90}$) throughout the chute. Depth-averaging was performed on the measured profiles to obtain the mean values ($\bar{C}$). From $Y_{0.90}$ and $\bar{C}$, an equivalent value of the clear-water flow depth (Y_w) was then calculated.

Values of $Y_{0.90}$, $\bar{C}$ and Y_w were used to show nominally equilibrium flow conditions at the design discharge (Q = 0.347 m^3/s) by comparing values between an upstream and downstream section of the chute, both near the right descending sidewall and along the chute centerline, to show relative invariance between the two sections.

For the design discharge of water down the chute, profiles of air concentration were measured along the right sidewall, at seven locations between steps 87 and 23 (see Figure 3.1). Figure 3.3 shows the probe and related mounting apparatus placed over step 87 for that collection of profile data, and indicates where, relative to incipient aeration at the design discharge, step 87 was. Downstream that point, the flow was gradually varied. The probe was placed at a constant distance of 4 cm from the converging sidewall along that span of steps. Also, the probe was aligned with the pseudo-bottom. At the bottom-most step where data were collected (i.e., step 23), the lower part of the mounting apparatus rested atop the stilling-basin sidewalls. Hence, chute data could not be collected downstream that transect. Measurements taken at step 23 were therefore designated as being representative of the flow at the bottom of the chute.

Also, for the design discharge, the lateral variations of air concentration ($Y_{0.90}$, $\bar{C}$ and Y_w) were evaluated in a section of nominally equilibrium flow by measuring profiles at 19 locations across the chute, along step 23. For this set of measurements, the mounting apparatus (frame) was placed such that the probe tips were positioned over the edge of the step riser along the centerline of the chute. Then, moving the probe laterally along the axis of the frame toward either sidewall, the slight planform curvature of the chute had two effects:

1. The pseudo-bottom invert was effectively deeper along the chute centerline than near either sidewall. That difference, measured normal to the chute slope was 0.018 m relative to the sidewall pseudo-bottom invert; and
2. For lateral positions which were far from the chute centerline, (say, within the left or right pier bay), the probe tips encroached slightly beyond the edge of the numbered step, into the upstream step cavity. The maximum extent of this encroachment is shown in Figure 4.4.

The resulting data set was non-dimensionalized in the lateral axis of the chute, *b/B*, where *b* was measured from the right sidewall and *B* was the local chute width. The first point mentioned above was accounted for in the lateral plot of water surface by subtracting from each measured flow depth, the offset of the chute invert, which was measured at each of the 19 chute positions using the point gage with reference to the sidewall as the 'elevation zero'.

At two fixed location across step 23, near the right sidewall and along the chute centerline, profiles of air concentration were measured for 10 different discharges. The lowest discharge for this set of measurements was 0.085 m^3/s. Subsequent discharges were increased in steps of 0.028 m^3/s. The penultimate discharge of 0.311 m^3/s was then followed by the design discharge, 0.347 m^3/s.

With all recorded samples, a time-series of the air concentration could be calculated to show the fluctuations with time. Data recorded for a duration *T* was averaged over the full duration to determine the nominal average. Then, sub-dividing that sample into smaller durations T_w, a moving average function showed the fluctuations with time. Calculating the standard deviation of that resulting time-series with respect to the nominal average gave a sense of the measurements' overall variance. Additionally, the phenomenon of roll waves was evaluated at a low discharge using the same moving average function.

Figure 3.3. The conductivity probe positioned at step 87 near the right sidewall. Step 87 corresponded with the cross-section where flow aeration had spread laterally across the entire chute.

3.3.2 Bulk-Flow Velocity

The bulk velocity of the air-water mixture was determined in the same locations as the air-concentration measurements and for the same water-discharge conditions. Both values were obtained using the same conductivity probe, explained in the next section. The calculations of bulk-flow velocity were time-averaged over the sample duration, either 30 sec or 60 sec. Velocity profiles were normalized to $V_{0.90}$, i.e. $V(at\ Y=Y_{0.90})$. Values of N (i.e., the exponent of the power function, Section 2.7) were obtained from the measured data by performing linear regressions, after log-log transformations were done.

3.4 Instrumentation

This section gives details regarding the instrumentation used to measure air concentration and bulk-flow velocity: the dual-tip conductivity probe. Along with a description of the probe's function are details regarding the setup within the hydraulic model, the experimental methodology and an overview of the data-processing procedure.

3.4.1 Conductivity Probe

A dual-tip conductivity probe was used to measure values of air concentration within aerated regions of the chute. The probe was custom manufactured by University of Queensland. The probe operates on the premise that the electrical conductivity of water is about one-thousand times greater than that of air (Straub & Killen, 1952). Because of this, when an electrode is submerged in an air-water mixture, the resulting voltage readout fluctuated between a minimum output in air, and a maximum output in clear water.

The probe consisted of two pointed tips, offset in the flow direction by 7.0 mm. The tips were excited with electricity, and the signal of the voltage readout fluctuated as the surrounding medium transitioned between water (high electrical conductivity) and air (low conductivity). The tips were shaped as needles to facilitate the direct impingement of approaching air bubbles.

Over a given sample duration, the time-averaged air concentration was obtained from the voltage time-series. First, a phase threshold was selected; i.e., a voltage value to delimit readouts in exceedance of that threshold as water, and all other readouts as air. A common threshold is taken as the average of the maximum and minimum voltage readouts (e.g., Toombes, 2002).

After a phase discrimination technique was implemented, the voltage time-series was binarized according to the voltage threshold, resulting in a time-series of the instantaneous void fraction, where C = 0 for water and C = 1 for air. The process of thresholding and binarizing was accomplished using a series of *if* statements in MATLAB.

The time-averaged values of air concentration were calculated as the arithmetic means of the instantaneous void fraction time-series (Chanson, 2013). The probe had a reported accuracy of $2.0\% < \Delta C/C < 5.0\%$. The conductivity probe's sampling frequency was variable and could be prescribed. For the present thesis and related hydraulic-model study, the optimum sampling

frequency was found to be 60 kHz. Data were sampled at that frequency for durations of 30 sec (or 60 sec) per elevation point. Sampling of the air-water mixture at precisely-incremented flow depths was made possible by the point-gage assembly.

Operation of the conductivity probe was facilitated by a point-gage assembly, which allowed for profiles measured from the chute invert to be precisely incremented in the plane normal to the chute along the major divisions of the point gage, i.e., at a spacing of 0.01 ft = 3.05 mm. The probe could also be placed at different lateral positions across the chute. The final design of the point-gage assembly was converged upon after a series of design iterations. Initially, the probe was affixed to the point gage by C-clamp connections. In this configuration, the probe was prone to slipping downward between major divisions along the point gage during the probe's operation because of the weight of the C-clamps. An additional problem with this initial design was the length of the point-gage rod, which extended far above the chute invert and was subject to oscillations when the probe was submerged in the flow.

In the final design of the assembly, the probe was connected to the point gage by bolted connection, and the length of the point-gage rod was shortened to reduce oscillations. Without the added weight of the C-clamps, and without the induced oscillations, the new assembly was found to work well during operation of the probe. The elevations at which the flow were sampled (i.e., at the major divisions along the point gage) remained steady over the 30- and 60-second samples.

The point-gage assembly is shown in Figure 3.4 and was supported by a structural frame which attached to the left sidewall and spanned the width of the chute. The frame consisted of a *T*-slotted profile oriented normal to the chute. The profile acted as a rail, and the assembly could therefore be placed at different lateral position. The structural frame was constructed with cognizance of the chute's converging sidewalls, such that the span distance to the right connection could be shortened or lengthened as needed to conform to the chute width at any given cross section.

Figure 3.4. A view of the point-gage assembly attached to the structural frame near the left sidewall of step 38

In addition to yielding air concentration data, the conductivity probe's dual-tip design facilitated the calculation of bulk-flow velocities. The computation of a sliding dot product on the voltage time-series produced by the upstream probe tip, versus the downstream probe tip, yielded a cross-correlation function. The time offset which maximized that function was taken to be the nominal travel time of the flow passing between the probe tips (Schwarzkopf et al, 2011), a known distance of 7.0 mm.

3.4.2 Discharge

The spillway's discharge was measured using a Promag W flowmeter, installed in the 0.61-m-diameter pipeline which supplied water to the head tank and required a 75 hp, 880 rpm pump. Outputs from the Promag were displayed in real-time, in units of cfs, and recorded using a LabView program. As needed, discharge measurements were saved for each model operation as

distinct time-series. The repeatability of the flowmeter was ±0.1% of the set reading at the design discharge. The influence on discharge of the ambient temperature of water was ±0.005%/°C.

The head tank and spillway essentially acted as a weir. With the head tank filled to the elevation of the crest, the spillway discharge was taken to be the subsequent volumetric input to the already-full head tank, as measured by the Promag, after waiting sufficiently long for the water level within the head tank to stabilize.

4 RESULTS & ANALYSES

4.1 Introduction

This chapter presents the results and analyses of the measurements of air concentration, water surface and bulk-flow velocity obtained from the hydraulic model of the chute. The measured data enabled analysis of the dynamic fluctuations (temporal fluctuations) of air concentration, as well as the Darcy-Weisbach friction factor associated with flow along the chute.

All profiles of air concentration and bulk-flow velocity were measured with the ordinate Y defined normal to the chute invert, as shown in Figure 4.1, where the lower dashed line adjoining each step represents the pseudo-bottom. The upper dashed line represents the water surface, defined as $Y_{0.90}$; i.e. the elevation where the time-averaged air concentration was 0.90.

Non-dimensional plots of air concentration were depth-normalized to the value $Y_{0.90}$ and, similarly, velocity profiles of the bulk flow were normalized in terms of velocity, to the value $V_{0.90}$, i.e. $V(at\ Y=Y_{0.90})$. Figure 4.2 indicates the approximate water surface $Y_{0.90}$ for the condition of skimming flow along the chute, as viewed through the chute's left sidewall.

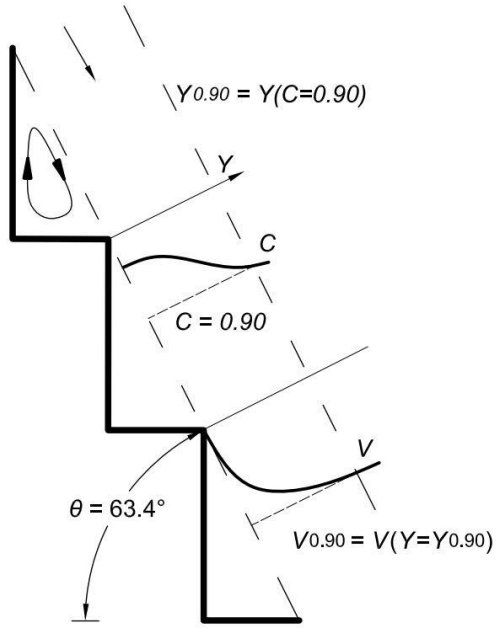

Figure 4.1. A definition sketch of air concentration and velocity profiles for skimming flow over the steps, as viewed from the right side of the chute.

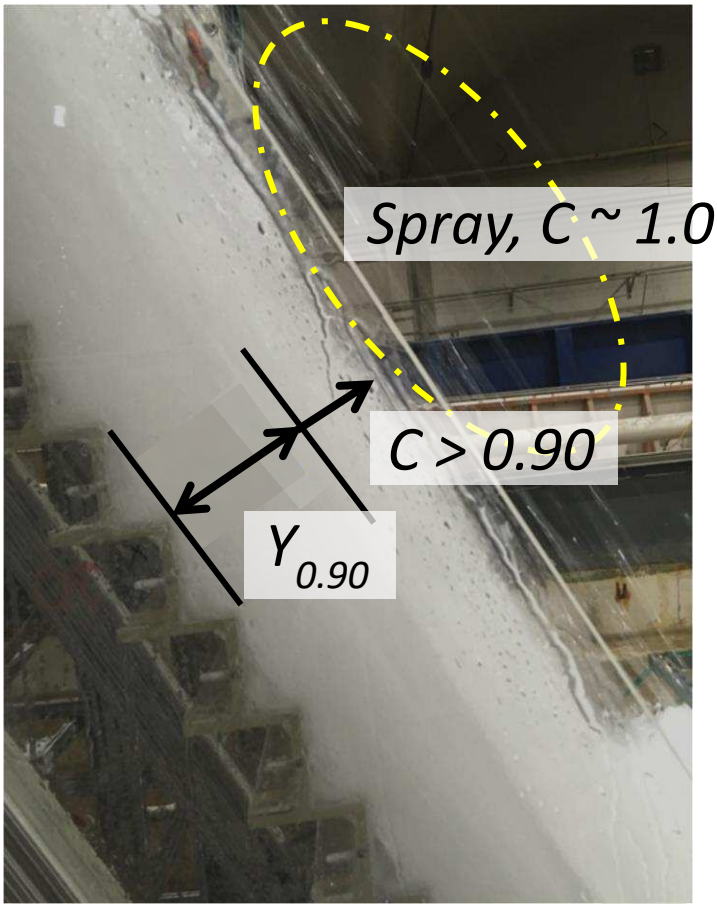

Figure 4.2. The water surface defined as $Y_{0.90}$, as viewed from the left side of the chute

Figure 4.3 shows the conductivity probe elevated at *Y=0* along the chute centerline. The steel tubing which houses the probe's electrical components rests atop the pseudo-bottom (spanning a length of about two step cavities). The position of the probe tips corresponded with the numbered step: e.g., in Figure 4.3, data were collected over step 23.

The point-gage assembly was set up on each step according to this centerline position[2]. Then, as explained in Section 3.4.1, it was set up at lateral positions away from the centerline. Because of the chute curvature, the probe's tips encroached beyond the edge of the numbered step, into the upstream step cavity. Figure 4.4 shows the maximum extent of the upstream encroachment, near

[2] Except for the profiles in Sections 4.3.2 and 4.4.2 which comprise the longitudinal data sets of velocity and air concentration. There, the point-gage assembly was set up with the probe tips aligned with the step edge near the sidewall.

the sidewall of step 23, where the probe tips encroached a distance of about 10% into the upstream step cavity. Here, the profile was not truly collected at step 23, but at step 23 + ~0.1x.[3]

Figure 4.3. The conductivity probe positioned along the centerline of the chute at elevation $Y=0$

[3] By the literature's convention, x refers here to the span of one step. The interior, step cavity locations are expressed as stations – not to be confused for x, previously used to express the longitudinal axis of the spillway chute.

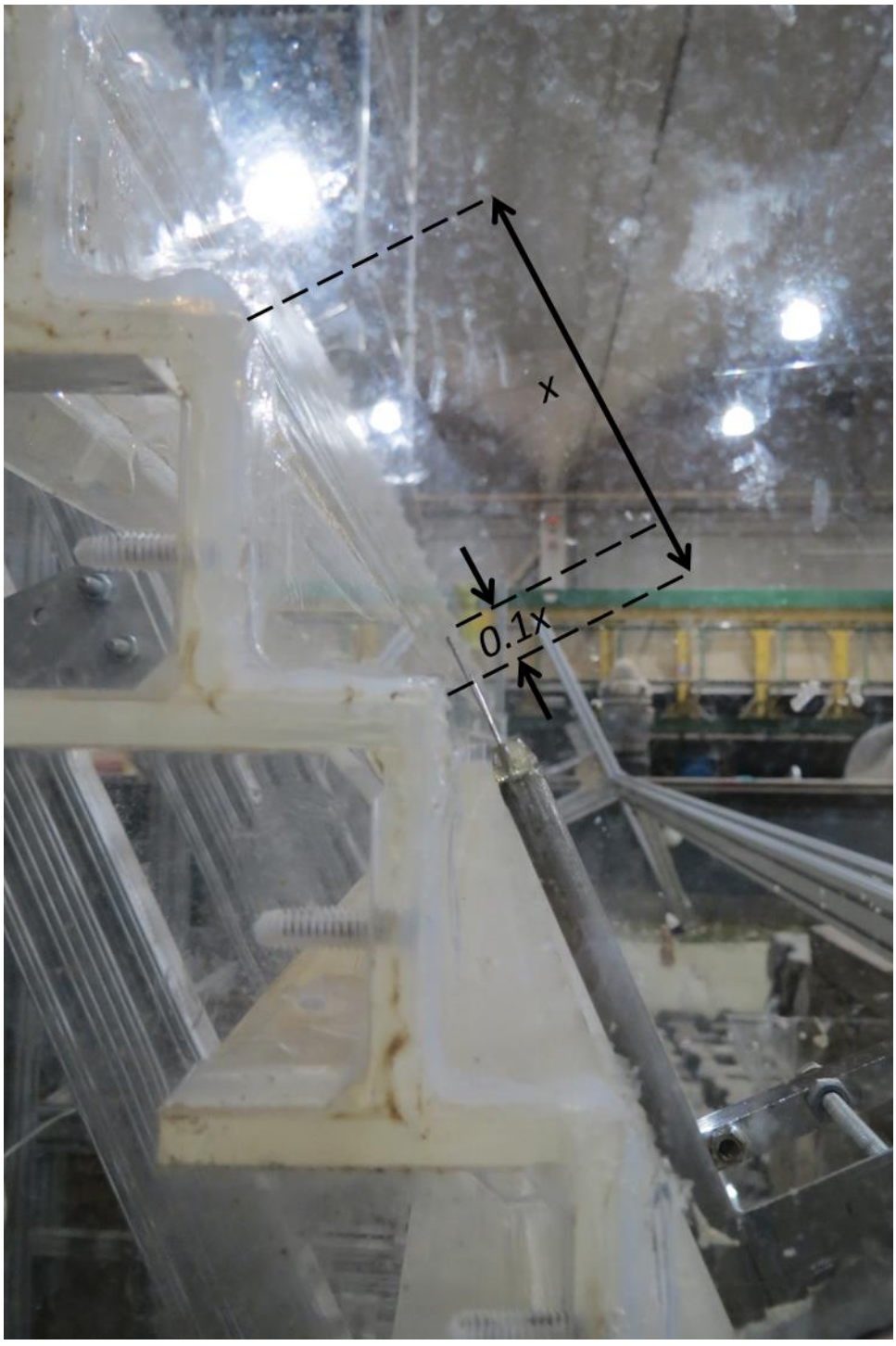

Figure 4.4. The upstream encroachment of the probe's tips near the chute's right sidewall, when the point-gage assembly was setup in accordance with the chute-centerline position (see Figure 4.3)

Figure 4.5 provides an aerial definition sketch of a typical step tread, and indicates the convention used for defining non-dimensional lateral positions (*b/B*) across the chute. The plan-form curvature of the spillway chute can also be discerned in the figure. The dashed line indicates where the foremost edge of the tread would lie, if the chute lacked any curvature.

As stated above, the measured, relative offset at the centerline position over step 23, measured in the plane normal to the chute pseudo-bottom, was 0.018 m. This offset is *not* indicated in Figure 4.5 by the straight-line distance between the dashed line (no curvature) and the foremost edge of the tread, because the profile measurements and invert surveys were conducted in the plane normal to the spillway, while the chute curvature was strictly horizontal. Hence, the relative offsets measured by the point gage comprise trigonometric hypotenuses, formed by any such straight-line distance (in the horizontal plane), and the positive z axis.

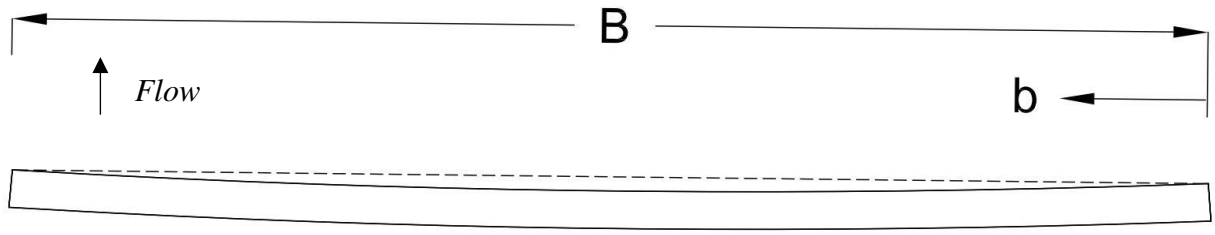

Figure 4.5. A definition sketch of the lateral position, *b*, when viewed looking downstream along the chute

4.2 General Flow Conditions

This section describes the flow conditions observed along the chute as it conveyed the full range of tested discharges. The photographs in Appendix A augment the descriptions contained in this section.

The skimming regime was fully established when $Q \geq 0.028$ m^3/s. At this discharge, incipient aeration occurred relatively uniformly across the chute at the end of the transitionary reach (i.e. the beginning of the nominal step dimensions), due to the relative roughness (height) of the steps in relation to the shallow flow depth.

When $Q < 0.028$ m^3/s, the skimming regime was discontinuous along the chute. The lowest attainable model discharge (from the pump) was approximately $Q = 0.014$ m^3/s. Within this

range of discharges (0.014 $m^3/s < Q < 0.028$ m^3/s), the flow was characterized by the presence of roll waves. Between each passing wave, the skimming water surface periodically collapsed into the step cavities. Nappe flow was observed only fleetingly, for $Q < 0.014$ m^3/s, and only after the pump was turned off and the head tank was draining.

With increasing discharge, incipient aeration occurred farther downstream along the chute, and was most delayed in regions that were relatively unaffected by the piers and sidewall presence. Clear-water flow extended farthest downstream near the pier midpoints (about $b/B = 0.17$, 0.50, and 0.83 across the chute). Near the sidewalls and downstream the piers, flow aeration was induced nearer to the crest. Aeration occurred near the sidewalls because of the boundary layer of the sidewall; and immediately downstream from each pier because of flow separation from each pier, which resulted in low pressure (slightly sub-atmospheric) voids that drew in and mixed air into the water flow.

At the design discharge, $Q = 0.347$ m^3/s, air entrainment began at approximately the same elevation for the piers and sidewalls, step 106 (in comparison, the crest is herein termed step 118). Clear-water flow extended downstream (at the pier midpoints) to about step 87. There below, air entrainment was observed fully across the chute. The resulting profile of incipient aeration took on a characteristic profile at higher discharges, appearing as a triple-catenary arc.

Figure 4.6. The model spillway conveying the design discharge, viewed from a distance

4.2.1 Equilibrium Flow Conditions

Equilibrium flow conditions were assessed at the chute's design discharge by comparing measured profiles of air concentration between successive upstream/downstream sections. This assessment was done for two chute positions: near the right descending sidewall, and along the chute centerline. At the centerline position, the upstream section corresponded with step 32 and the downstream section with step 23. At the chute-sidewall position, those steps were 34 and 23.

The measured flow depth $Y_{0.90,}$ and calculated parameters $\bar{C}$, Y_w and V_w were all basically invariant with step number at the design discharge, once flow reached step 23, at both chute positions (i.e., the sidewall and centerline positions).

The chute's curvature, as well as its converging sidewalls, rendered the flow inherently non-uniform. Yet, by the standard of flow uniformity adopted by previous researchers (i.e., equality of successive air concentration profiles), the values of $Y_{0.90}$, $\bar{C}$ and Y_w were considered to have reached their respective equilibrium values in the measured chute positions once flow passed step 23.

4.3 Air Concentration

The following data pertaining to air concentration were obtained within the chute:

1. An evaluation of equilibrium flow conditions at the design discharge;
2. Successive profiles of air concentration obtained along the sidewall in a reach where, at the design discharge, flow transitioned from gradually-varied to nominally equilibrium flow;
3. Profiles of air concentration obtained for a range of discharges at two lateral positions, in a section of equilibrium flow;
4. Profiles of air concentration obtained at intervals across the chute, in a section of equilibrium flow, at the design discharge; and,
5. An evaluation of air concentration in terms of a time-series of measurements, at the design discharge and at a low discharge where the phenomenon of roll waves occurred.

4.3.1 Equilibrium Flow Conditions

The measurements described in Section 4.2.1 yielded values of $Y_{0.90}$ and Y_w in very close agreement. Table 4.1 compares those values as measured at two chute positions: $b/B = 0.02$ and $b/B = 0.50$. The figure shows that the measured values agreed to within 1.0 mm of each other between the upstream and downstream sections, for each respective chute position.

Due to the chute's non-prismatic geometry, the flow was non-uniform across the chute. As Table 4.1 shows, $Y_{0.90}$ and Y_w varied considerably across the chute as a result of the chute's curvature, with centerline values along the chute being about 30% greater than values near the chute sidewalls.

Table 4.1. Values of $Y_{0.90}$, $\bar{C}$ and Y_w measured at the chute-sidewall and centerline positions when the chute conveyed the design discharge

	Right Sidewall $b/B = 0.02$		Centerline $b/B = 0.50$	
	Step 34	*Step 23*	*Step 32*	*Step 23*
$Y_{0.90}$ (m)	0.075	0.076	0.096	0.097
Y_w (m)	0.033	0.033	0.043	0.043
$\bar{C}$	0.557	0.570	0.554	0.553

Figure 4.7 shows the profiles that produced the results in Table 4.1. Part (a) shows profiles for the chute position $b/B = 0.02$, and (b) shows profiles for $b/B = 0.50$.

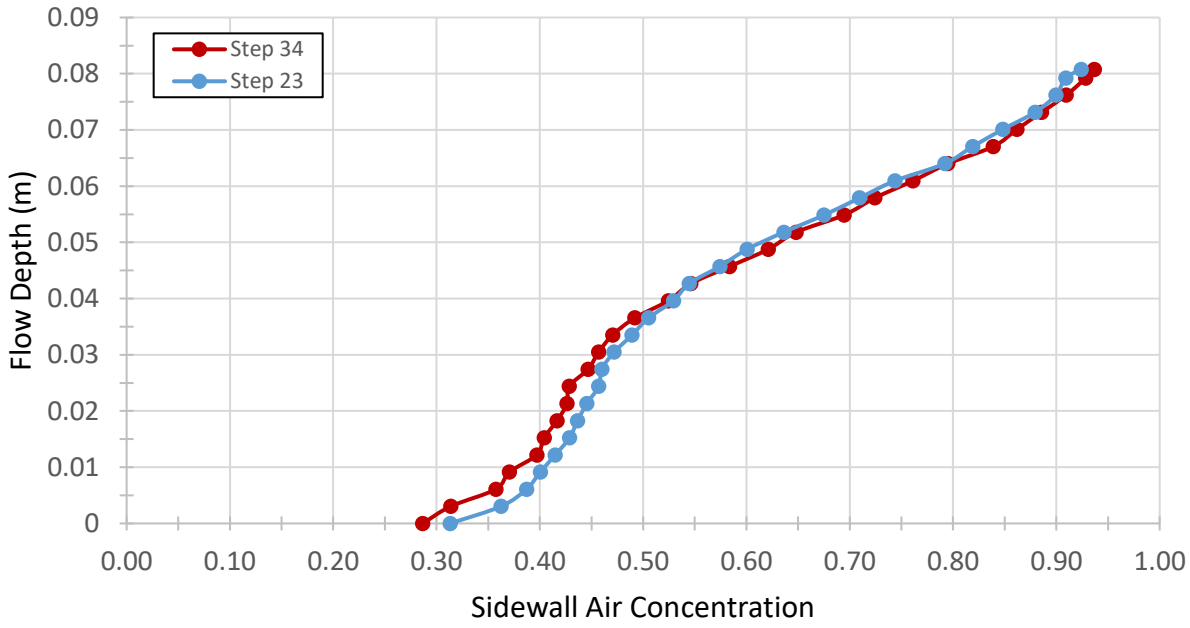

(a)

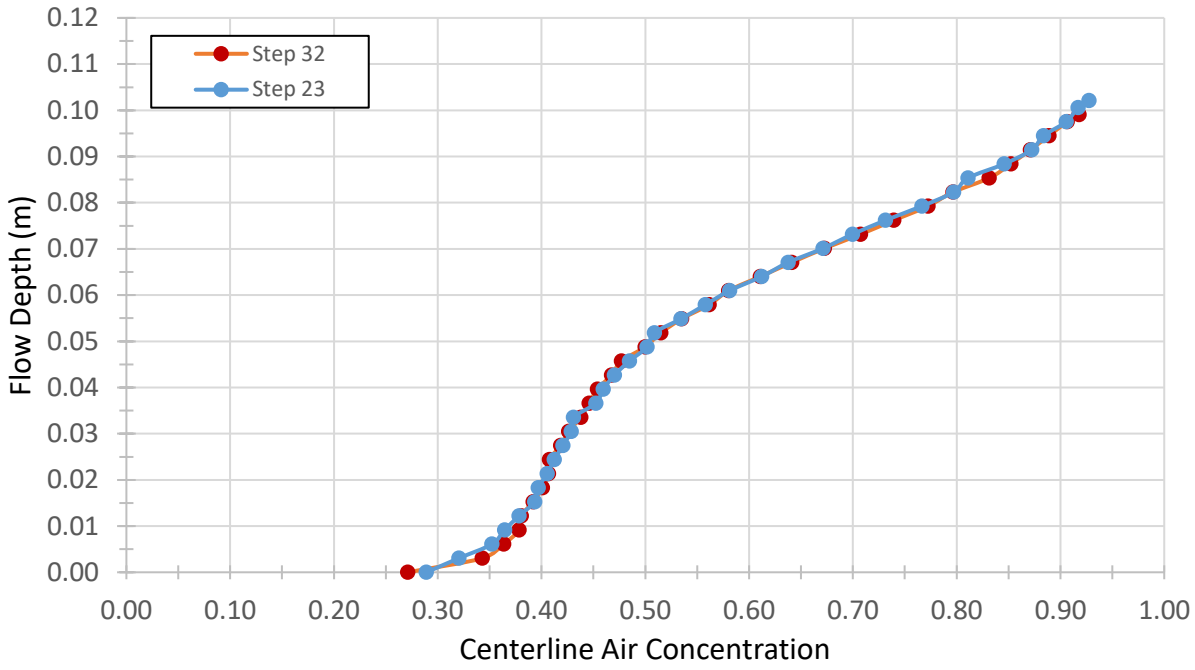

(b)

Figure 4.7. A comparison of streamwise profiles of air concentration measured as the chute conveyed the design discharge, at chute positions: (a) b/B = 0.02, and (b) b/B = 0.50.

4.3.2 Measurements Along the Chute Sidewall

This section presents air-concentration profiles collected along the right sidewall when the chute was conveying its design discharge. The profiles are then assessed in terms of a longitudinal water-surface profile.

4.3.2.1 Air-Concentration Profiles

Figure 4.8 shows profiles of air concentration collected between steps 87 and 23. Step 87 corresponds with the upstream section where a state of aeration has spread fully across the chute (see Figure 3.3). All data were measured 4 cm out from the sidewall (i.e., b = 0.04 m). At step 23, where B = 1.87 m, that position corresponded with b/B = 0.02. Because of the chute's converging width, b/B was slightly less for the higher steps. The figure shows two sets of plots, where flow depth is expressed (a) dimensionally and (b) non-dimensionally. The main trends are as follow:

1. Within gradually varied (bulking) flow, successive air concentration profiles shifted rightward, reflecting two processes: the vertical mixing of entrained air, and the continued entrainment of additional air. In the lower part of the water column, $Y/Y_{0.90} <$ 0.50, the volume of entrained air increased by about 20% between steps 87 and 23.
2. The variations caused the mean concentration of entrained air ($\overline{C}$) to increase with downstream distance. Depth integration was performed on the profiles, and the results are given in Table 4.2. For example, at step 87, $\bar{C} = 0.430$, and at step 23, $\bar{C} = 0.570$.
3. Equilibrium flow conditions prevailed near the bottom of the chute (step 23).

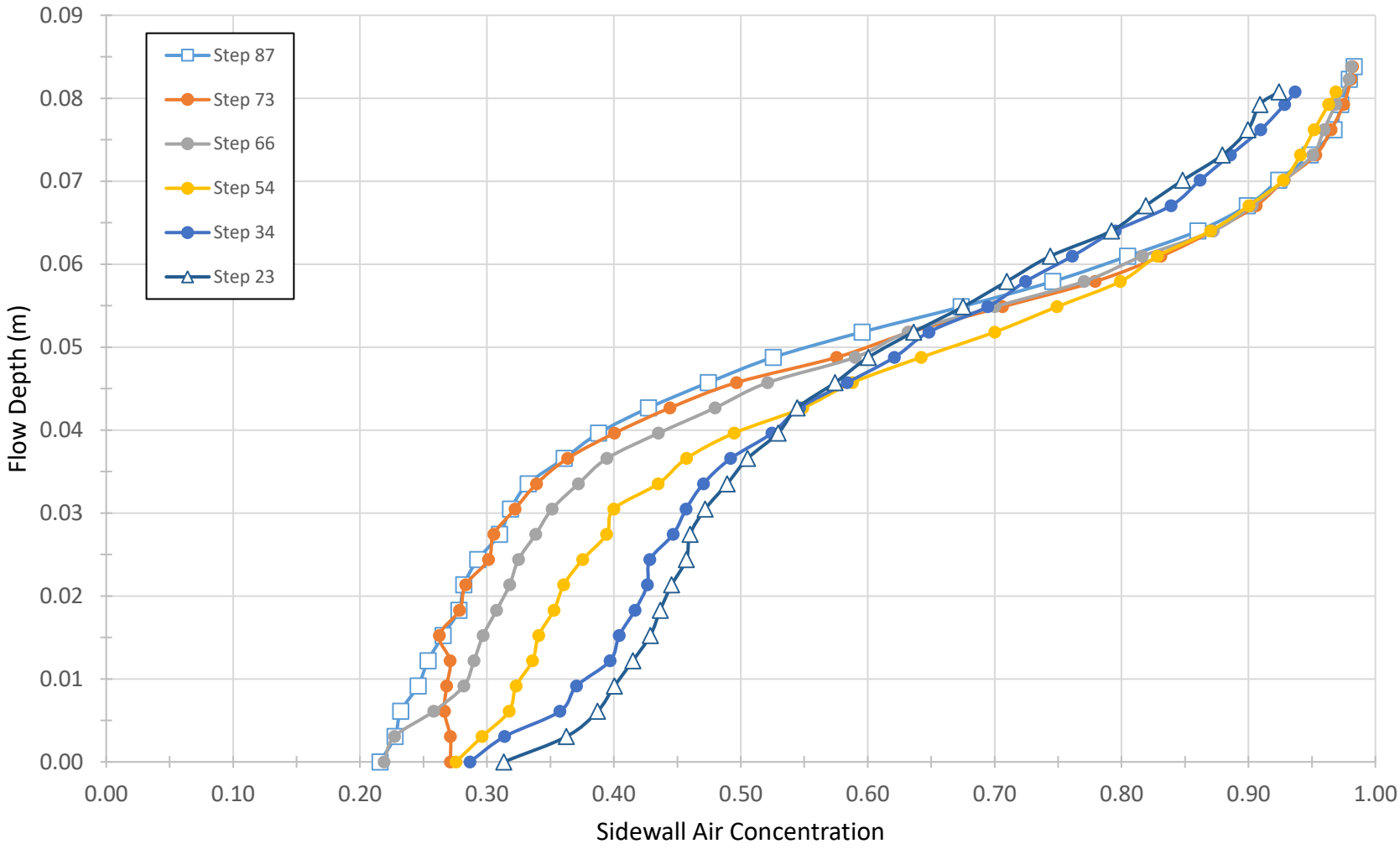
Step 87
Step 73
Step 66
Step 54
Step 34
Step 23
Flow Depth (m)
0.00
0.01
0.02
0.03
0.04
0.05
0.06
0.07
0.08
0.09
0.00
0.10
0.20
0.30
0.40
0.50
0.60
0.70
0.80
0.90
1.00
Sidewall Air Concentration

(a)

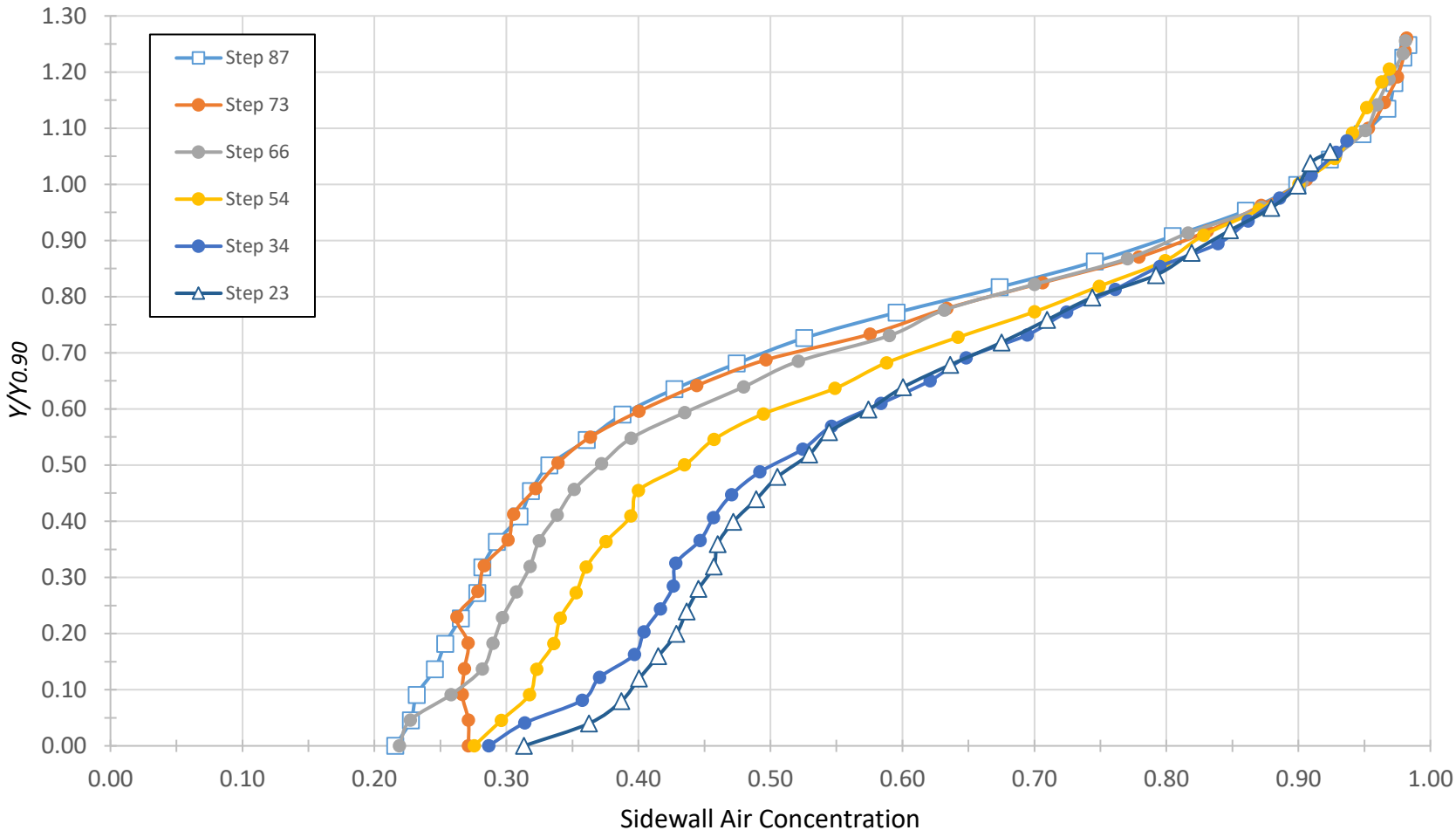

(b)

Figure 4.8. Sidewall profiles of air concentration measured between steps 87 and 23 when the chute conveyed the design discharge: (a) dimensional values, and (b) non-dimensional values.

Table 4.2. The longitudinal variations of $Y_{0.90}$, Y_w and $\bar{C}$ measured near the chute's right sidewall when the chute conveyed the design discharge.

	Step No.					
	87	*73*	*66*	*54*	*34*	*23*
$Y_{0.90}$ (m)	0.067	0.067	0.067	0.067	0.075	0.076
Y_w (m)	0.038	0.037	0.036	0.033	0.033	0.033
$\bar{C}$ (%)	0.430	0.445	0.459	0.509	0.557	0.570

4.3.2.2 Water Surface

Figure 4.9 plots the water-surface profile, in terms of $Y_{0.90}$ and Y_w, between steps 87 and 23 along the right chute sidewall. The value of $Y_{0.90}$ at that sidewall position reached an equilibrium magnitude of 0.076 m between steps 54 and 34. Similarly, Y_w became invariant after step 54, reaching an essentially equilibrium value of 0.033 m.

Figure 4.10 shows the longitudinal variations of $\bar{C}$. All the data plotted are listed in Table 4.2.

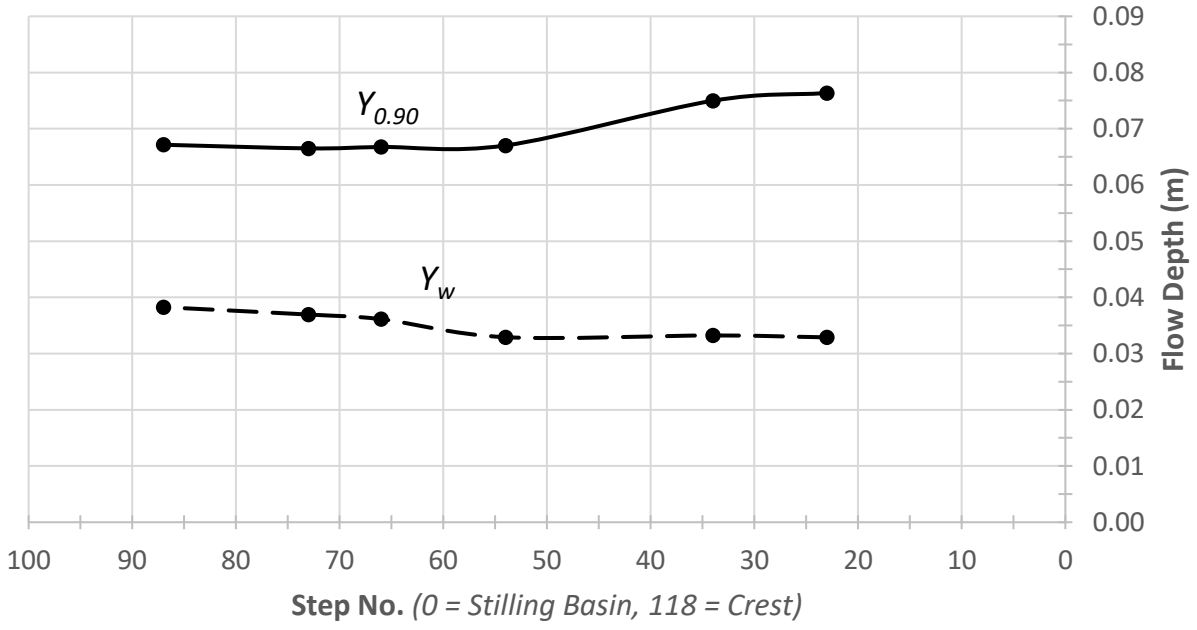

Figure 4.9. The longitudinal variations of $Y_{0.90}$ and Y_w near the right chute sidewall when the chute conveyed the design discharge.

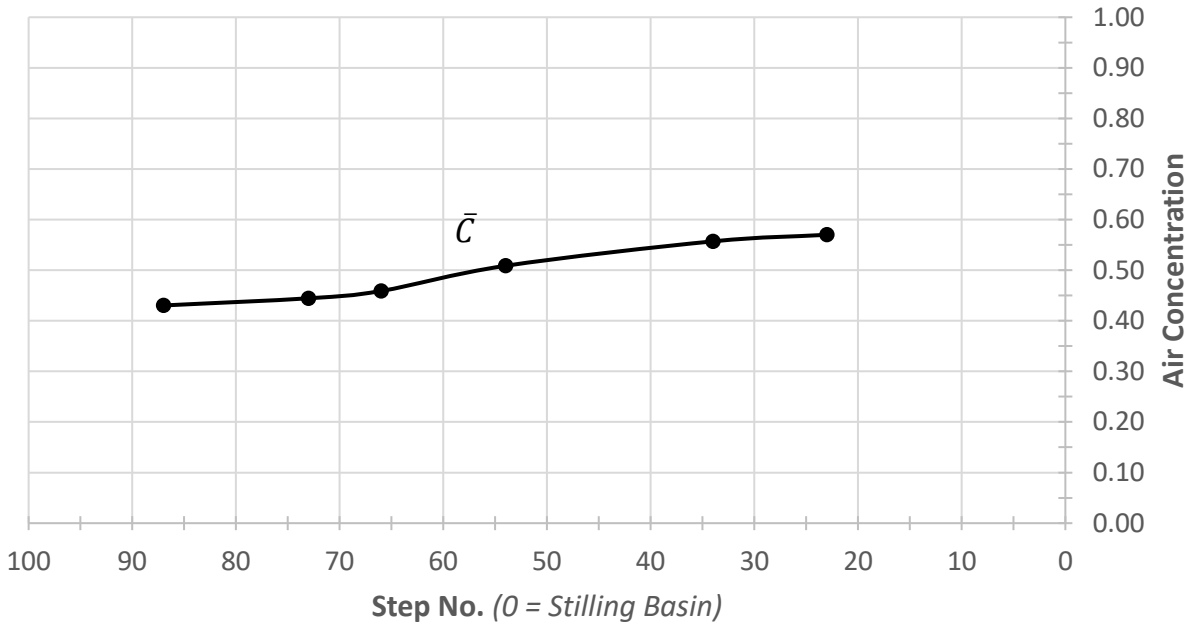

Figure 4.10. The longitudinal variations of $\bar{C}$ near the right chute sidewall when the chute conveyed the design discharge.

4.3.3 Variation with Water Discharge

This section presents air concentration profiles measured above step 23 for a range of water discharges down the chute. The profiles were measured at two locations: *b/B* = 0.02 and 0.50. At each location, the profiles are shown in two plots, with flow depth expressed dimensionally and non-dimensionally.

The lowest discharge used was Q = 0.085 m^3/s. Subsequent discharges were increased by an amount ΔQ = 0.028 m^3/s, up to Q = 0.311 m^3/s. The design discharge (Q = 0.347 m^3/s) was then used.

At both locations, two trends were evident with increasing discharge:

1. The dimensional profiles of air concentration stretched vertically because of the increasing flow depth; and,
2. The normalized profiles of air concentration shifted leftward, an indication of decreasing $\bar{C}$.

In the measured data that follow, as per the second observation noted above, $\bar{C}$ was found to be inversely related to Q at both chute locations. The measured data that follow generally replicate prior observations reported by previous researchers, as discussed further in Section 4.6.

4.3.3.1 Sidewall

This section presents the measurements of air concentration collected above step 23 for a range of water discharges down the chute, at the chute-sidewall position; i.e., at $b/B = 0.02$.

Table 4.3. The variations with water discharge of $Y_{0.90}$, $\bar{C}$ and Y_w at the chute-sidewall position of step 23.

	Discharge (m^3/s)									
	0.085	*0.113*	*0.142*	*0.170*	*0.198*	*0.227*	*0.255*	*0.283*	*0.311*	*0.347*
$Y_{0.90}$ (m)	0.025	0.032	0.040	0.047	0.052	0.059	0.063	0.068	0.071	0.076
$\bar{C}$	0.663	0.654	0.646	0.634	0.629	0.622	0.617	0.595	0.595	0.570
Y_w (m)	0.008	0.011	0.014	0.017	0.019	0.022	0.024	0.028	0.029	0.033

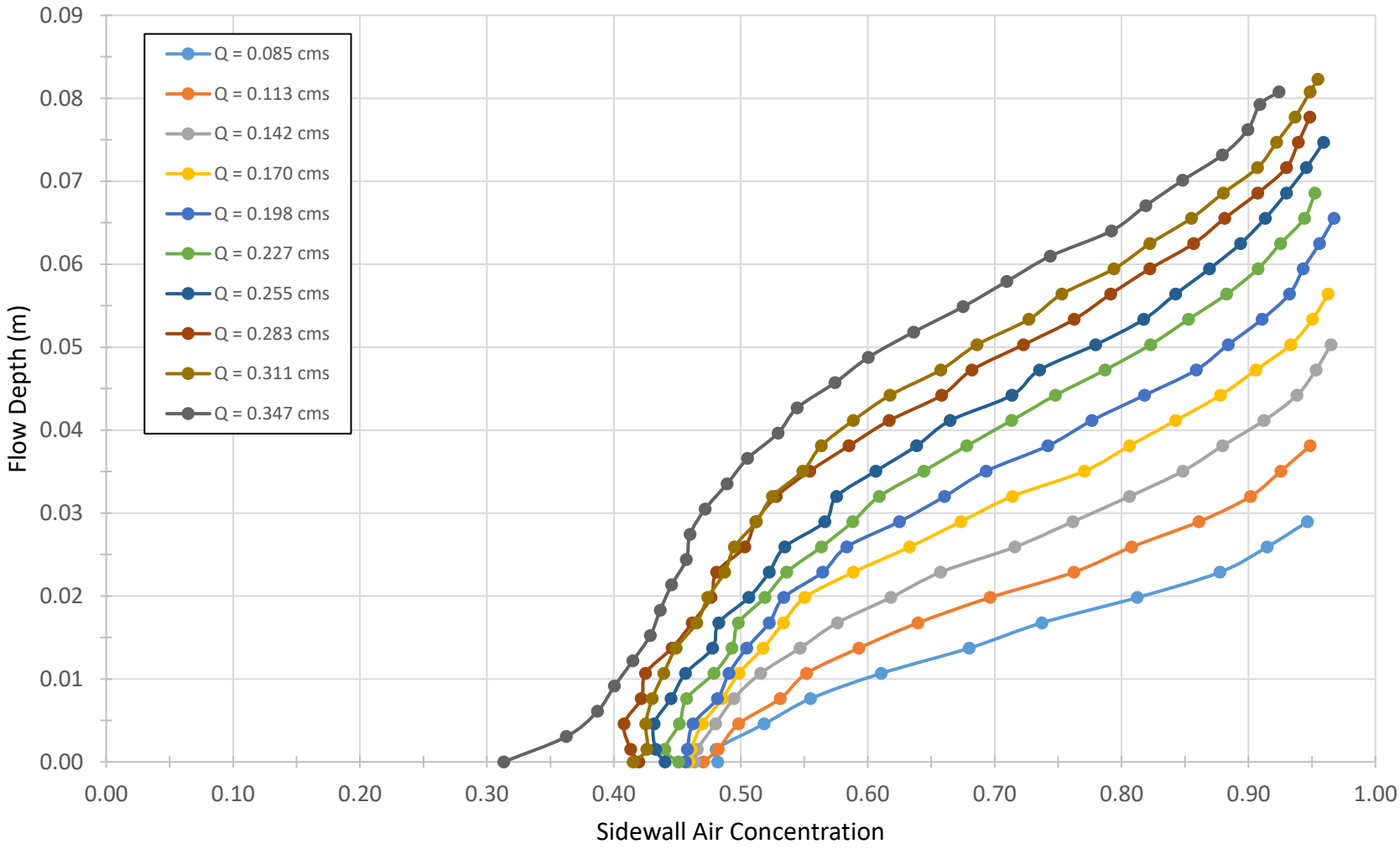
Q = 0.085 cms
Q = 0.113 cms
Q = 0.142 cms
Q = 0.170 cms
Q = 0.198 cms
Q = 0.227 cms
Q = 0.255 cms
Q = 0.283 cms
Q = 0.311 cms
Q = 0.347 cms
Flow Depth (m)
0.00
0.01
0.02
0.03
0.04
0.05
0.06
0.07
0.08
0.09
0.00
0.10
0.20
0.30
0.40
0.50
0.60
0.70
0.80
0.90
1.00
Sidewall Air Concentration

(a)

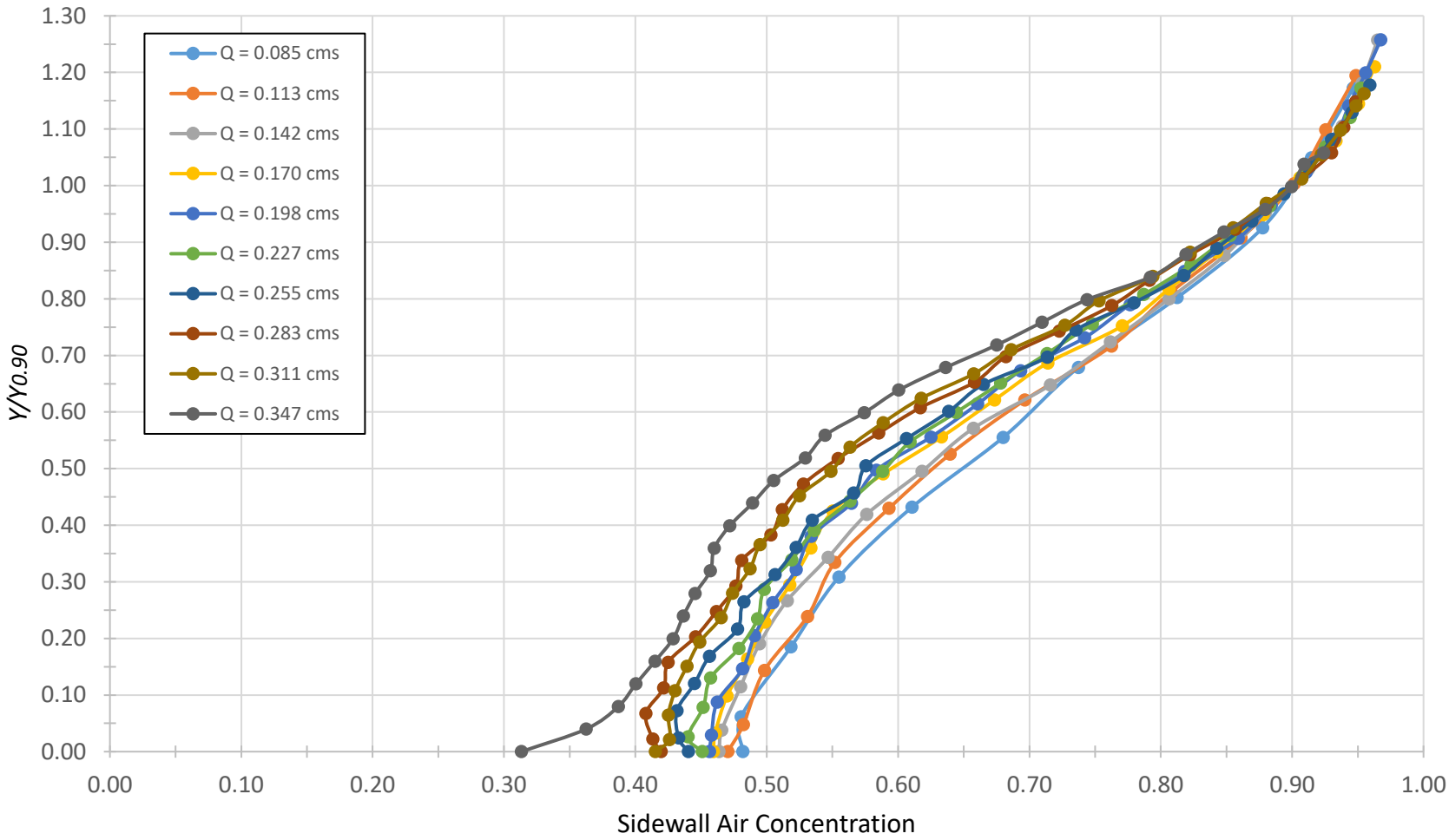

(b)

Figure 4.11. Air-concentration profiles measured for various water discharges at the chute-sidewall position of step 23: (a) dimensional values, and (b) non-dimensional values.

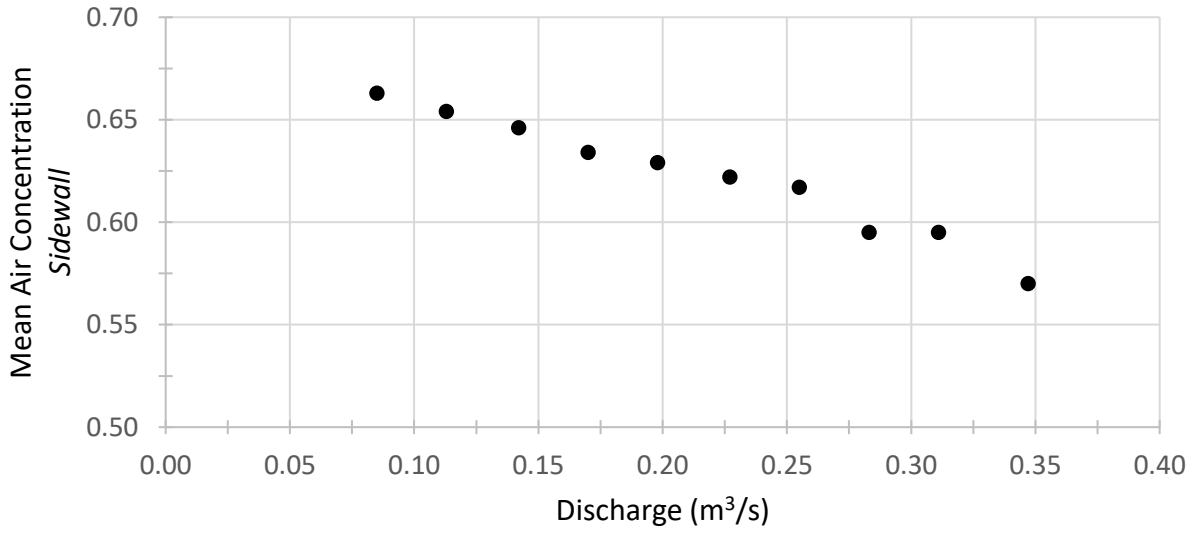

Figure 4.12. Values of depth-averaged air concentration, measured at the chute-sidewall position of step 23, plotted as a function of water discharge.

4.3.3.2 Centerline

This section presents the measurements of air concentration collected above step 23 for a range of water discharges down the chute, at the chute-centerline position; i.e., at $b/B = 0.50$.

Table 4.4. The variations with water discharge of $Y_{0.90}$, $\bar{C}$ and Y_w at the chute-centerline position of step 23.

	Discharge (m^3/s)									
	0.085	*0.113*	*0.142*	*0.170*	*0.198*	*0.227*	*0.255*	*0.283*	*0.311*	*0.347*
$Y_{0.90}$ (m)	0.024	0.033	0.040	0.047	0.057	0.063	0.069	0.076	0.083	0.096
$\bar{C}$	0.659	0.659	0.643	0.633	0.628	0.614	0.593	0.580	0.565	0.554
Y_w (m)	0.008	0.011	0.014	0.017	0.021	0.024	0.028	0.032	0.036	0.043

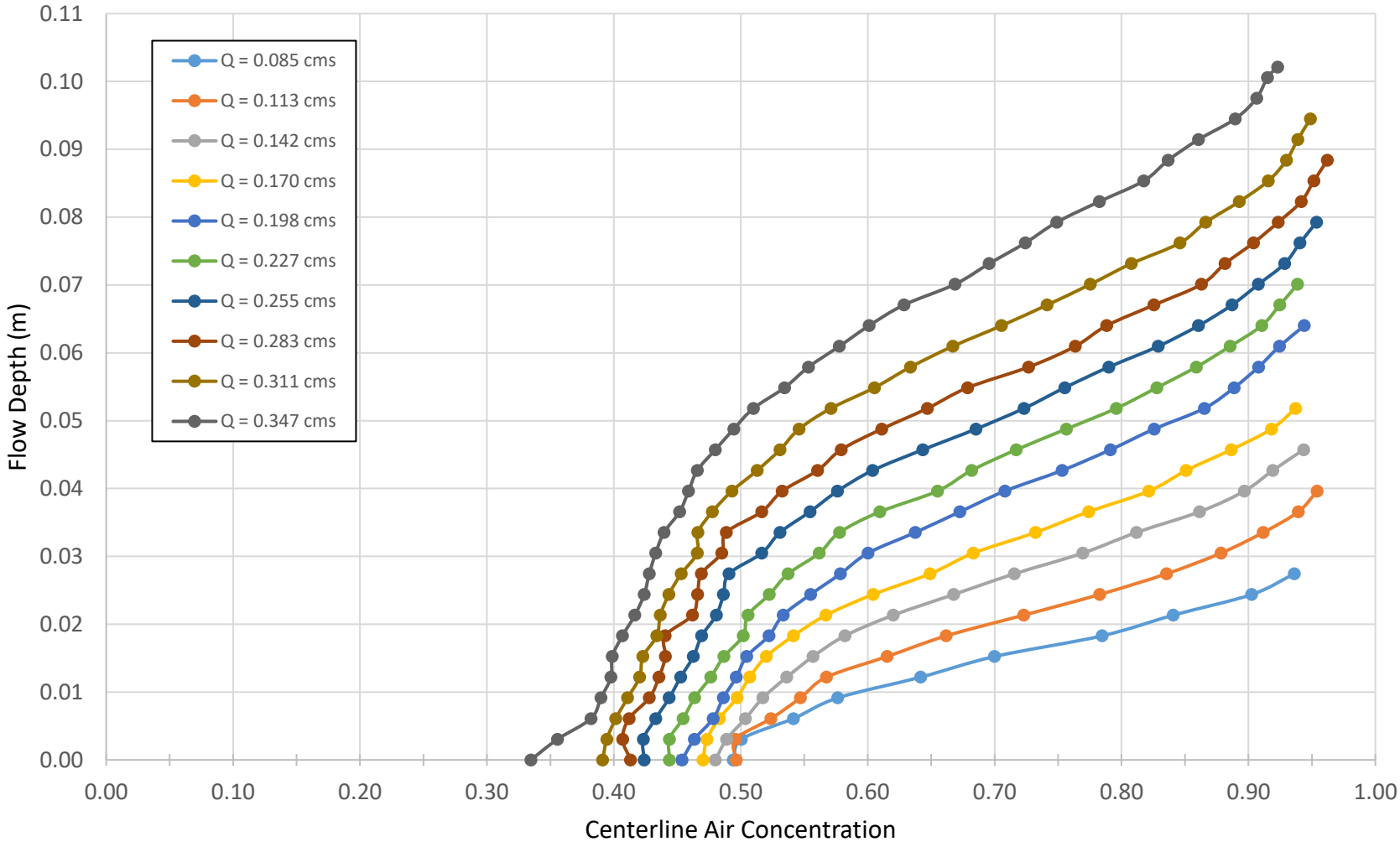
Q = 0.085 cms
Q = 0.113 cms
Q = 0.142 cms
Q = 0.170 cms
Q = 0.198 cms
Q = 0.227 cms
Q = 0.255 cms
Q = 0.283 cms
Q = 0.311 cms
Q = 0.347 cms
Flow Depth (m)
0.00
0.01
0.02
0.03
0.04
0.05
0.06
0.07
0.08
0.09
0.10
0.11
0.00
0.10
0.20
0.30
0.40
0.50
0.60
0.70
0.80
0.90
1.00
Centerline Air Concentration

(a)

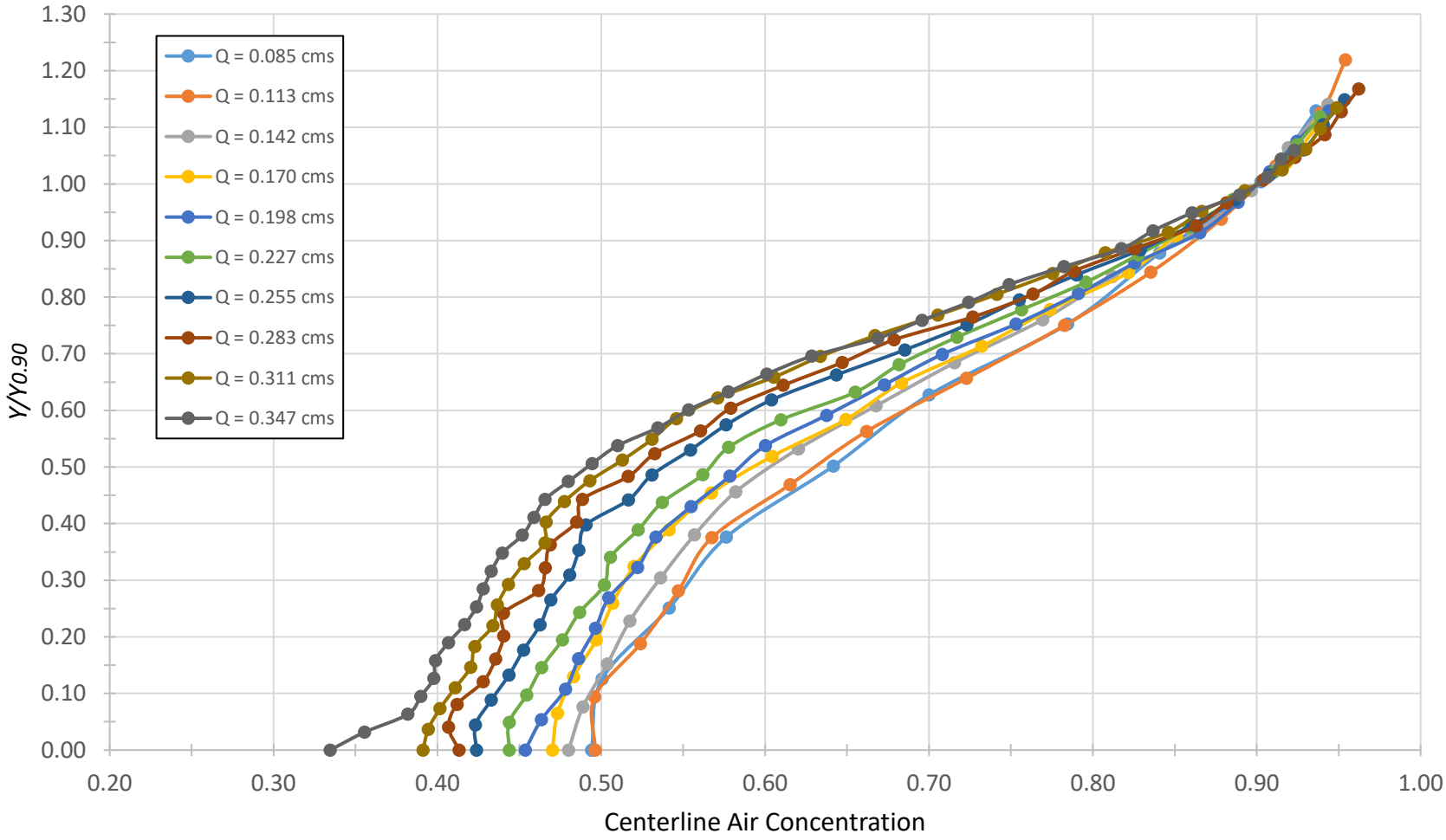

(b)

Figure 4.13. Air-concentration profiles at various water discharges, measured at the chute-centerline position of step 23: (a) dimensional values, and (b) non-dimensional values.

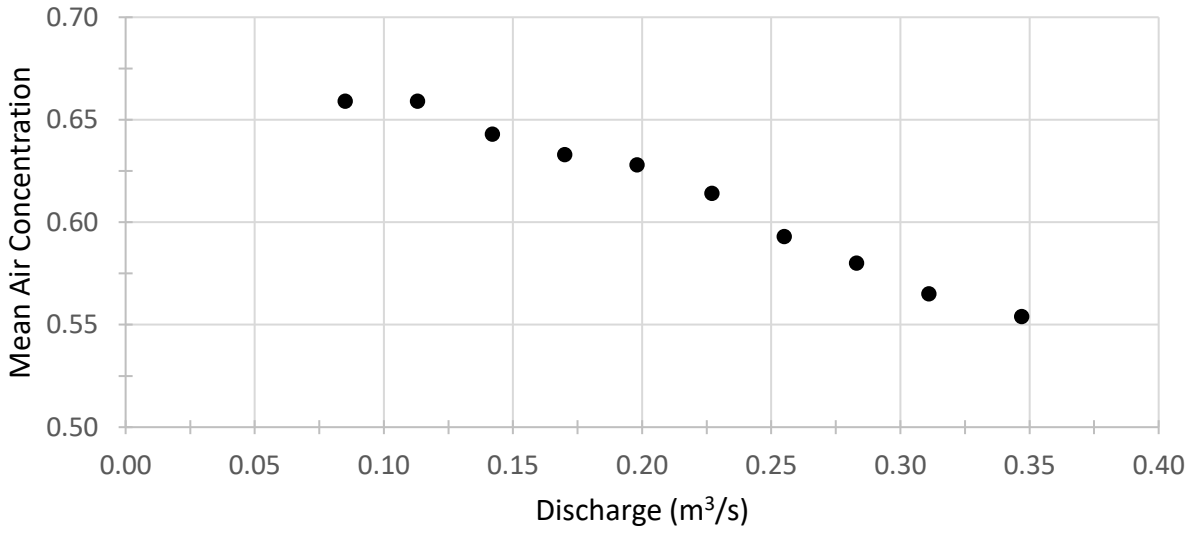

Figure 4.14. Values of depth-averaged air concentration, measured at the chute-centerline position of step 23, plotted as a function of water discharge.

4.3.4 Measurements Across the Chute

The variations of flow depths, $Y_{0.90}$ and Y_w, across the chute at step 23 are shown in Figure 4.16, which consists of two plots. In each plot, chute positions are given as b/B, with B = 1.87 m. A definition sketch is shown in Figure 4.15.

Chute curvature is neglected in Figure 4.16(a). For each measured profile, flow depth is measured relative to the chute invert at that location. In Figure 4.16(b), the chute curvature is accounted for. At each lateral position, the offset of the chute invert is measured using the point gage with reference to the right sidewall as the elevation zero. At the chute centerline of step 23, the invert's offset was 0.018 m.

The chute curvature produced a non-uniform flow depth across the section. At the chute centerline, flow achieved a maximum depth of 0.096 m, nominally about 30% greater than near the sidewall where the flow depth was 0.077 m. The minimum flow depth, 0.071 m, occurred within the range $0.21 < b/B < 0.29$.

The additional flow depth along the chute centerline was more-or-less commensurate with the offset of the chute invert, as seen in Figure 4.16(b), where, accounting for the offset, the centerline water surface was in-line with the sidewall.

By comparing water-surface elevations on either side of the chute-centerline position (b/B = 0.50), it was concluded that flow within the chute was symmetrical about the centerline. For example, comparing points b/B = 0.25 and 0.75 (or 0.42 and 0.58), measured values of $Y_{0.90}$ agreed to within 1.0 mm. For this reason, the mounting apparatus of the point-gage assembly, which precluded measurements of air concentration within the approximate range 0.75 < b/B < 1.0, was considered adequate for assessing the lateral trends.

Figure 4.17 shows a scatter-plot of the air concentration data for all lateral positions measured. At b/B = 0.50, the mean concentration of entrained air was lowest: $\bar{C}$ = 0.554. This location, where $\bar{C}$ was minimum corresponds with the location where flow depth was maximum. Similarly, $\bar{C}$ reached a maximum value of about 0.608 where flow depth was minimum, between 0.21 < b/B < 0.29.

Figure 4.15. A definition sketch of the non-dimensional chute positions, b/B

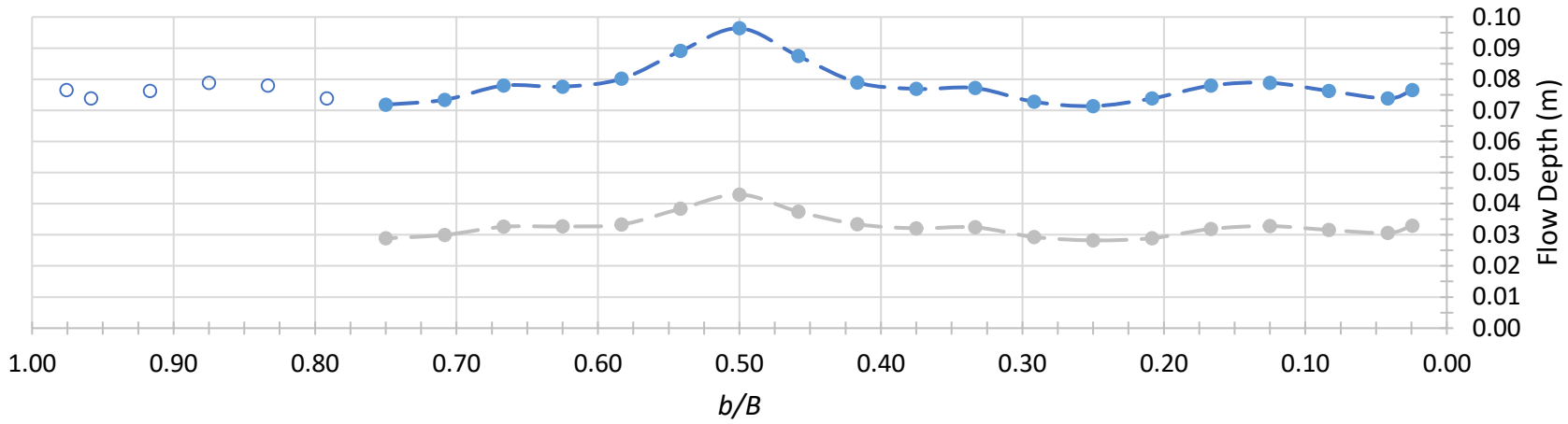

(a)

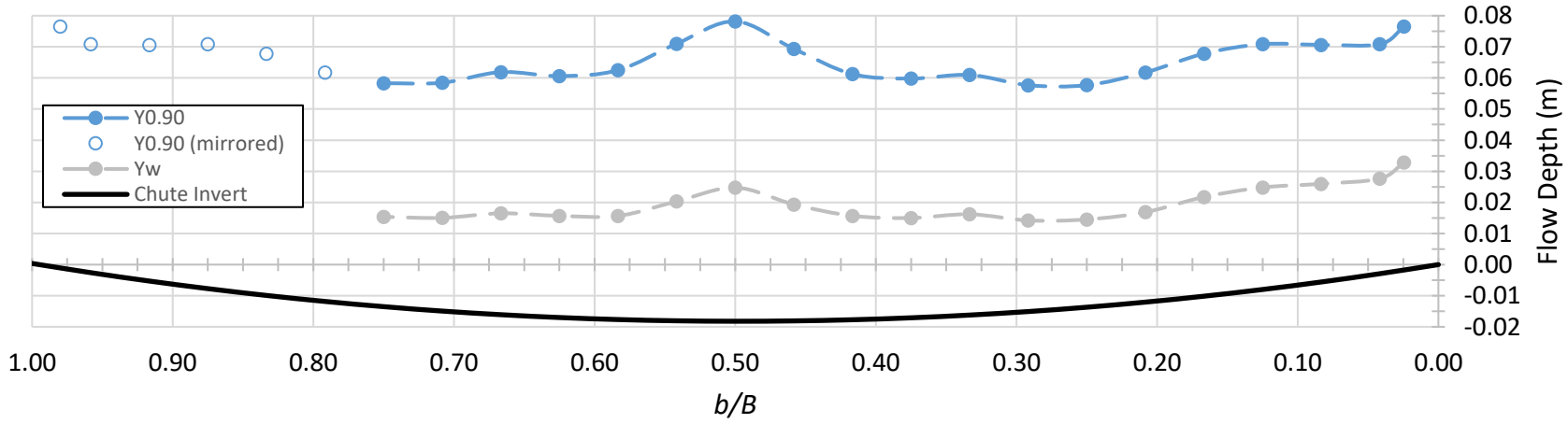

(b)

Figure 4.16. The lateral variations across step 23 of $Y_{0.90}$ and Y_w when the chute conveyed the design discharge; (a) w/o curvature, and (b) w/ curvature.

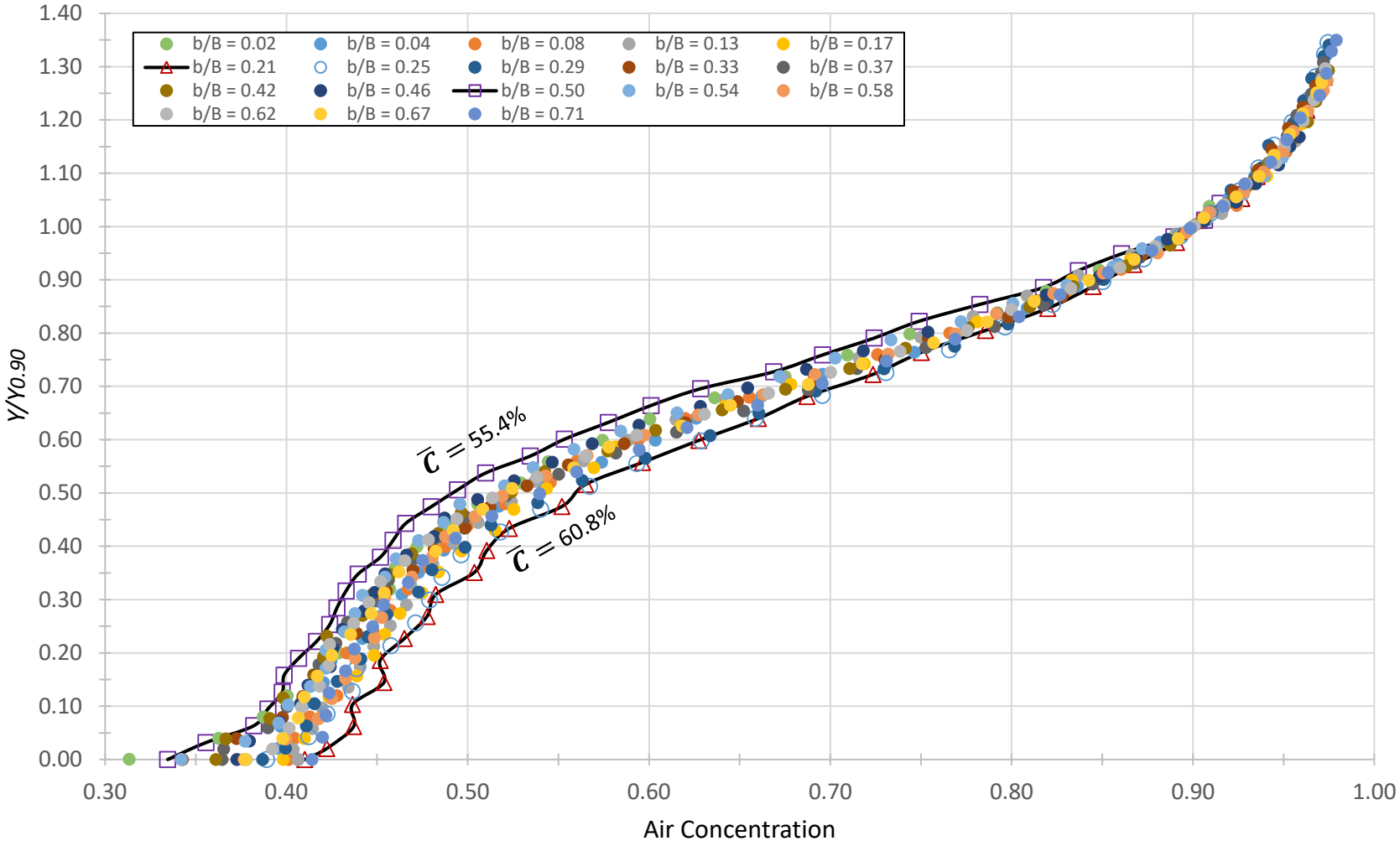

Figure 4.17. A scatter plot of air-concentration profiles collected across step 23 when the chute conveyed the design discharge.

Table 4.5. The distributions across the chute of $Y_{0.90}$, $\bar{C}$ and Y_w when the chute conveyed the design discharge.

	b/B																		
	0.02	*0.04*	*0.08*	*0.13*	*0.17*	*0.21*	*0.25*	*0.29*	*0.33*	*0.37*	*0.42*	*0.46*	*0.50*	*0.54*	*0.58*	*0.62*	*0.67*	*0.71*	*0.75*
$Y_{0.90}$ (m)	0.077	0.074	0.076	0.079	0.078	0.074	0.071	0.073	0.077	0.077	0.079	0.087	0.096	0.089	0.080	0.078	0.078	0.073	0.072
$\bar{C}$	0.570	0.586	0.586	0.584	0.591	0.608	0.605	0.597	0.580	0.583	0.577	0.572	0.554	0.569	0.584	0.579	0.582	0.592	0.598
Y_w (m)	0.033	0.031	0.032	0.033	0.032	0.029	0.028	0.029	0.032	0.032	0.033	0.037	0.043	0.038	0.033	0.033	0.033	0.030	0.029

4.3.4.1 Sidewall Effect

The chute was sufficiently wide that the effect on the overall flow field of the chute sidewall was localized to near the sidewall. As previously reported by Kramer (2004), air-concentration profiles are unaffected by the sidewall (though velocity profiles are, as this study affirms). This section compares more closely the sidewall profile and profiles measured at adjacent lateral positions, and the positions where $\bar{C}$ were measured as being the highest and lowest. The profile at chute position $b/B = 0.02$ nearly coincides with profiles measured at positions $b/B = 0.04$, 0.08. The chute's curvature and upstream piers produced more profile variability across the chute than did the sidewall; e.g., $b/B = 0.21$ and 0.50.

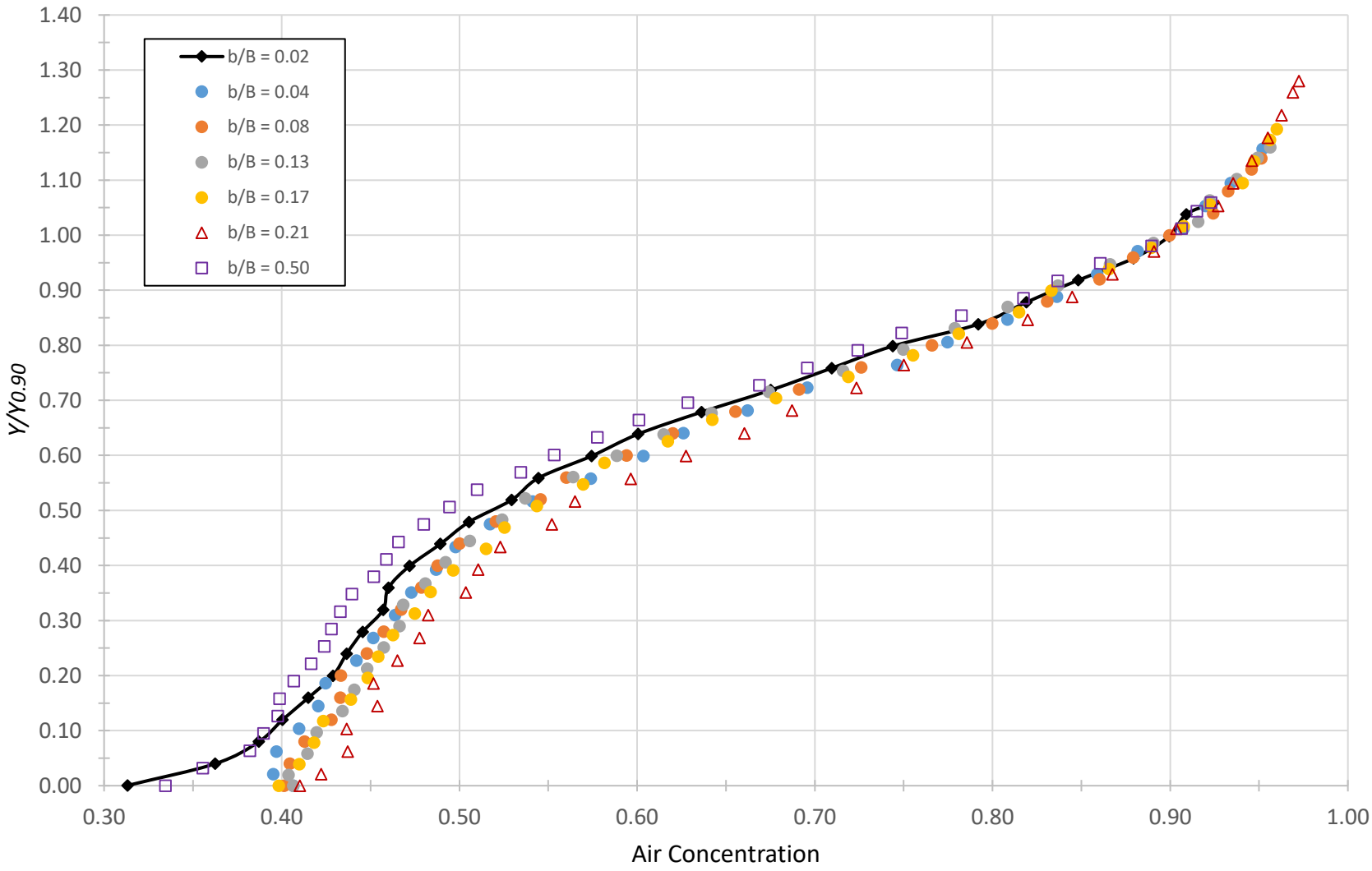

Figure 4.18. A comparison of air-concentration profiles at/near the chute sidewall (showing negligible influence of sidewall boundary layer on measured values of air concentration).

4.3.5 Repeatability of Water-Surface Measurements

The water surface was defined as the flow depth where the time-averaged air concentration was 0.90. However, the depth $Y_{0.90}$ was never measured directly. Using the point-gage assembly to increment the sampling depths, each profile was sampled at discrete points and hence $Y_{0.90}$ was interpolated using the neighboring points along the profile, $Y(C < 0.90)$ and $Y(C > 0.90)$.

To assess the accuracy of the values of $Y_{0.90}$ estimated (and presented in Section 4.3.4), experiments were untaken so that some of the measurements were repeated. This section presents the results of two experiments, conducted at lateral positions $b/B = 0.50$ and 0.21. These positions across the chute were chosen specifically for re-analysis of $Y_{0.90}$, because they correspond with the profiles where $\bar{C}$ (depth-averaged) and $Y_{0.90}$ were found to be lowest/highest and highest/lowest, respectively.

4.3.5.1 $b/B = 0.50$

At the chute-centerline position, $b/B = 0.50$, the value of $Y_{0.90}$ (as reported in Section 4.3.4) was 0.096 m. Table 4.6 gives the profile data that produced that value (Run IDs 01 and 02). Also, a total of ten samples were recorded (Run IDs 1 through 10): five at $Y(C < 0.90)$, and five at $Y(C > 0.90)$. The data sets were recorded along subsequent major divisions of the point-gage assembly; i.e. at a spacing normal to the chute invert of 0.01 ft = 3.05 mm. In each set, C is averaged, and the standard deviation σ_C is reported. From those averages, a new $Y_{0.90}$ is interpolated, and found to be 0.095 m. The difference between the reported value in Section 4.3.4 and the value obtained by averaging a total of ten samples, is 1.0 mm. That difference, expressed as a proportion of the flow depth, is about 1.0%. The error can also be expressed in terms of air concentration by considering the mean gradient $\frac{\partial C}{\partial y}$ of the ten samples. From data in (b), $\frac{\overline{\partial C}}{\partial y} \approx 1.6\ \text{ft}^{-1} = 5.2\ \text{m}^{-1}$. Then, $\Delta C = 5.2\ \text{m}^{-1} \int_{Y=0.095\ m}^{Y=0.096\ m} dy$, and the normalized error is thus $\Delta C/C = 0.5\%$ (where $C = 0.90$).

Table 4.6. Repeated measurements of the value $Y_{0.90}$ along the chute's centerline position of step 23 when the chute conveyed its design discharge. Run IDs 01-02 are the measurements that produced the original value of $Y_{0.90}$ (0.096 m), and IDs 1-10 are the repeated measurements that produced the new value ($Y_{0.90}$ = 0.095 m).

Run ID	Flow Depth, Y (m)	Air Concentration, C
01	0.094	0.890
02	0.098	0.906
		$Y_{0.90}$ = 0.096 m
1	0.094	0.895
2		0.896
3		0.895
4		0.893
5		0.897
	Average	C = 0.895 σ_C =0.001
6	0.098	0.911
7		0.910
8		0.909
9		0.913
10		0.911
	Average	C = 0.911 σ_C =0.002
		$Y_{0.90}$ = 0.095 m

4.3.5.2 *b/B* = 0.21

Profile data for the chute position *b/B* = 0.21 are given below in Table 4.7. At this position, $Y_{0.90}$ was reported in Section 4.3.4 to be 0.074 m. The profile data that produced the original value of $Y_{0.90}$ are given by Run IDs 01-02.

Five additional samples were recorded at the flow depth Y = 0.075 m (Run IDs 1-5). This flow depth was considered for additional measurements because it nearly coincided with $Y_{0.90}$: as data in Table 4.7 show, C (*at* Y = 0.075 m) = 0.90.

In Table 4.7, the five measured values of C are averaged. The results indicate that, at the measured flow depth, C = 0.898 ± 0.002 = 0.90. Comparing this result with the value of $Y_{0.90}$ as reported in Section 4.3.4, the difference is ~1.0 mm, and $\Delta C/C$ ~ 0.5%

Table 4.7. Repeated measurements of the value $Y_{0.90}$ at chute position b/B = 0.21 of step 23 when the chute conveyed its design discharge. Run IDs 01-02 are the measurements that produced the original value of $Y_{0.90}$ (0.074 m), and IDs 1-5 are the repeated measurements at the flow depth Y = 0.075 m.

Run ID	Flow Depth, Y (m)	Air Concentration, C
01	0.072	0.891
02	0.075	0.904
		$Y_{0.90}$ = 0.074 m
1	0.075	0.895
2		0.896
3		0.895
4		0.893
5		0.897
	Average	C = 0.898 σ_C =0.002 $Y_{0.90} \approx$ 0.075 m

4.3.6 Time-Series Record of Air-Concentration Data

Air-concentration data were analyzed as time-series to assess fluctuations of C. The time-series presented in this section complement the error analysis in Section 4.3.5 and were generated using a moving-average function in MATLAB. The input for this analysis were the conductivity

probe's raw voltage data and a prescribed time-duration of the averaging window, T_w, over which the moving average was calculated (i.e. a sub-interval of the total sample). Values obtained from the moving-average function were evaluated in terms of the actual mean value. The actual mean was taken as the average value over the full sample duration. From this analysis, the standard deviation, σ_C, was determined for each T_w. With increasing T_w, the moving-average function yielded values of air concentration which approached the actual mean; i.e., $\sigma_C \rightarrow 0$.

This section presents time-series generated at two different water discharges. In Section 4.3.5.1, σ_C is evaluated at the chute's design discharge, and in Section 4.3.5.2 the time-series of C is examined for a low water discharge in which roll waves were present along the chute.

4.3.6.1 Design Discharge

At the chute's design discharge, time-series were generated in a section of equilibrium flow at four positions across the chute, and at two flow depths per position. The following positions across step 23 were chosen for the time-series analysis: b/B = 0.02, 0.21, 0.29 and 0.50. These positions were chosen for analysis because of the following considerations:

1. Step 23 was a region of nominally equilibrium flow conditions.
2. The measured profile at b/B = 0.21 had the highest value of $\bar{C}$ (0.608), whereas the profile at b/B = 0.50 had the lowest value of $\bar{C}$ (0.554).
3. Similarly, (as presented in Section 4.4.3), the profile at b/B = 0.02 had the lowest value of $\bar{V}$ (5.06 m/s), while the profile at b/B = 0.29 had the highest value (5.84 m/s).

The time-series were generated for flow elevations $Y = 0$ and $Y = Y_{0.90}$, and for three averaging windows: T_w = 1.0, 5.0 and 10.0 sec. The results of σ_C are given in Table 4.8 and indicate the following points:

1. When averaging was performed over a sliding window of 1.0 sec,
    - Variance in C was most pronounced near the sidewall, b/B = 0.02. At the chute invert σ_C was 1.7%, and at the water surface was 1.9%.
    - C was slightly steadier along the chute centerline, b/B = 0.50; σ_C at the chute invert was 1.4%, and at the water surface was 0.7%.

2. When data were averaged over a window of 10.0 sec,
    - At every chute position and flow depth, variance in C was less than 0.5%.

The results confirm the stated accuracy of the conductivity probe. Chanson (1996) reported that $\Delta C/C < 2.0\%$, while Felder & Chanson (2014) reported $\Delta C/C < 4.0\%$. Bung (2013) stated $\Delta C/C < 5.0\%$ when the sample duration was reduced from 25.0 sec to 1.0 sec.

As Table 4.8 shows, σ_C reached a maximum value of 1.9% when averaging was performed over a sub-interval of 1.0 sec. Yet, because data were sampled for durations of 30.0 and/or 60.0 sec, the accuracy was thereby improved. As Figure 4.17 (b) shows, $\Delta C/C \rightarrow 0$ when averaging was performed over a sufficiently long duration (whereas in Figure 4.17 (a), deviations about the mean are more pronounced).

Table 4.8. Variance in C when data were averaged over sub-intervals of 1.0, 5.0 and 10.0 sec.

			b/B = 0.02	b/B = 0.21	b/B = 0.29	b/B = 0.50
σ_C	$Y = 0$	T_w = 1.0 sec	1.7%	1.4%	1.5%	1.4%
		T_w = 5.0 sec	0.5%	0.4%	0.8%	0.4%
		T_w = 10.0 sec	0.3%	0.2%	0.5%	0.1%
	$Y = Y_{0.90}$	T_w = 1.0 sec	1.9%	1.6%	1.3%	0.7%
		T_w = 5.0 sec	0.4%	0.8%	0.3%	0.3%
		T_w = 10.0 sec	0.1%	0.2%	0.2%	0.2%

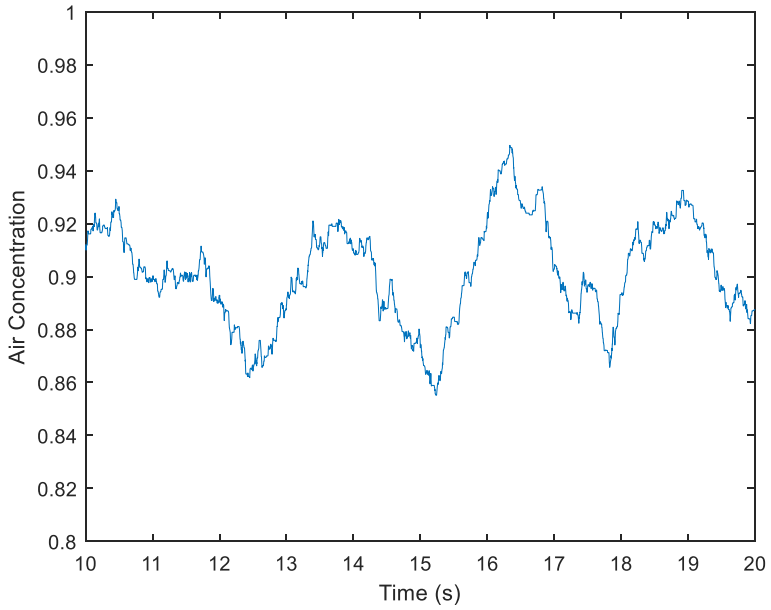

(a)

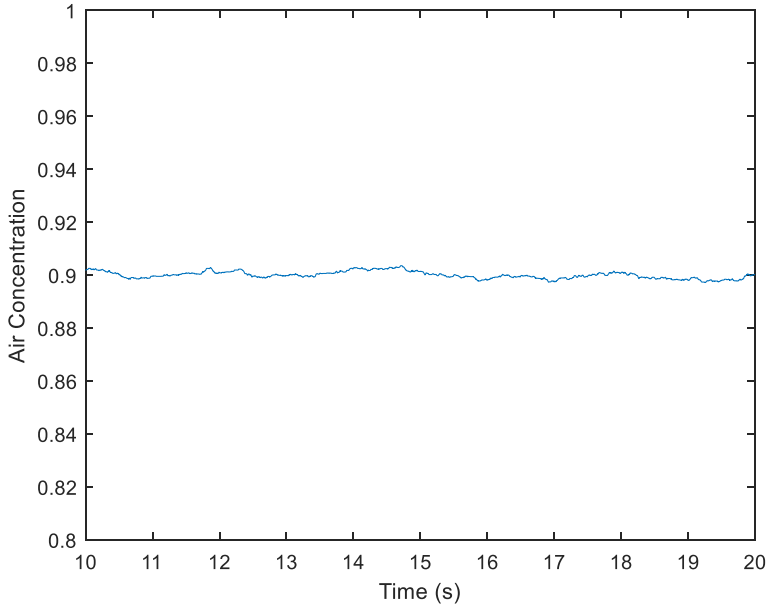

(b)

Figure 4.19. Time-series of C at the chute-sidewall position, b/B = 0.02, at the approximate flow depth $Y_{0.90}$ when the chute conveyed its design discharge. In (a): T_w = 1.0 sec and σ_C = 1.9%; in (b): T_w = 10.0 sec and σ_C = 0.1%.

4.3.6.2 Roll Waves

Following the procedures mentioned above, a time-series of C was generated for a low discharge, about Q = 0.021 m^3/s, in which roll waves were present along the chute. Data were recorded along step 23 at the chute-centerline position, b/B = 0.50, with the probe tips aligned with the chute's pseudo-bottom invert, Y = 0. At this low discharge, the flow depth was unsteady. With each passing roll wave, the water surface tipped up momentarily. The time-series of C is intended to assess the effect on C of the passing roll waves and the frequency of roll-wave passage.

The frequency of the roll waves was estimated using a stopwatch, and was found to be about 0.8 sec. The mean of C was calculated, over the full sample duration of 30 sec, to be 0.692.

At low discharges generally, and in the data set recorded for this analysis, the bubble frequency of the mixture restricted some applications of the moving-average function. For example, if bubbles were detected at a frequency of 200 Hz, while averaging was performed at a sub-interval of T_w = 0.1 sec, then computed values of air concentration were based only on ~20 detected bubbles. Further, as Table 4.8 indicates, even for the design discharge where the bubble frequency is maximum, the variance was about 2.0% for a sub-interval of 1.0 sec. Hence, for a low discharge (Q = 0.021 m^3/s) where the bubble frequency is even less, and where the sub-interval is taken as < 1.0 sec (a shorter period than was estimated by the stopwatch), it is difficult to attribute the variance in C as being caused solely by the role waves and not also by insufficient sampling of the air-water mixture.

Figure 4.20 plots the time-series with T_w = 10.0 sec, which effectively 'drowns out' all roll waves over that sample period and yields very close to the actual mean value.

(a) T_w = 10.0 sec, σ<0.5%; (b) T_w = 1.0 sec, σ=2.0%; (c) T_w = 0.8 sec, σ =2.3%; (d) T_w = 0.4 sec, σ=3.8%; (e) T_w = 0.2 sec, σ=6.3%; (f) 0.1 sec, σ=10.3%.

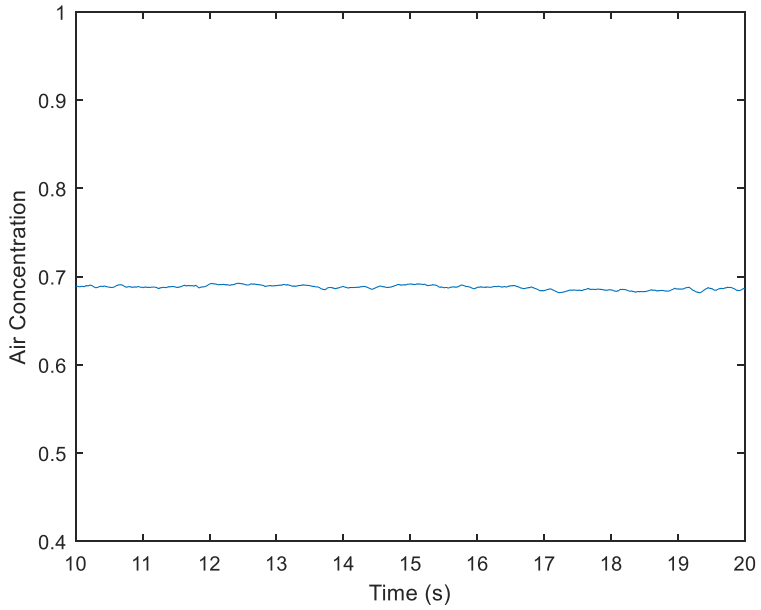
Air Concentration
Time (s)
1
0.9
0.8
0.7
0.6
0.5
0.4
10
11
12
13
14
15
16
17
18
19
20

(a)

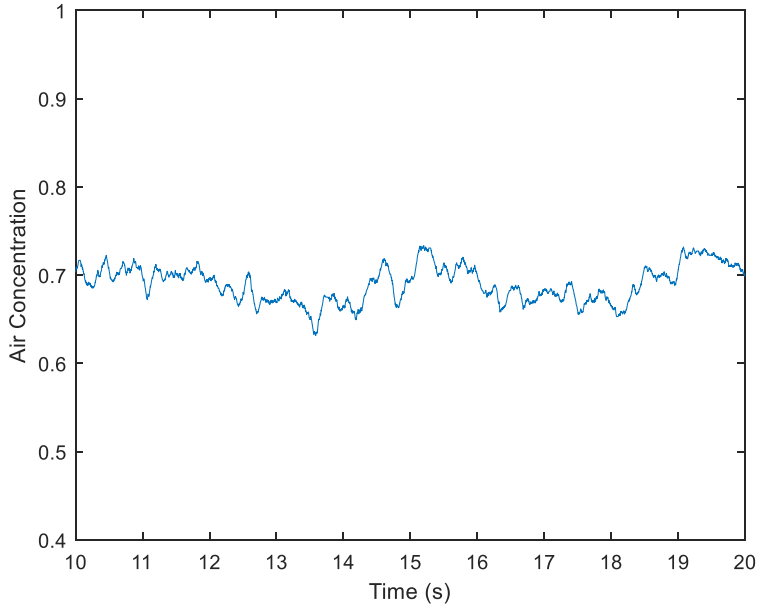
Air Concentration
Time (s)
1
0.9
0.8
0.7
0.6
0.5
0.4
10
11
12
13
14
15
16
17
18
19
20

(b)

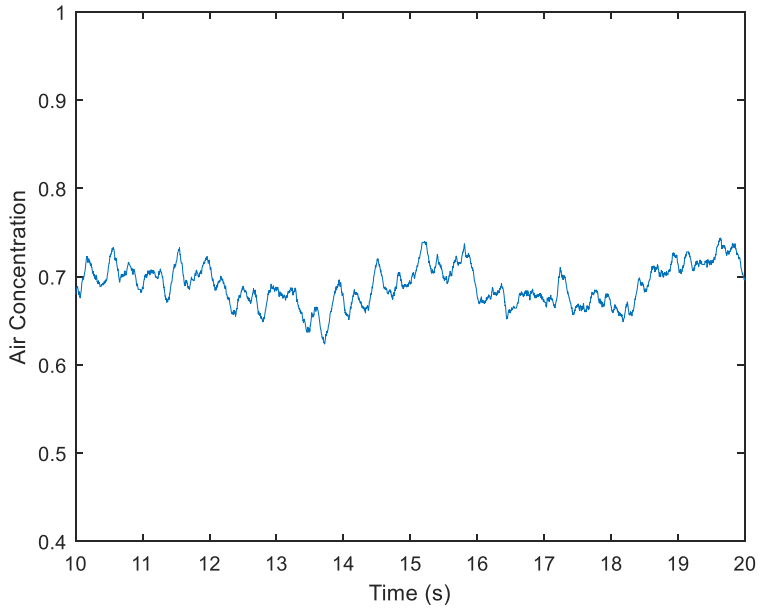
Air Concentration
Time (s)
1
0.9
0.8
0.7
0.6
0.5
0.4
10
11
12
13
14
15
16
17
18
19
20

(c)

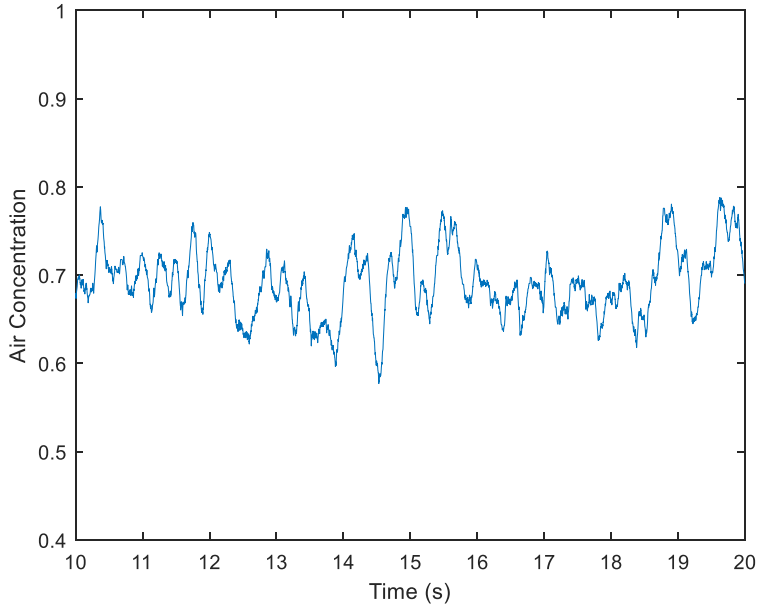
Air Concentration
Time (s)
1
0.9
0.8
0.7
0.6
0.5
0.4
10
11
12
13
14
15
16
17
18
19
20

(d)

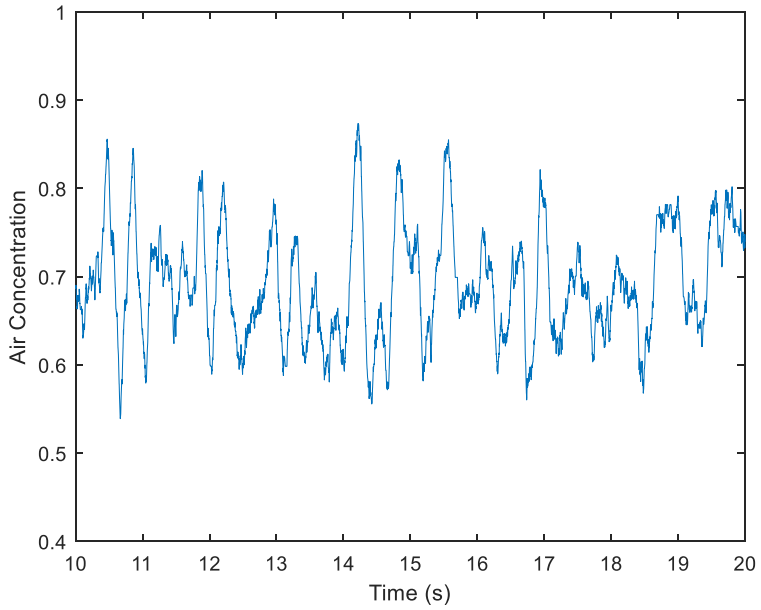

(e)

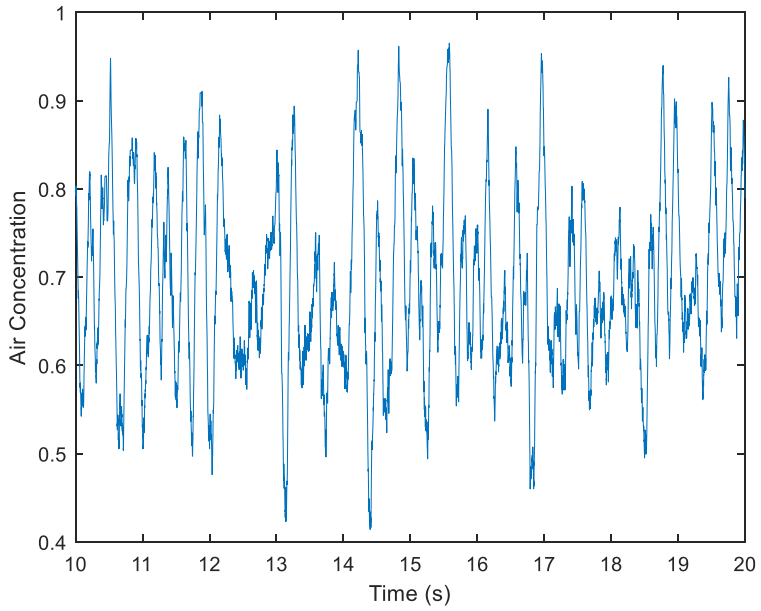

(f)

Figure 4.20. Time-series of C at chute position b/B = 0.33 when the chute conveyed the roll-wave discharge, Q = 0.021 m^3/s. For each value T_w, the standard deviations of the time-series is assessed, and are as follow: (a) T_w = 10.0 sec, σ<0.5%; (b) T_w = 1.0 sec, σ=2.0%; (c) T_w = 0.8 sec, σ =2.3%; (d) T_w = 0.4 sec, σ=3.8%; (e) T_w = 0.2 sec, σ=6.3%; (f) 0.1 sec, σ=10.3%.

4.4 Bulk-Flow Velocity

Each sample of air concentration yielded a corresponding velocity measurement of the air-water mixture (bulked flow), calculated using cross-correlation analysis. Point values were assembled into profiles, as this section presents. Flow depth and velocity are expressed both dimensionally and non-dimensionally. Chute positions are expressed as *b/B*. A power function, of the form $\frac{V}{V_{0.90}} = \left(\frac{Y}{Y_{0.90}}\right)^{1/N}$, as used, approximated every measured profile with $R^2 > 0.90$ (where R^2 is the coefficient of determination.

In this section, each data set is analyzed according to the exponent *N*. The literature reports different values of *N* for turbulent, aerated flows along stepped spillways. It has been noted that values of *N* can vary from one step to the next for a given discharge (Felder & Chanson, 2014). In this thesis, the value of *N* was found to be practically constant down the chute, but varied across the chute and with water discharge.

Values of *N* were obtained from the measured data by performing linear regressions, after log-log transformations were done. The following data pertaining to bulk-flow velocity were obtained within the chute, and are presented in this section:

1. Successive profiles of the bulk-flow velocity obtained along the sidewall in a reach where, at the design discharge, flow transitioned from gradually-varied to nominally equilibrium (in terms of air concentration).
2. Profiles of the bulk-flow velocity obtained for a range of discharges at two chute positions, in a section of equilibrium flow; and,
3. Profiles of the bulk flow velocity obtained at intervals across the chute, in a section of equilibrium flow, at the design discharge.

4.4.1 Measurements Along the Chute Sidewall

Figure 4.21 compares profiles of bulk-flow velocity measured between steps 87 and 23 near the right sidewall of the chute when the spillway conveyed its design discharge. All data were measured 4 cm out from the sidewall (i.e., $b = 0.04$ m). At step 23, where $B = 1.87$ m, that position corresponded with $b/B = 0.02$. Because of the chute's converging width, *b/B* was

slightly less for the higher steps. The plots are presented in two forms: (a) dimensional, and (b) non-dimensional.

Table 4.10 gives values of $Y_{0.90}$, $V_{0.90}$ and $\bar{V}$ for each profile, as well as the exponent N of the power function that best approximates the profiles. The mean value of N is 4.4. The exponent does not appear to be correlated with downstream distance; or, put differently, N was not found to change between regions of gradually-varied and nominally equilibrium flow.

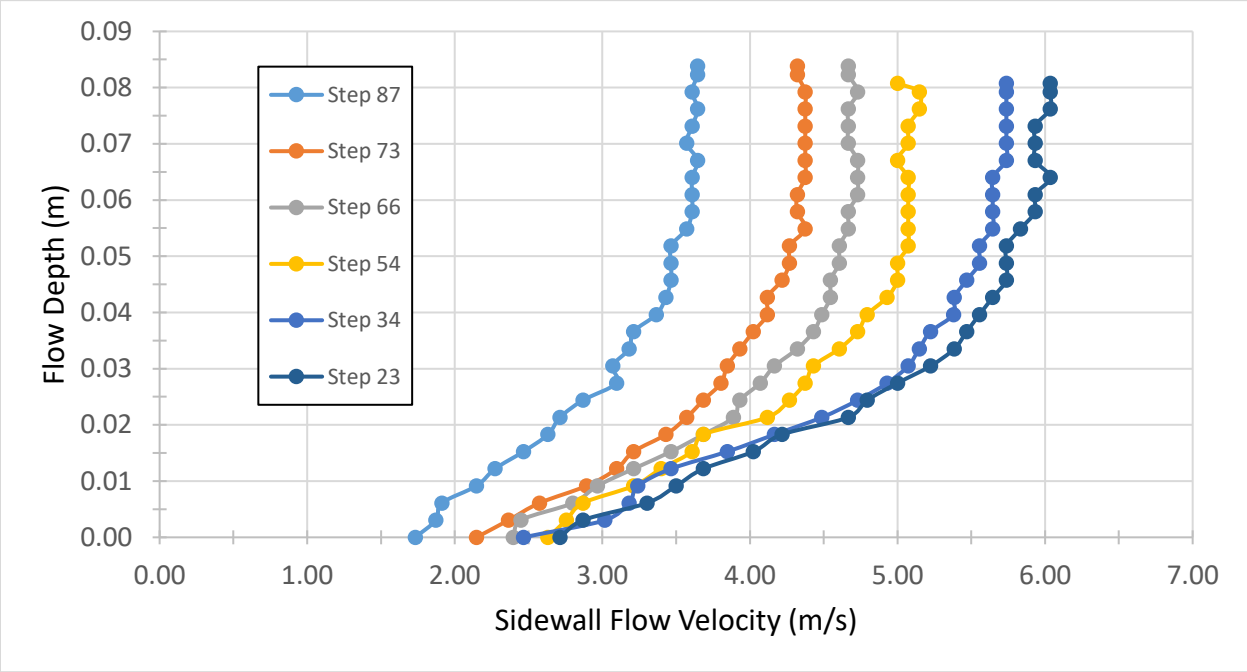

(a)

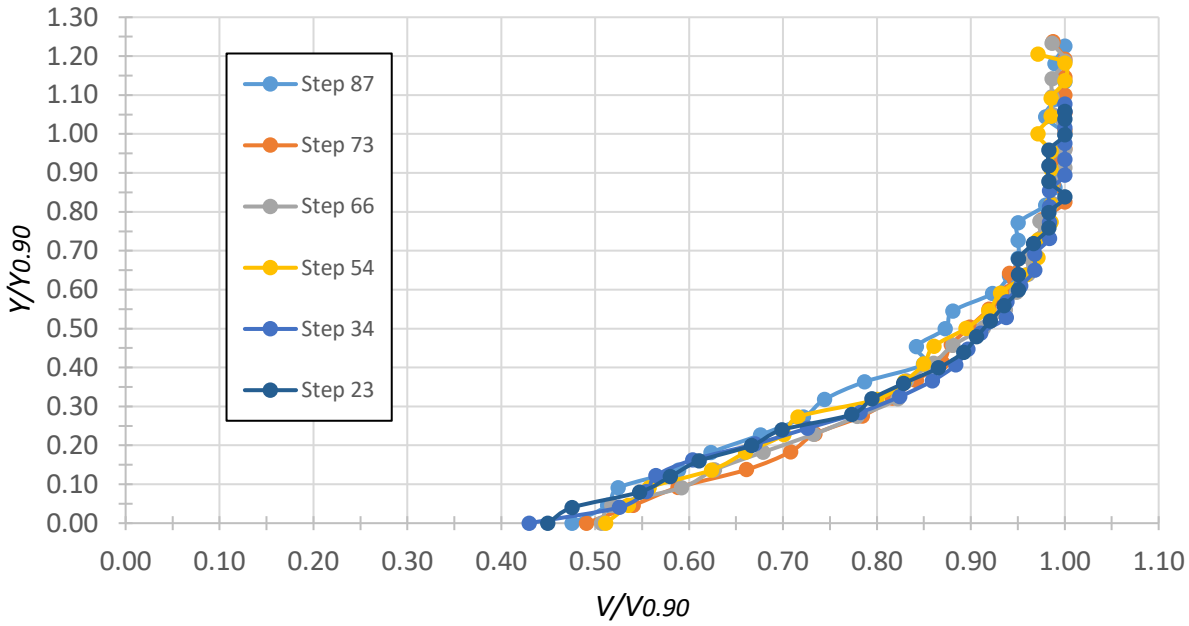

(b)

Figure 4.21. Velocity profiles measured along the right sidewall when the chute conveyed its design discharge, with values expressed: (a) dimensionally, and (b) non-dimensionally.

Table 4.9. Longitudinal variations of $Y_{0.90}$, $V_{0.90}$ and N, measured near the right sidewall when the chute conveyed its design discharge.

	Step No.					
	87	*73*	*66*	*54*	*34*	*23*
$Y_{0.90}$ (m)	0.067	0.067	0.067	0.067	0.075	0.076
$V_{0.90}$ (m/s)	3.65	4.38	4.73	5.15	5.74	6.03
N	4.2	5.1	4.7	4.6	4.4	3.7
R^2	0.96	0.96	0.96	0.94	0.91	0.95

4.4.2 Variation with Water Discharge

This section presents profiles of bulk-flow velocity collected above step 23 for a range of water discharges. The results are shown at two chute positions: near the sidewall (b/B = 0.02), and along the chute centerline (b/B = 0.50). The lowest tested discharge was Q = 0.085 m^3/s.

Subsequent discharges were increased in increments of $\Delta Q = 0.028$ m^3/s, up to $Q = 0.311$ m^3/s; followed, finally, by the design discharge, $Q = 0.347$ m^3/s.

At both positions, the velocity exponent consistently decreased with increasing discharge, discussed further in Section 4.6.3.

4.4.2.1 Sidewall

This section presents profiles of bulk-flow velocity collected above step 23 at the chute-sidewall position ($b/B = 0.02$) for a range of water discharges. The data plotted in Figure 4.22 are listed in Table 4.10**Error! Reference source not found.**. In Figure 4.23, the exponents N that best approximate the respective profiles are plotted as functions of water discharge.

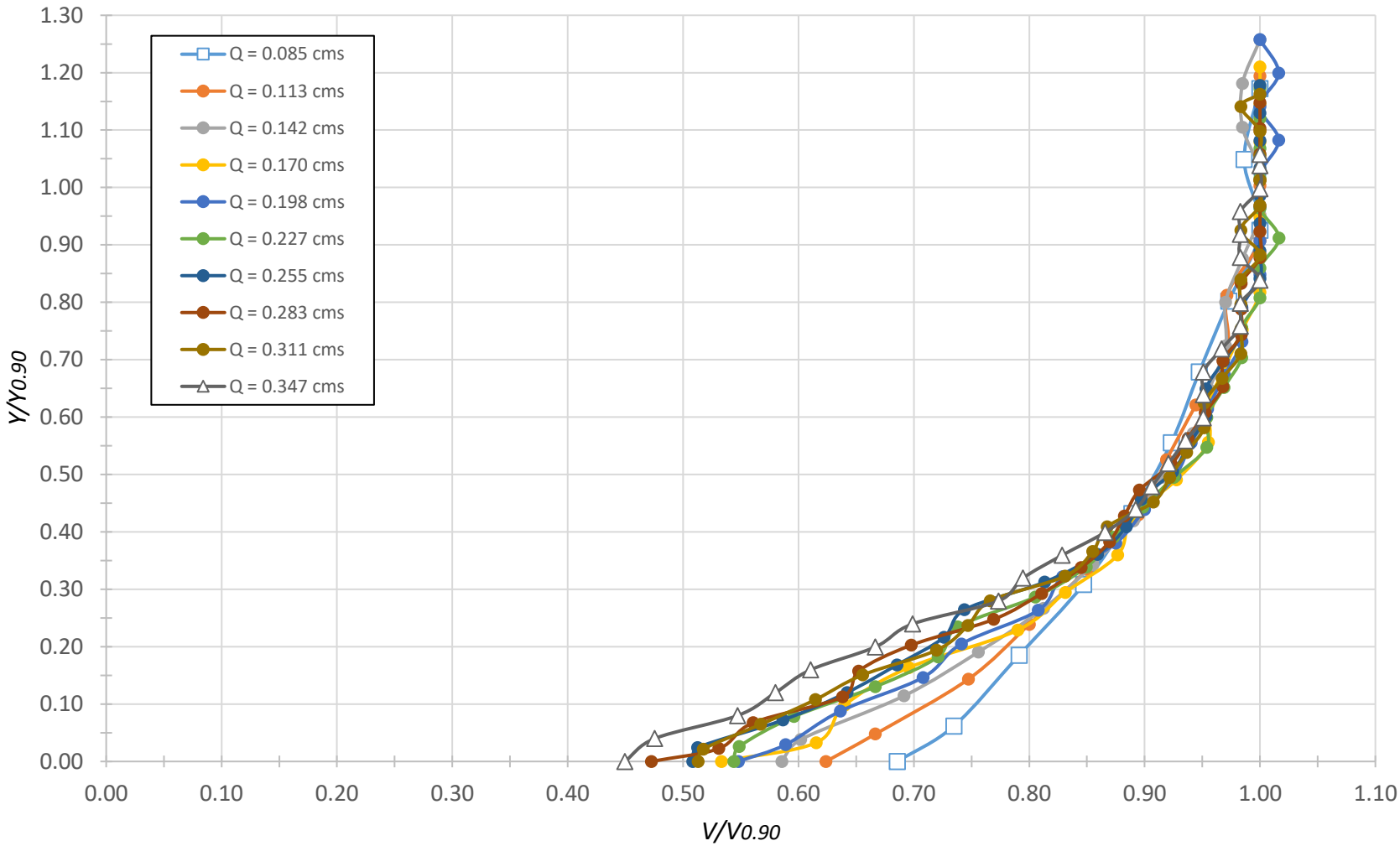

Figure 4.22. Non-dimensional velocity profiles measured for various water discharges at the chute-sidewall position of step 23.

Table 4.10. Variations with water discharge of $Y_{0.90}$, $V_{0.90}$ and N at the chute-sidewall position of step 23.

		Discharge (m^3/s)								
	0.085	*0.113*	*0.142*	*0.170*	*0.198*	*0.227*	*0.255*	*0.283*	*0.311*	*0.347*
$Y_{0.90}$ (m)	0.025	0.032	0.040	0.047	0.052	0.059	0.063	0.068	0.071	0.076
$V_{0.90}$ (m/s)	4.86	5.15	5.38	5.47	5.56	5.65	5.74	5.83	5.93	6.03
N	8.0	7.1	6.3	6.1	6.1	5.5	5.2	5.2	5.2	4.3
R^2	0.97	0.99	0.98	0.94	0.96	0.95	0.96	0.95	0.95	0.94

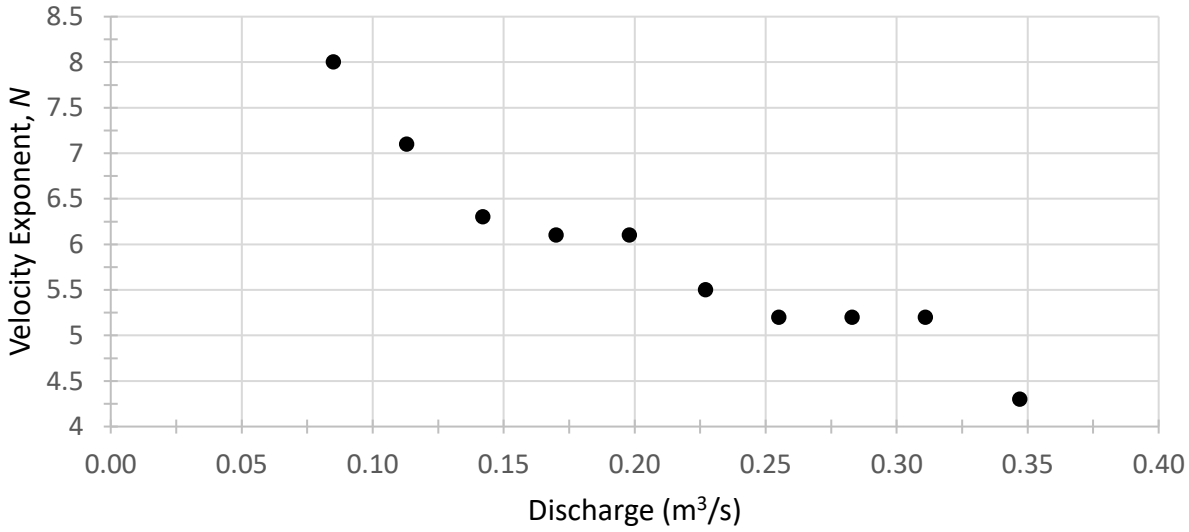

Figure 4.23. Variations with water discharge of N at the chute-sidewall position of step 23.

4.4.2.2 Centerline

This section presents profiles of bulk-flow velocity collected above step 23 at the chute-centerline position (b/B = 0.50) for a range of water discharges. The data plotted in Figure 4.24 are listed in Table 4.11. In Figure 4.25, the exponents N that best approximate the respective profiles are plotted as functions of water discharge.

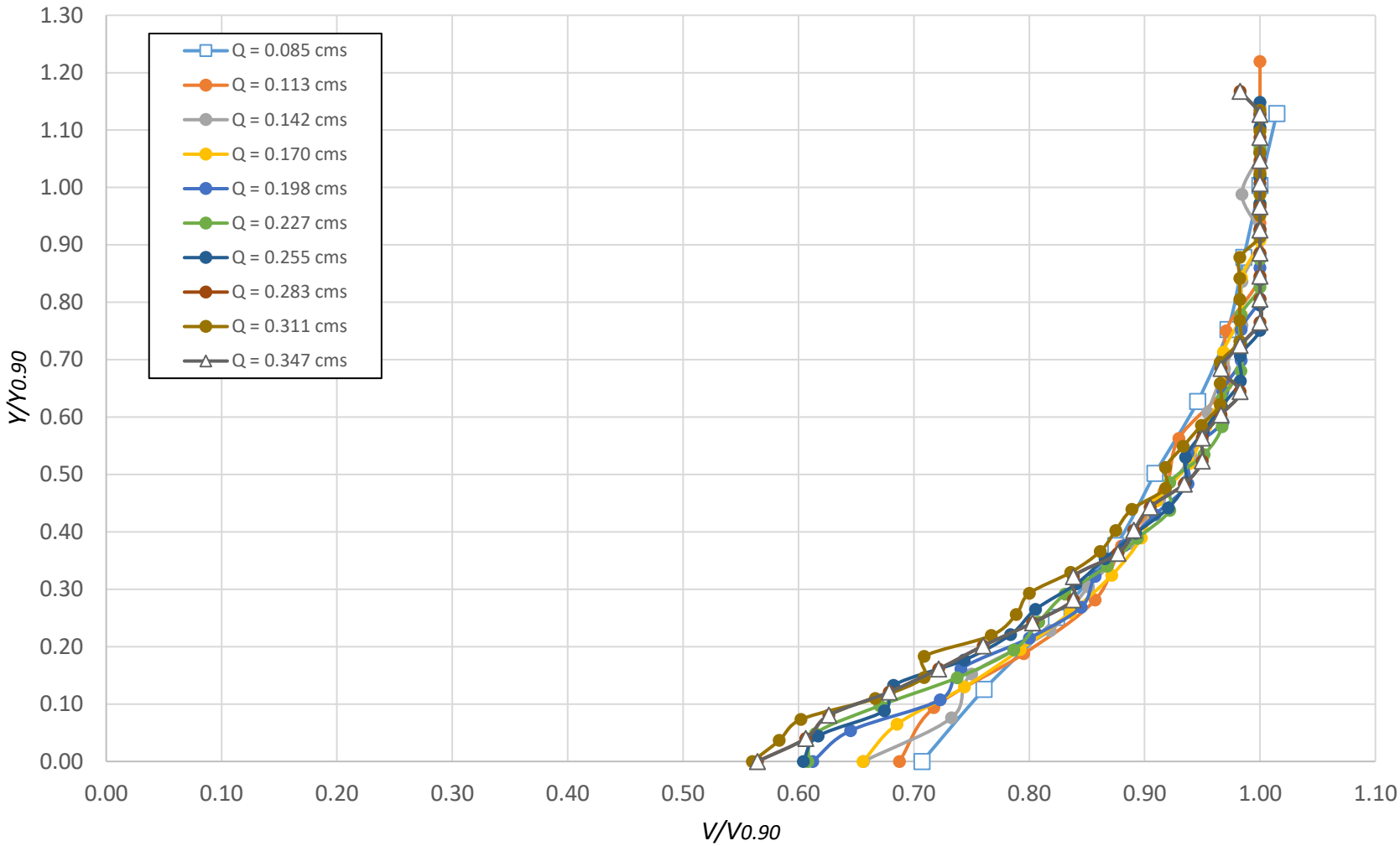

Figure 4.24. Non-dimensional profiles of bulk-flow velocity for various water discharges at the chute-centerline position of step 23.

Table 4.11. Variations with water discharge of $Y_{0.90}$, $V_{0.90}$ and N at the chute-centerline position of step 23.

		Discharge (m^3/s)								
	0.085	*0.113*	*0.142*	*0.170*	*0.198*	*0.227*	*0.255*	*0.283*	*0.311*	*0.347*
$Y_{0.90}$ (m)	0.024	0.033	0.040	0.047	0.057	0.063	0.069	0.076	0.083	0.096
$V_{0.90}$ (m/s)	5.00	5.30	5.55	5.74	5.83	5.93	6.03	6.14	6.25	6.31
N	7.5	7.4	7.6	7.4	6.9	6.5	6.3	6.1	5.7	5.5
R^2	0.99	0.98	0.97	0.98	0.96	0.95	0.95	0.94	0.96	0.95

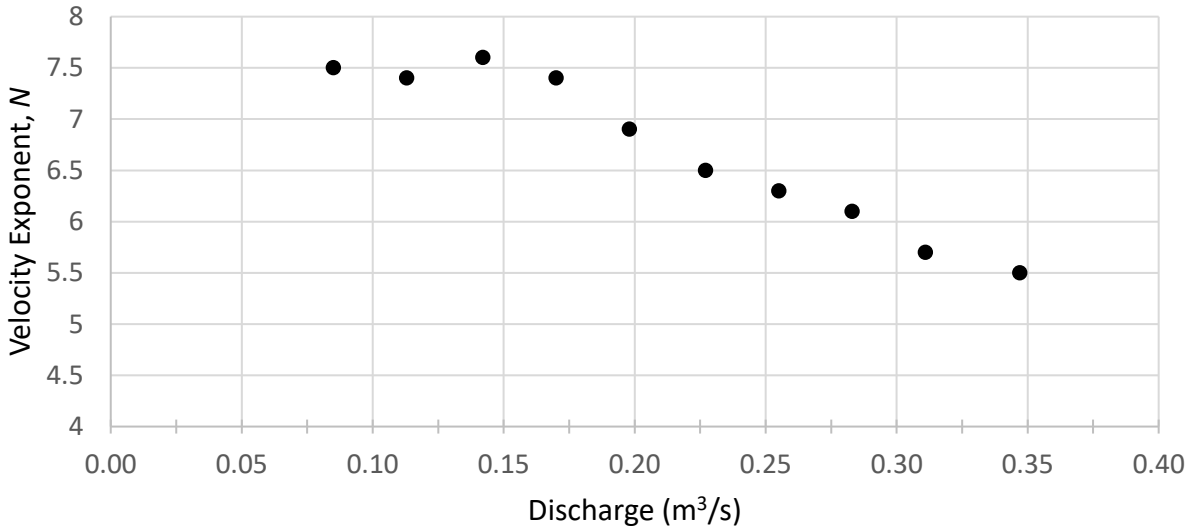

Figure 4.25. Variations with water discharge of N at the chute-centerline position of step 23.

4.4.3 Measurements Across the Chute

The data of bulk-flow velocity collected across step 23 when the chute conveyed its design discharge are presented in this section, in the form of a scatter plot (Figure 4.26). From those profiles, pertinent data are listed in Table 4.13.

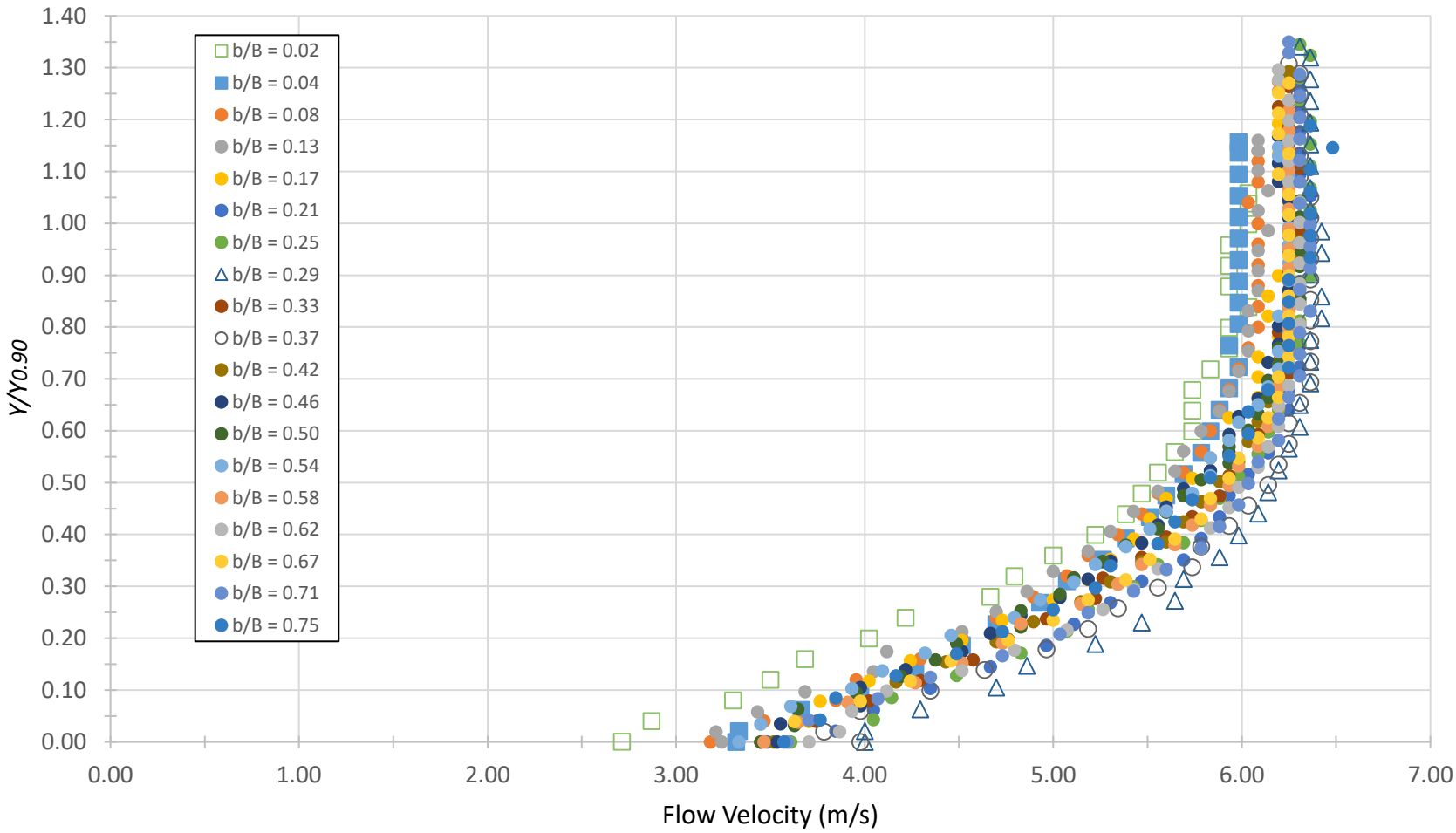
b/B = 0.02
b/B = 0.04
b/B = 0.08
b/B = 0.13
b/B = 0.17
b/B = 0.21
b/B = 0.25
b/B = 0.29
b/B = 0.33
b/B = 0.37
b/B = 0.42
b/B = 0.46
b/B = 0.50
b/B = 0.54
b/B = 0.58
b/B = 0.62
b/B = 0.67
b/B = 0.71
b/B = 0.75
Y/Y0.90
1.40
1.30
1.20
1.10
1.00
0.90
0.80
0.70
0.60
0.50
0.40
0.30
0.20
0.10
0.00
0.00
1.00
2.00
3.00
4.00
5.00
6.00
7.00
Flow Velocity (m/s)

(a)

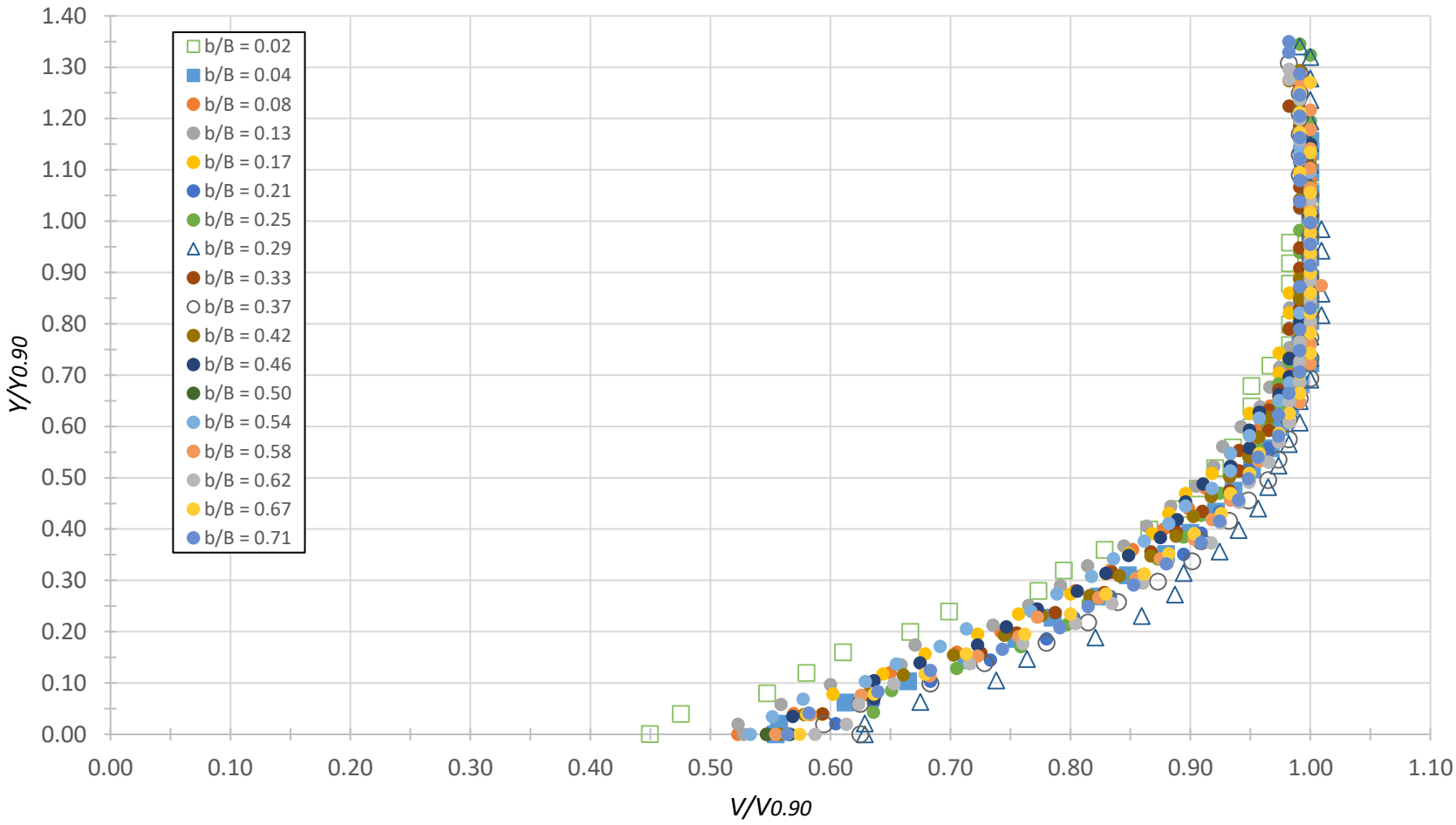

Figure 4.26. A scatter plot of the profile data pertaining to bulk-flow velocity, collected across step 23 when the chute conveyed its design discharge. Values of the bulk-flow velocity are expressed: (a) dimensionally, and (b) non-dimensionally.

Table 4.12. Values of $V_{0.90}$, $\bar{V}$ and N across the chute, measured along step 23 when the chute conveyed its design discharge.

	b/B																		
	0.02	*0.04*	*0.08*	*0.13*	*0.17*	*0.21*	*0.25*	*0.29*	*0.33*	*0.37*	*0.42*	*0.46*	*0.50*	*0.54*	*0.58*	*0.62*	*0.67*	*0.71*	*0.75*
$V_{0.90}$ (m/s)	6.03	5.98	6.09	6.14	6.25	6.36	6.36	6.36	6.31	6.36	6.31	6.25	6.31	6.25	6.25	6.31	6.25	6.36	6.36
$\bar{V}$ (m/s)	5.06	5.30	5.30	5.24	5.40	5.67	5.64	5.84	5.54	5.74	5.53	5.45	5.46	5.41	5.56	5.65	5.55	5.66	5.50
N	4.2	6.2	5.6	5.2	5.5	6.9	5.5	8.1	6.1	6.9	5.8	5.7	5.5	5.3	6.1	6.8	6.1	6.1	5.5
R^2	0.94	0.94	0.96	0.96	0.95	0.94	0.95	0.91	0.95	0.91	0.94	0.96	0.95	0.95	0.92	0.90	0.92	0.90	0.96

The average value of N, from Table 4.12, is about 6.0, and standard deviation is 0.80. The range $5 < N < 7$ encompassed 90% of the measured profiles (all except $b/B = 0.02, 0.29$). The profiles falling within that range are plotted in Figure 4.27, along with the power functions representing $N = 5$ and 7. Between $0.40Y_{0.90} < Y < 0.90Y_{0.90}$, the measured velocity data is consistently about 5.0% to 10.0% greater than the value predicted by the power function, suggesting that a power function does not represent the normalized velocity profile to as great an extent as previous researchers have found.

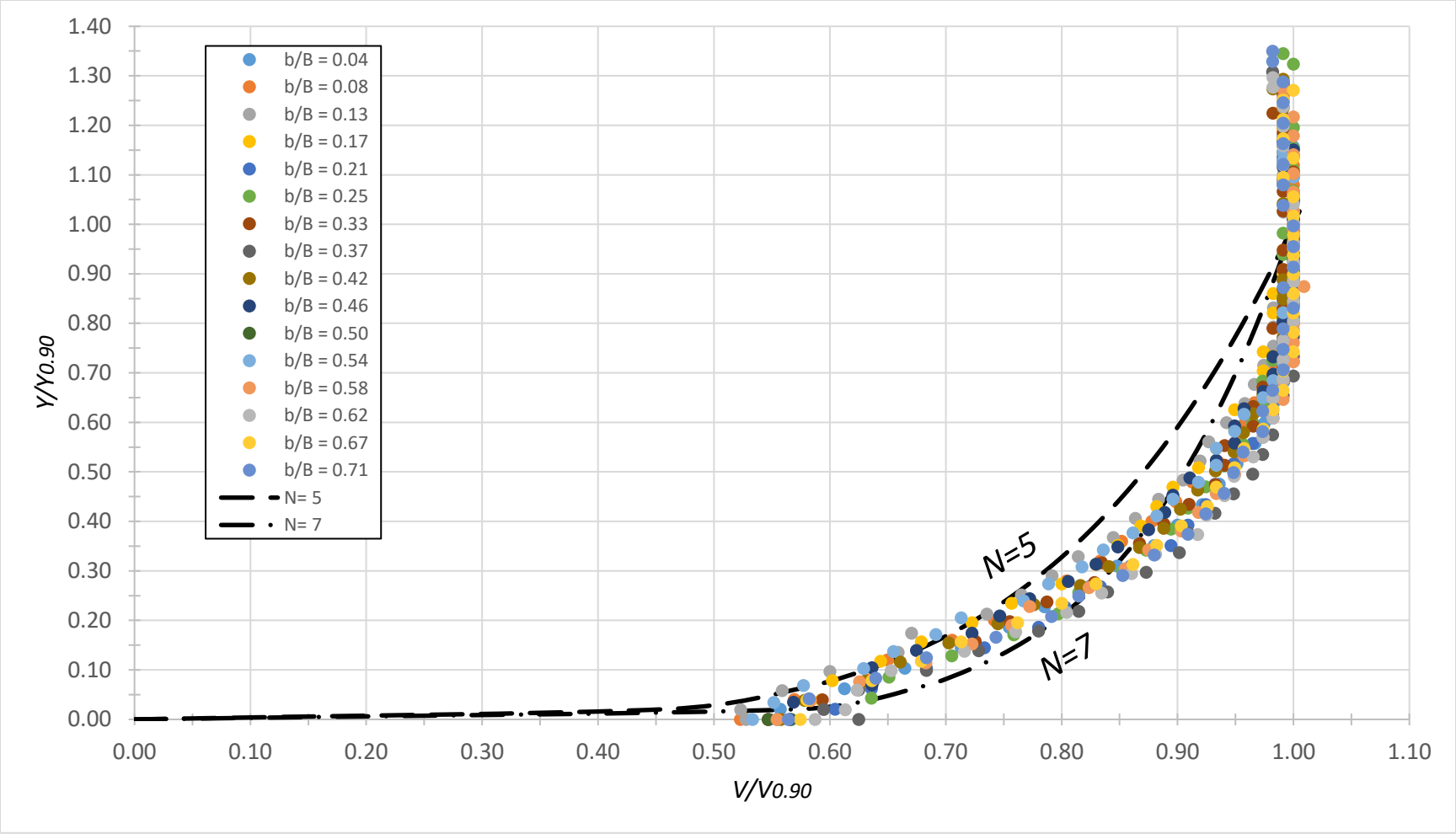

Figure 4.27. A comparison of the measured data pertaining to bulk-flow velocity (Figure 4.26) with the best-fit power functions $N = 5$ and 7.

The two outliers of the range $5 < N < 7$ ($b/B = 0.02$ and 0.29) are plotted separately in Figure 4.28 and Figure 4.29. Those plots indicate the following:

1. At the chute-sidewall position, $b/B = 0.02$, velocity is hindered for $Y < 0.40Y_{0.90}$, but above that the profile is well approximated by the power function. These findings comport with previous observations of the sidewall boundary layer and its effect on the velocity field – e.g., Kramer (2004), who found that flow velocities were reduced in the vicinity of the sidewall by as much as 10%; whereas,
2. At the chute position $b/B = 0.29$, the power function works well for $Y < 0.40Y_{0.90}$, but for flow depths above that value, the measured magnitude of the bulk-flow velocity is appreciably higher than is predicted by the power function.

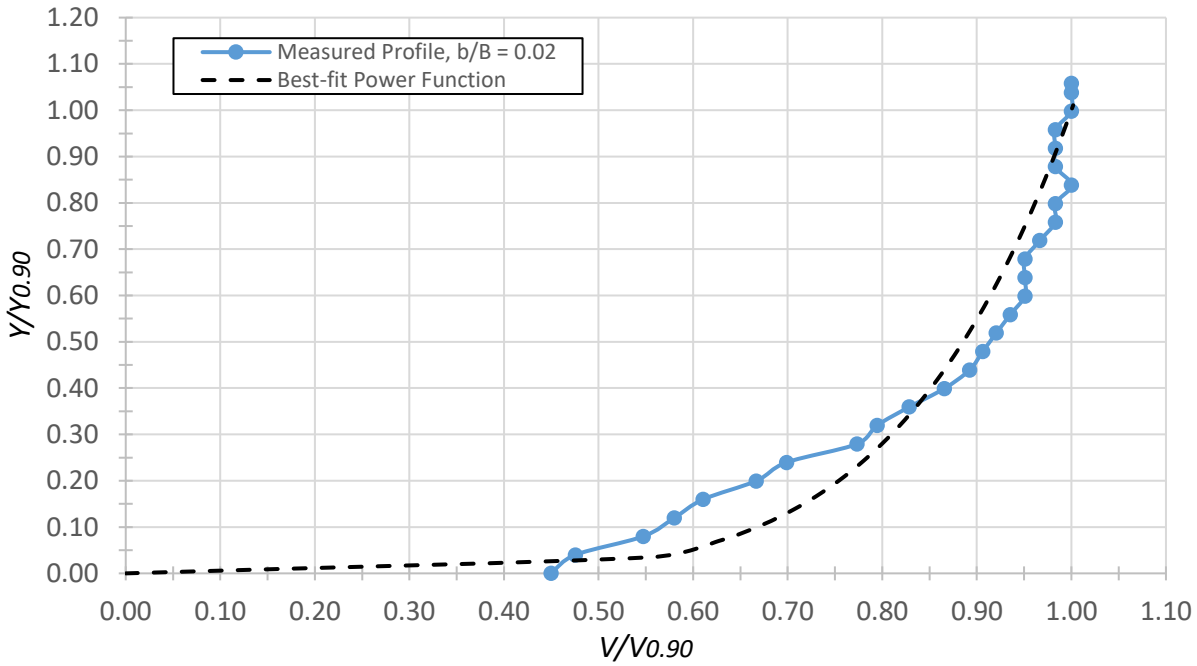

Figure 4.28. A comparison of the measured bulk-flow velocity profile and best-correlated power function for the chute position $b/B = 0.02$ when the spillway conveyed its design discharge. Exponent $N = 4.2$, $R^2 = 0.94$.

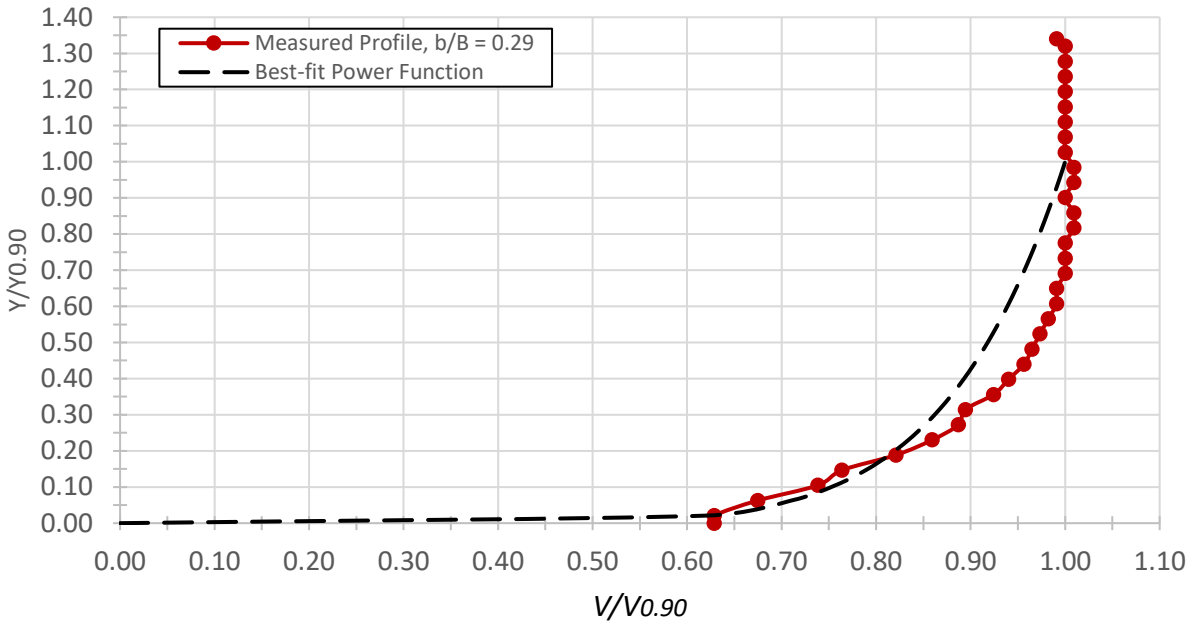

Figure 4.29. A comparison of the measured profile of bulk-flow velocity and the best-correlated power function for the chute position *b/B* = 0.29 when the chute conveyed its design discharge. Exponent $N = 8.1$, $R^2 = 0.91$.

4.5 Friction Factor

Values of the Darcy-Weisbach friction factor, *f*, were calculated at the design discharge in discrete intervals across the chute in a section of equilibrium flow. The interval spacing at which the friction factors were calculated corresponds with the chute positions as previously plotted in Sections 4.3.4 and 4.4.4, i.e. *b/B* = 0.02, then *b/B* = 0.04, and a nominal spacing of $\Delta\frac{b}{B} = 0.04$ thereafter, until *b/B* = 0.75 (beyond which measurements were precluded by the point-gage frame, as discussed in Section 3.4.1). The friction factor was calculated for each interval using the following expression:

$$\tau_o = \gamma\, Y_w\, \sin\theta = \frac{f}{8}\rho_w V^2$$

The flow was non-uniform across the chute. Hence, *V* could not be calculated as q_w/Y_w. Rather, velocity was calculated within each interval as $V_i = \left(\frac{Q}{A_i}\right) * w_i$, where w_i is a weight accounting for the discharge distribution across the curved chute, obtained for each interval by evaluating the following: $q_i = (Y_{0.90} * \bar{V})_i$, and $w_i = \frac{q_i}{\sum q}$. $\bar{V}$ is the mean (depth-averaged) velocity of the

bulk flow. For each calculation, $Y_{0.90}$ and $\bar{V}$ were taken as the average of the current and previous node values, i.e., each interval spans from *i-1* to *i*. For example, calculations at *b/B* = 0.04 comprise an average for 0.02 < *b/B* < 0.04.

Figure 4.30 plots the distribution of the calculated friction factor. The highest value, 0.1, was calculated along the chute centerline. The average value for the cross-section is $f \sim 0.07$. The distribution of friction-factor values across the chute matches the distribution of the energy grade line. The maximum value was calculated at the chute position where flow depth was maximum. Similarly, the minimum value was calculated at the position where flow depth was minimum.

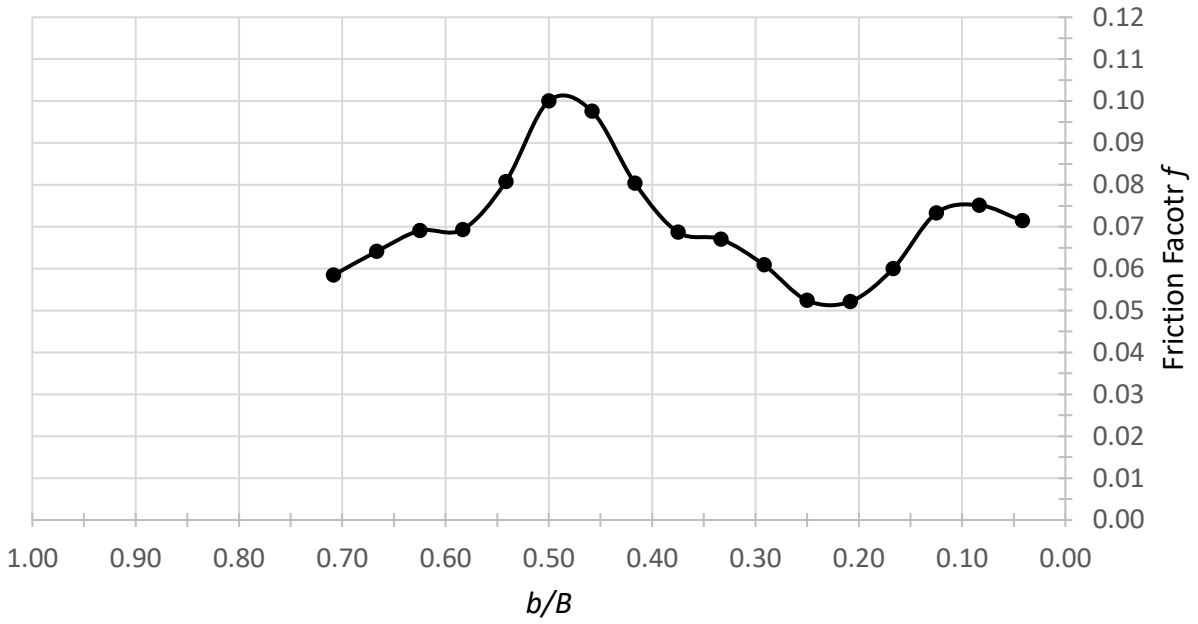

Figure 4.30. The distribution of the Darcy-Weisbach friction factor across the chute when the design discharge was conveyed.

4.6 Comparison of Results with Existing Relationships

This section compares some of the experimental results with existing relationships found within the literature (Chapter 2).

4.6.1 Vertical Distributions of Air Concentration (in Equilibrium Flow)

The vertical profile equations for air concentration by Wood (1984), Chanson & Toombes (2002), and Takahashi & Ohtsu (2012) are compared with data measured at the chute positions b/B = 0.21 and 0.50 of step 23 for the design discharge (Section 4.3.4). At these respective chute positions, $\bar{C}$ was measured as being maximum (0.608) and minimum (0.555).

The model proposed by Wood (1984) agrees remarkably well with the measured data at b/B = 0.21, and to a lesser extent (but still well) the profile at b/B = 0.50. The equation from Takahashi & Ohtsu (2012) serves as a good approximation of the measured profiles for $Y/Y_{0.90} > 0.30$, but for $Y/Y_{0.90} < 0.30$ tends to underestimate C by about 10%. Similarly, the equation by Chanson & Toombes (2002) provides a decent approximation, but underestimates C by an even larger margin than the equation by Takahashi & Ohtsu for $Y/Y_{0.90} < 0.30$.

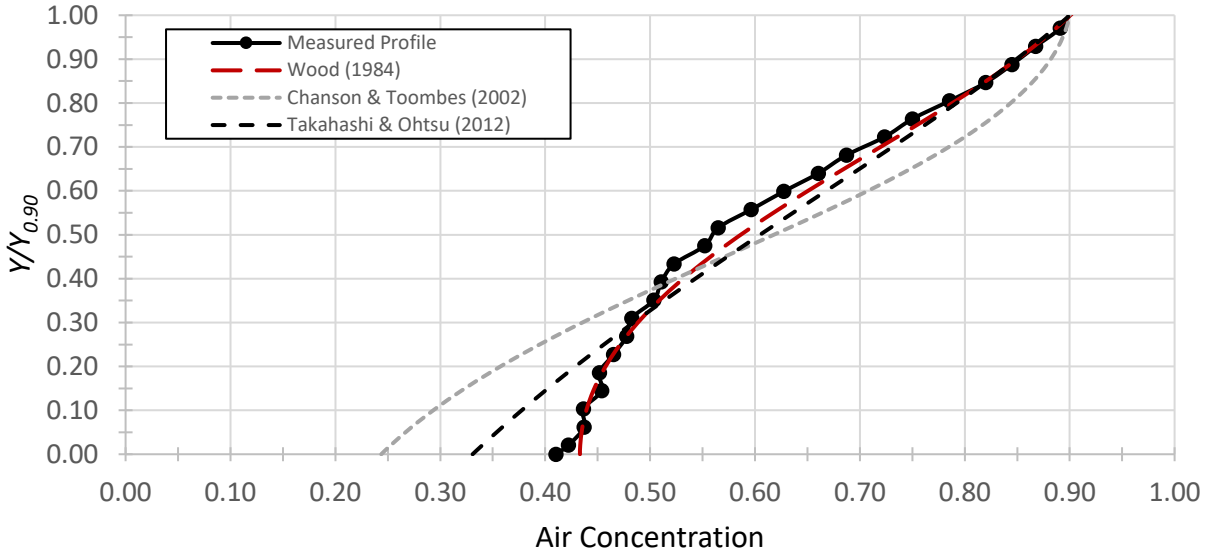

Figure 4.31. A comparison of a typical air-concentration profile measured at the chute position b/B = 0.21, where $\bar{C}$ =0.608 at the chute's design discharge, with proposed distributions by Wood (1984), Chanson & Toombes (2002) and Takahashi & Ohtsu (2012).

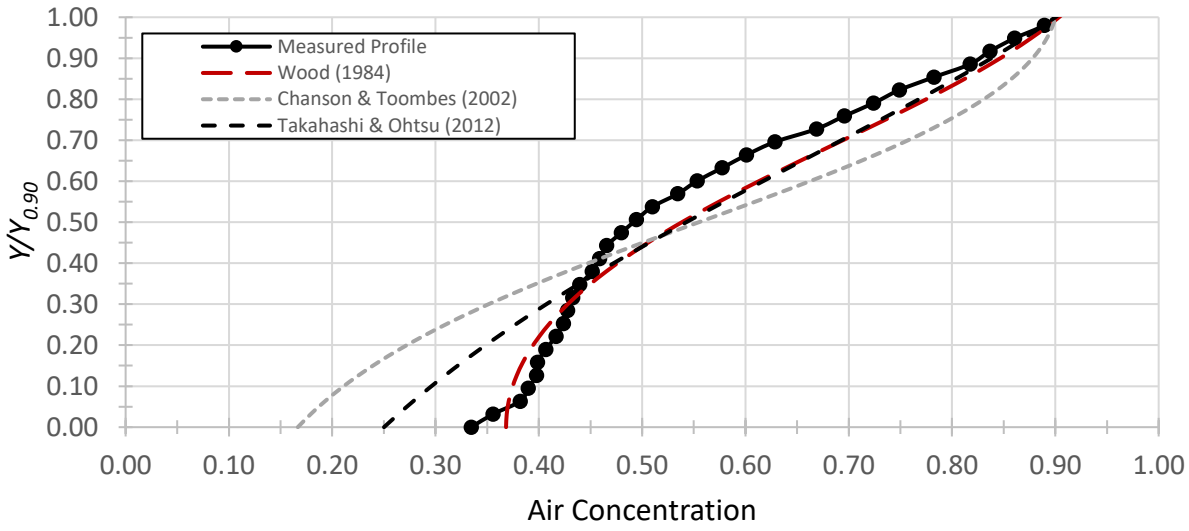

Figure 4.32. A comparison of a typical air-concentration profile measured at the chute-sidewall position, $b/B = 0.50$, where $\bar{C} = 0.555$ at the chute's design discharge, with proposed distributions by Wood (1984), Chanson & Toombes (2002) and Takahashi & Ohtsu (2012).

4.6.2 Equilibrium Flow Conditions

The unique geometry of the Gross Dam stepped spillway (its converging sidewalls, planform curvature) rendered the flow inherently non-uniform across the chute, with flow depths varying by as much as 30% (being deepest along the centerline). While the flow-depth magnitude varied across the chute, when the chute's curvature was accounted for, the lateral water surface took on a more level profile (Figure 4.16).

The condition of longitudinal flow uniformity was evaluated using two of the three established methods noted by Boes & Hager (2003b), to check for streamwise, equilibrium values. In the first case, successive air concentration profiles were compared. This was done at two chute positions: along the centerline and near the right sidewall (Figure 4.7) over a span of about 10 steps. Figure 4.8 gives additional profiles measured at greater spacing along the sidewall, between steps 87 and 23.

In these measurement sets (Figure 4.7 and Figure 4.8), longitudinally, the flow depth was more or less invariant (+/- 1.0 mm) near the end of the chute (say, by step 23), an indication of equilibrium flow conditions.

The second criterion to evaluate flow uniformity suggested by Boes & Hager is to assess the drawdown curve. This can be discerned in Figure 4.9, which plots the water-surface profile measured near the right sidewall. The results are further given in terms of $Y_{0.90}$ and $\bar{C}$ in Table 4.2. The hydraulic grade line became essentially parallel (equal) with the slope of the pseudo-bottom invert after flow bulking occurred between steps 54 and 34.

The third criterion suggested by Boes & Hager is to evaluate the friction factor for two successive cross-sections. The calculation of the friction factor includes Y_w raised to the third power. Hence, if either $Y_{0.90}$ or $\bar{C}$ (used to calculate Y_w) are discrepant between successively measured sections, the resulting values of f should be notably divergent. However, as seen in Figure 4.30, this chute's unique curvature results in significant variations in f within a single cross section, and hence this metric of assessing flow uniformity (in terms of f) is probably not well suited for a curved chute, given all the other underlying flow uncertainties.

Boes & Hager (2003b) give a relationship (Eq. (2.25) to predict H_d, the height below the spillway crest where uniform conditions should be attained. Substituting Q = 0.347 m^3/s and B = 1.87 m (for step 23), equilibrium flow conditions should be attained at H_d = 3.39 m below the spillway crest, which corresponds with about step 50. Relating this predicted value with the measured, longitudinal water-surface profile (Figure 4.9), flow bulking occurs between steps 54 and 34, and the flow depth is basically constant thereafter. By step 23 (4.78 m below the spillway crest), flow ought to be uniform (equilibrium).

As asserted by Wood (1983), Hager (1991) and others, in regions of equilibrium flow $\bar{C}$ is independent of Q (i.e. constant). However, as shown in Figure 4.33, the measured data in this study indicate that $\bar{C}$ consistently decreased as a function of Q for every tested discharge, in agreement with previous findings by, e.g., Straub & Anderson (1958) and Chamani & Rajaratnam (1999), who investigated similarly steep chutes. Not shown in the figure are comparable findings by Takahashi & Ohtsu (2014), who relate $\bar{C}$ to $S = h/Y_c$ and thereby show an effect on $\bar{C}$ from water discharge for θ=55°.

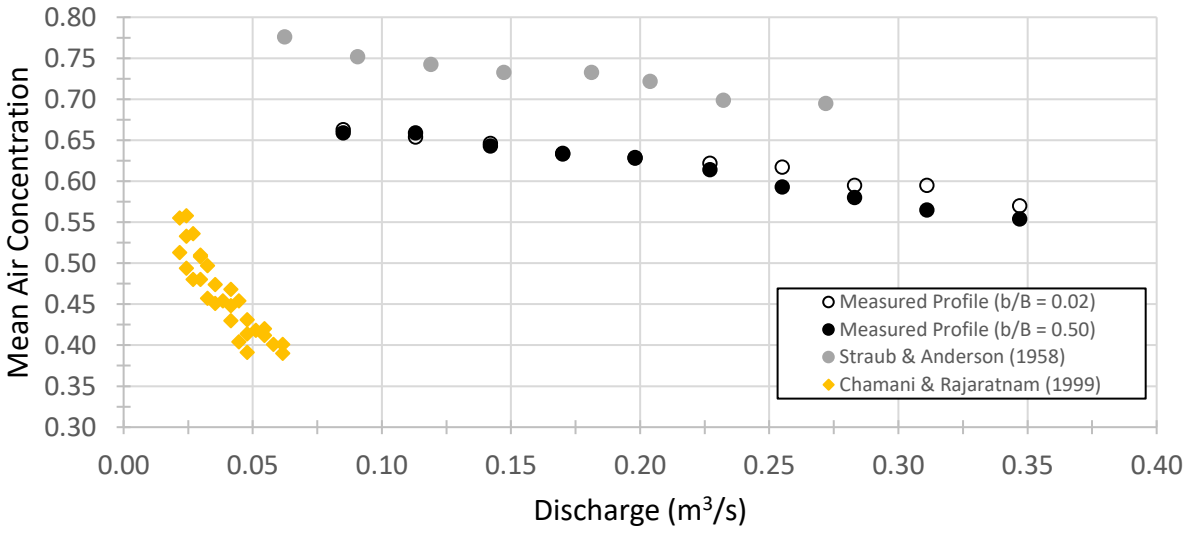

Figure 4.33. A comparison of $\bar{C}$ as a function of water discharge, with data from the present study (θ=63.4°), Straub & Anderson (θ=60.0°) and Chamani & Rajaratnam (θ=59.0°).

Applying the discharge-independent relationships for $\bar{C}_e$ to the spillway of the present study, the value predicted by Hager (1991) is 0.689, and by Christodolou (1999) is 0.805. In Figure 4.34, the measured values of $\bar{C}$ previously presented in Section 4.3.3 and 4.3.4 (collected over step 23, in different chute positions for a range of water discharges), are compared with results from Straub & Anderson and Chamani & Rajaratnam, along with the regression curves by Hager, Christodolou and Takahashi & Ohtsu[4], which show predicted values of $\bar{C}$. Of the three equations, Takahashi & Ohtsu, if extrapolated to 63.4°, appear to predict best the measured data:

[4] Because the regression equation by Takahashi & Ohtsu includes the parameter *S*, a function of critical flow depth, the curves are displayed for the minimum and maximum tested discharges (0.085 m³/s and 0.311 m³/s).

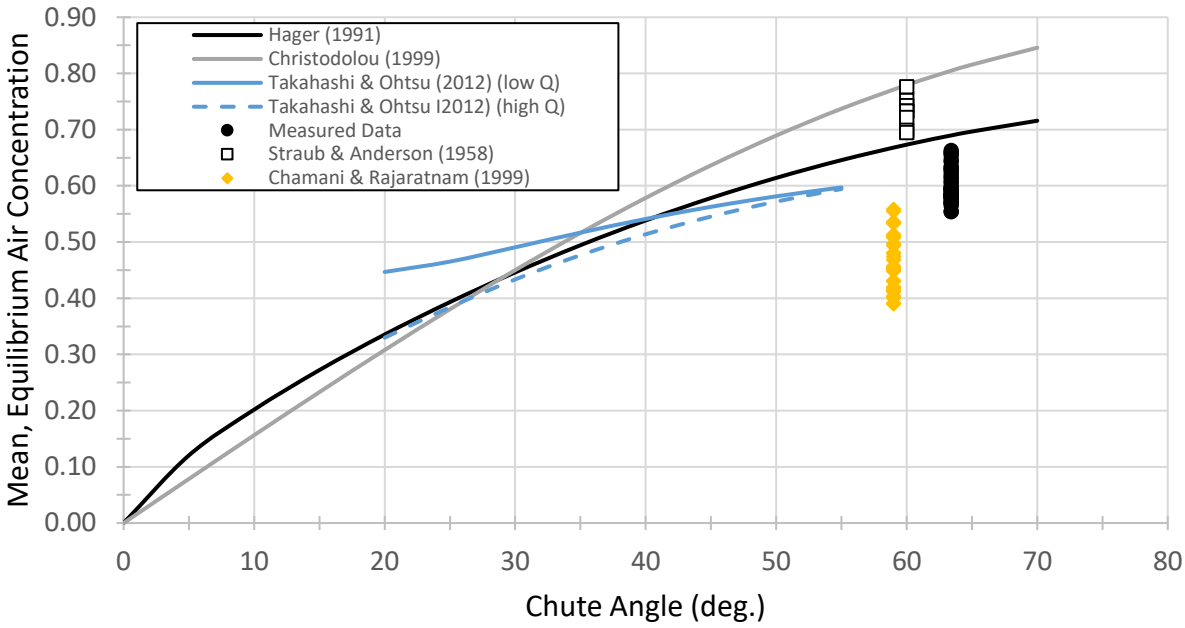

Figure 4.34. A comparison of measured values of $\bar{C}$ with predicted values of $\bar{C}$, as functions of the chute slope. The data shown are from the present study (θ=63.4°), Straub & Anderson (θ=60.0°) and Chamani & Rajaratnam (θ=59.0°); compared with existing relationships by Hager (1991), Christodolou (1999) and Takahashi & Ohtsu (2012).

4.6.3 Velocity Exponent

Similar to the findings of other researchers, the velocity results from Section 4.4 indicate considerable scatter in the exponent *N* of the normalized profile of bulk-flow velocity, represented by a power-law function [$V/V_{0.90} = (Y/Y_{0.90})^{1/N}$]. In this study, that scatter owed largely to the wide range of tested flow conditions (0.085 m^3/s < Q < 0.311 m^3/s), as well as the range of flow depths for a single discharge, an effect of the chute's curvature.

For velocity profiles measured at the sidewall position (*b/B* = 0.02) of step 23, the exponent *N* varied by almost a factor of 2, as Table 4.10 indicates: the highest value of *N* was 8.0 for the lowest tested water discharge, and the lowest value of *N* was 4.3 for the highest tested water discharge. A similar trend, where *N* is a negatively decreasing function of *Q*, was observed along the chute centerline, with results of *N* given in Table 4.11.

The regression equation formulated by Takahashi & Ohtsu (2012) is compared with the measured values reported in Table 4.10 and Table 4.11, concerning a range of water discharges over step 23. The equation has bounds of θ<55°, however the extrapolated values of N for θ=63.4° seem reasonable considering the overall trend of the regression equation, which comports with the findings by Boes & Hager (2003a) that N increases for flatter slopes, and hence, in line with the regression's trend, N should decrease for flatter slopes. The extrapolated value of N at θ=63.4° is slightly less than the value suggested for θ=55°. Yet, as the comparison in Figure 4.35 shows, values of N which were calculated from profiles of the bulk-flow velocity measured in the present work are much higher than suggested by Takahashi & Ohtsu (2012).

Figure 4.35 also shows that measured values of N have a greater response to water discharge than the regression equation implies: the curve flatlines with increasing Q, whereas the measured data align generally with slopes ($\Delta N/\Delta Q$) of -11.7 s/m^3 at b/B = 0.02, and -8.7 s/m^3 at b/B = 0.50.

To note, near the sidewall (b/B = 0.02) the effect of the sidewall boundary layer has been reported in the literature to alter the velocity profile, e.g. Kramer (2004), who found that bulk-flow velocities were reduced in the vicinity of the sidewall by as much as 10%. Hence, the discrepancies between values of N at the two chute positions are not so significant as the general trends displayed, as well as the relative magnitude differences between the measured data and the values predicted by Takahashi & Ohtsu.

In Figure 4.36, the flat-line value of N recommended by Takahashi & Ohtsu in Figure 4.35 is plotted with the data measured along the chute-centerline position for a range of water discharges.

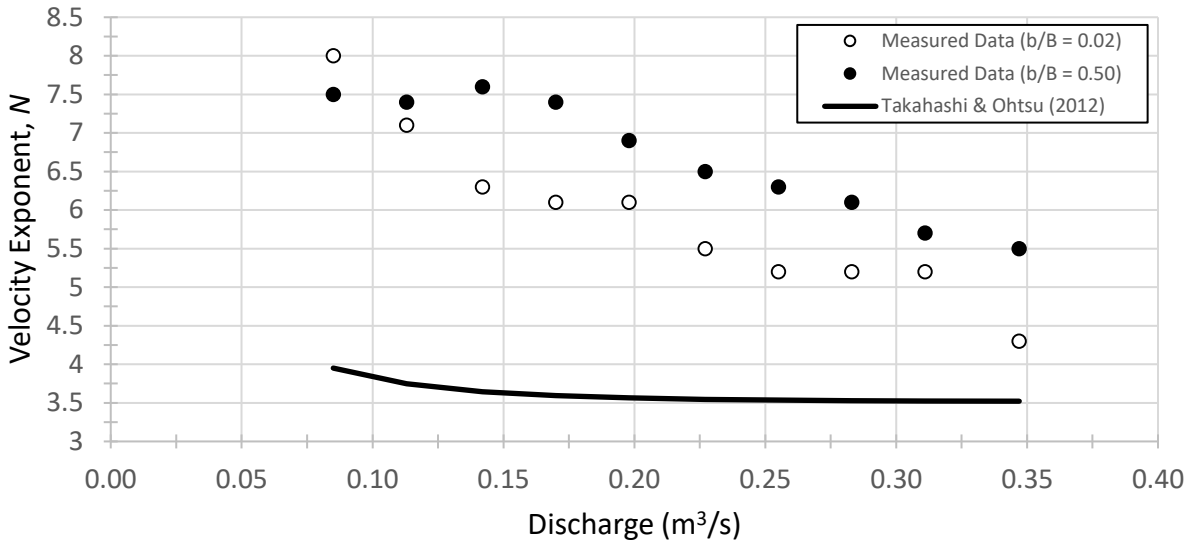

Figure 4.35. A comparison of the values of *N* calculated for a range of water discharges measured at two chute positions across 23, with empirical relationship from Takahashi & Ohtsu (2012).

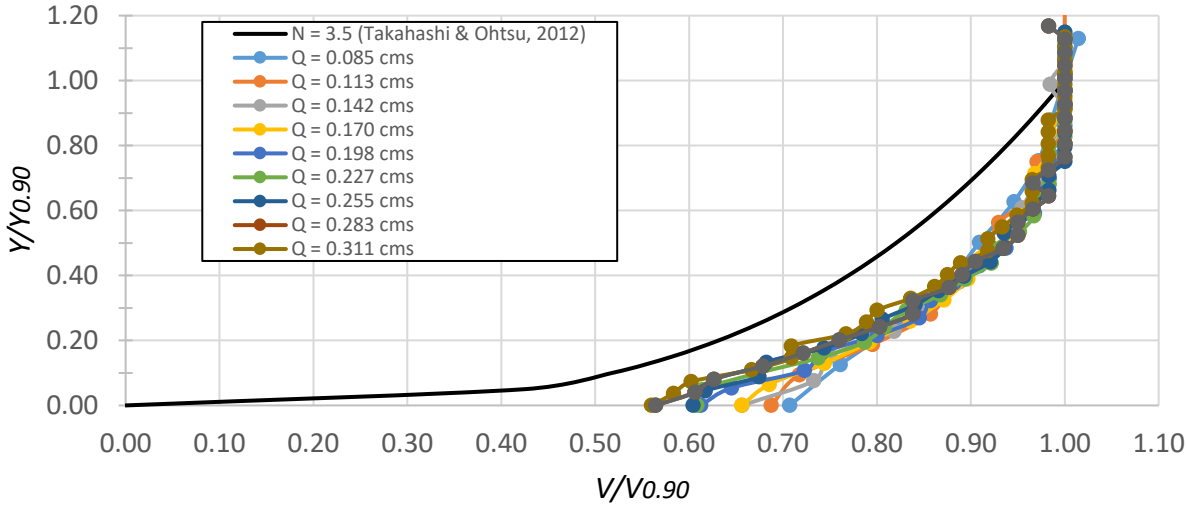

Figure 4.36. A comparison of the measured bulk-flow velocity profiles collected at the chute-centerline position of step 23 for a range of water discharges, with the predicted profile exponent *N* = 3.5 from Takahashi & Ohtsu (2012).

4.6.4 Friction Factor

Using Eq. (2.8 by Takahashi & Ohtsu (extrapolated slightly beyond 55°), for the design discharge at step 23, $f = 0.063$. Figure 4.37 compares that estimated value (in the legend, marked *R* for regression) with results obtained in the present work. Also compared are values of f calculated using Eq. (2.6 from the same authors (*E*), which involves the ratio of clear-water flow depth to critical flow depth raised to the third power. Finally, the equation by Chamani & Rajaratnam (1999), Eq. (2.7, is plotted, wherein flow depth is taken as the $Y_{0.90}$ value. The measured data were calculated from Eq. (2.5 at width increments of 0.04, thereby accounting for the distributions of flow depth and velocity across the chute.

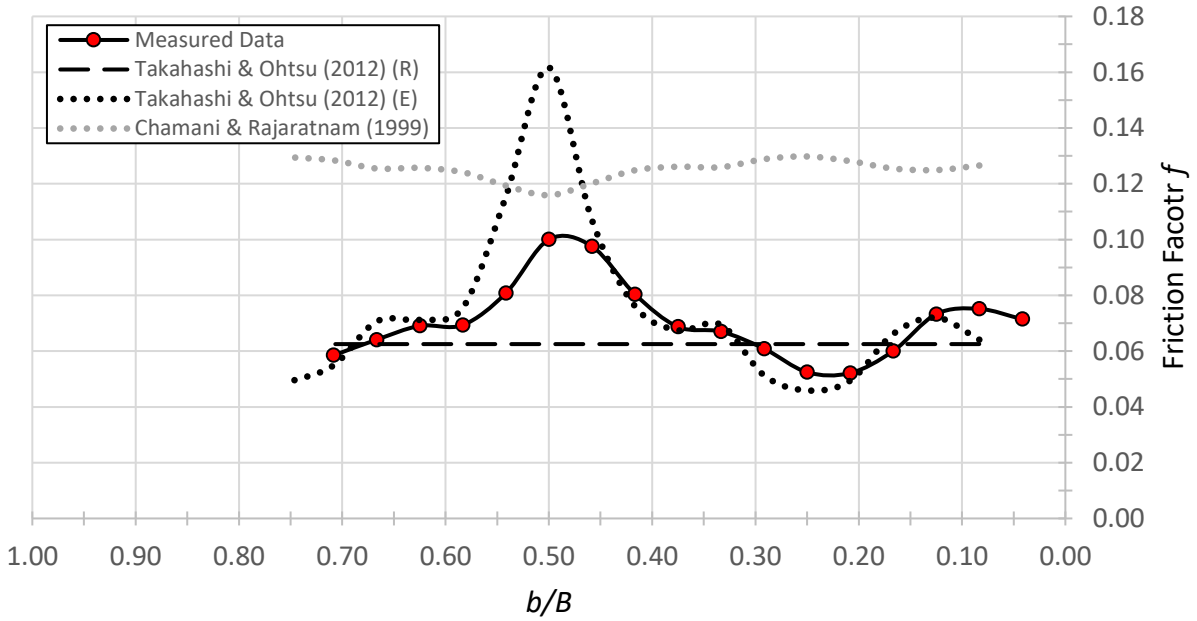

Figure 4.37. A comparison of the calculated values of f from the profile data measured across step 23 when the chute conveyed its design discharge, with predicted value by Takahashi & Ohtsu (2012) and Chamani & Rajaratnam (1999).

An order-of-magnitude approximation for f in the present chute (θ=63.4°) at the chute's design flow, is 0.1. That value falls on the lower end of the probability distribution function generated by Chanson (2006) of friction-factor values obtained in large-scale, experimental models of steep stepped chutes. A practical or design consequence of this finding regarding the lower than

expected value of f is that greater reliance must be placed on the stilling basin at the bottom of the chute than the literature on stepped spillways has led designers to understand. This finding reinforces essentially the same finding reported by Pegram et al. (1999) for steep stepped spillways.

4.6.5 Time Series

Bung (2013) used a conductivity probe as well as a high-speed video camera to examine surface wave characteristics in a region of uniform, skimming flow. From his analyses, Bung calculated wave frequencies of the water surface and found a wide range of values for small Y_c/h, which he attributes to high degrees of turbulence. He notes that to perform such an analysis (on wave frequencies), a high sample rate, especially of video footage but also of phase detection, is required.

The data pertaining to roll waves (presented in Section 4.3.6.2) were used to undertake a similar wave frequency analysis to Bung's, and to assess the effect on air concentration of the roll waves. However, the flow regime associated with roll waves (generally, in the case of the present chute, that meant very low water discharges) was markedly different from the skimming regime that occurred for high water discharges. When roll waves were present along the chute, as noted in the relevant section, the low bubble detection rate by the conductivity probe (# bubbles / sec) associated with the shallow flow depth of the roll wave regime hindered a substantive analysis of the air concentration variation with time.

The moving-average function presented in that section, if used to analyze data collected by a conductivity probe in time-coordinated conjunction with a high-speed video camera, could lend more precise vision to the fluctuations of C associated with passing roll waves. With the frequency determined by the video camera used to inform the value of T_w (from Section 0, the time-averaging window over which air concentration is averaged), a robust analysis could be undertaken.

4.6.6 Pier Effect

The experimental study by Calitz (2015) featured a stepped spillway equipped with one pier, placed downstream the ogee crest and atop the transitional sub reach of steps (step of increasing

dimension). In his study, the flow separation that occurred because of the downstream placement of the piers resulted in a different effect on air entrainment from what was observed in the physical model of the present work. Figure 4.38 shows, on left, the pier configuration used by Calitz, and on right, an iso-contour of air concentration showing an unaerated flow region downstream the piers. Incipient aeration occurred in the hydraulic model used by Calitz near the end of the chute, with $\bar{C}$ reaching only about 20%. The two piers along the crest of the Gross Dam spillway model caused substantial air entrainment, and flow downstream the piers was thoroughly aerated, as photos in Appendix A show.

(a)

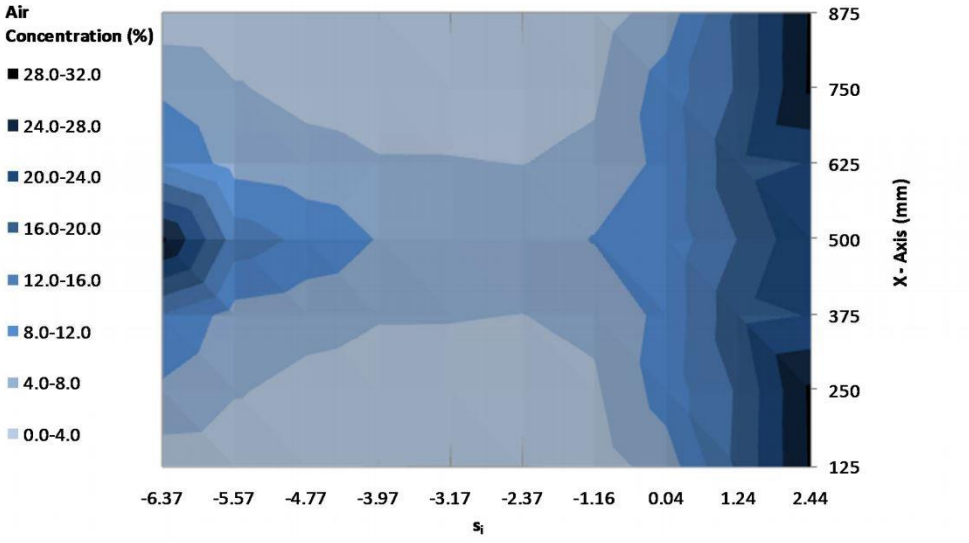

(b)

Figure 4.38. Flow separation around a pier by Calitz (2015). In (a), a photograph of the flow separation, and in (b), an iso-contour plot of depth-averaged values of air concentration taken along the chute.

5 CONCLUSIONS & RECOMMENDATIONS

The hydraulic model of Gross Dam spillway created a unique opportunity to investigate air entrainment and transport in a spillway chute of comparatively unique geometry. The geometry was unique because of the chute's height and steepness, converging sidewalls, and curved planform. While the feature of converging sidewalls had been somewhat explored during a few earlier experiments, most earlier experiments on air entrainment involved rectangular chutes of constant cross section.

The measurements obtained from the hydraulic model of Gross Dam spillway indicate a number of key findings related to the chute's geometry. Near the converging sidewalls, flow was found to be affected both in terms of depth and velocity. The chute's planform curvature resulted in distinct flow distributions across the chute of air concentration and flow depth. The steepness of the chute contributed to vertical mixing over the measured profiles of both air concentration and bulk-flow velocity. Also, the presence of the two piers along the spillway crest influenced the spillway's air-entrainment performance.

5.1 Main Conclusions

The main conclusions from the present study address the study's objectives and were as follow:

1. The skimming condition of flow prevailed along the spillway chute for a model-scale $Q \geq 0.028$ m^3/s, (i.e., for all discharges greater than about 9% the design discharge for the spillway);
2. The presence of the two piers along the spillway crest and the crest sidewalls affected the plan profile of the "line" of incipient aeration, especially at high water discharges (e.g., the chute's design discharge). Figure 4.6 shows the profile for that discharge. The wakes formed by the piers, and the sidewalls triggered aeration nearer to the crest than otherwise occurred at chute positions between the piers;
3. The chute's converging sidewalls (convergence angle of 2.2^o) mildly affected the flow near the sidewalls, causing slight increases in flow depth and reductions in flow velocity. These changes, though noticeable, were negligible in terms of spillway performance because of their magnitude;

4. The chute's planform curvature caused flow depths to vary across the chute. The measured flow depths ($Y_{0.90}$) varied as much as 30% across the chute when the design discharge was conveyed. The flow was deepest along the centerline ($Y_{0.90}$ = 0.096 m) and shallowest about half-way between each sidewall and the centerline ($Y_{0.90}$ = 0.071 m). The slightly larger depth near the sidewalls was caused by the convergence of the sidewalls. When accounting for the chute's curvature, the level of the water surface at the centerline of the chute was approximately the same as near the sidewall;
5. At the design discharge, where $Y_{0.90}$ was maximum across step 23 (along the centerline of the chute), the depth-averaged value of air concentration, $\bar{C}$ was least (0.554). Conversely, where flow depth was minimum across step 23, $\bar{C}$ was greatest (0.608);
6. At the design discharge, depth-averaged values of the bulk-flow velocity, $\bar{V}$, showed little variation across the chute at step 23, except near the sidewall, where $\bar{V}$ (5.06 m/s) was about 10% less, on average, than the values measured at positions across the chute (5.41 m/s < $\bar{V}$ < 5.84 m/s);
7. At the design discharge, the Darcy-Weisbach friction factor, *f*, varied across the chute. The variation matched the energy grade line. The maximum value of *f* was calculated along the centerline as being 0.10. The minimum value of *f* occurred where flow depth was minimum and was about 0.05; and,
8. Near the end of the chute (at step 23), values of $\bar{C}$ decreased with increasing water discharge. Here, near the sidewall, $\bar{C}$ reached a maximum value of 0.663 for the lowest water discharge, and a minimum value of 0.570 for the highest water discharge. Similarly, at this elevation, and at the chute's centerline position, those values were 0.659 and 0.554.

The conductivity probe functioned well and produced replicable measurements of air concentration and bulk-flow velocity for a wide range of flow conditions within the chute. Though, when the chute conveyed the low water discharge associated with roll waves, submergence of the probe tips was restricted to just one major division along the point-gage assembly. Thus, point-wise data of the roll waves could not be assembled into profiles, as was done for the high water discharges associated with the skimming flow regime.

5.2 Recommendations for Further Research

While this study briefly investigated the phenomenon of roll waves using the conductivity probe to generate time-series records of the air concentration, the shallow flow depth associated with the roll-wave discharge precluded pointwise data from being assembled into profiles. Also, the low bubble frequency associated with that low water discharge, made dubious the results obtained by time-averaging the data over short durations (e.g., if averaged over $T_w < 1.0$ sec, a similar duration as the frequency associated with roll-wave passage). In future studies, analyses of roll waves in terms of the temporal fluctuations of air concentration may be facilitated using a high-speed video camera, to correlate the observed roll-wave frequency with the values of air concentration measured by the conductivity probe. A tandem evaluation of the video-camera footage, employing the technique of bubble image velocimetry (BIV) may also prove useful, as previously undertaken in the literature (e.g., Bung, 2014).

The effect of the chute's converging sidewalls should be assessed for degrees of convergence greater than that of the new spillway designed for Gross Dam (2.2^o). Specifically, for a chute of comparable slope to Gross Dam, variable convergence angles should be evaluated for their effect on the values of air concentration measured near the chute sidewalls. Such an evaluation of sidewall convergence on chute flow would require additional measurements collected at transects higher up along the chute, which could be facilitated by an automated cart and traverse system to more easily access those hard-to-reach chute positions.

Near the bottom of the chute, water discharge was found to affect the measured values of depth-averaged air concentration, both along the chute's centerline and near the sidewall. This finding affirms what has been previously reported in the literature by other researchers who investigated similarly steep chutes (e.g., Straub & Anderson, 1958; Chamani & Rajaratnam, 1999; Ohtsu, Yasuda & Takahashi, 2004; Takahashi & Ohtsu, 2012). In that transect, depth-averaged values of air concentration were also found to vary across the chute (a consequence of the chute's curvature), and the values correlated with flow depth. This finding indicates that chute curvature affects the process of air entrainment and the equilibrium values attained, for a given chute slope. Further research should be conducted to evaluate this effect in chutes with larger planform radii of curvature.

Evaluation of the inception point of air entrainment and an exact delineation of its curved perimeter should be undertaken by applying the definition of inception by Boes & Hager (2003b); i.e., where the pseudo-bottom air concentration equals 0.01. Because the onset of aeration occurred at or above step 87 (4.4 m above the invert of the stilling basin), access to the locations of interest was impractical for this study. However, with the use of an automated cart and traverse system, a more exact evaluation could be undertaken of the profile of incipient aeration. An iso-contour plot of air concentration comparable to the plot generated by Calitz (2015) could also provide useful clarity to understanding the degree of aeration in the vicinity of the piers.

6 REFERENCES

André, S., & Schleiss, A. (2004). High velocity aerated flows on stepped chutes with macro-roughness elements (No. BOOK). EPFL-LCH.

Boes, R. M., & Hager, W. H. (2003a). Two-phase flow characteristics of stepped spillways. *Journal of Hydraulic Engineering*, 129(9), 661-670.

Boes, R. M., & Hager, W. H. (2003b). Hydraulic design of stepped spillways. *Journal of Hydraulic Engineering*, 129(9), 671-679.

Boes, R. M., Chanson, H., Matos, J., Ohtsu, I., Yasuda, Y., Takahasi, M., Chamani & Rajaratnam, N. (2000). Characteristics of skimming flow over stepped spillways. *Journal of Hydraulic Engineering*, 126(11), 860-873.

Boes, R. M. (2000). Scale effects in modelling two-phase stepped spillway flow. *In International Workshop on Hydraulics of Stepped Spillways*, 53-60.

Bung, D. B. (2013). Non-intrusive detection of air–water surface roughness in self-aerated chute flows. *Journal of Hydraulic Research*, 51(3), 322-329.

Bung, D. B., Leandro, J., & Carvalho, R. (2014). Measuring void fraction and velocity fields of a stepped spillway for skimming flow using non-intrusive methods. *Experiments in Fluids*, 55(5), 1732.

Cain, P. (1978). Measurements within self-aerated flow on a large spillway. Research Report 78-18, Ph. D Thesis, Department of Civil Engineering, University of Canterbury, Christchurch, New Zealand.

Calitz, J. A. (2015). Investigation of air concentration and pressures of a stepped spillway equipped with a crest pier. Doctoral dissertation, Stellenbosch University.

Chamani, M. R., & Rajaratnam, N. (1999). Characteristics of skimming flow over stepped spillways. *Journal of Hydraulic Engineering*, 125(4), 361-368.

Chanson, H. (1993). Self-aerated flows on chutes and spillways. *Journal of Hydraulic Engineering*, 119(2), 220-243.

Chanson, H. (1994). Hydraulic design of stepped cascades, channels, weirs and spillways. Pergamon.

Chanson, H. (1995). Air bubble diffusion in supercritical open channel flow. *Proc. 12th Australasian Fluid Mechanics Conference*, Sydney, Australia, 707-710.

Chanson, H. (2001). Hydraulic design of stepped spillways and downstream energy dissipators. *Dam Engineering*, 11(4), 205-242.

Chanson, H. (2006). Hydraulics of skimming flows on stepped chutes: The effects of inflow conditions? *Journal of Hydraulic Research*, 44(1), 51-60.

Chanson, H., & Toombes, L. (2002). Experimental investigations of air entrainment in transition and skimming flows down a stepped chute. *Canadian Journal of Civil Engineering*, 29(1), 145-156.

Ettema, R., Thornton, C., Hogan, T., & Biethman, B. (2019). Gross Dam Reservoir Expansion: Hydraulic Model Study of Stepped Spillway Design CSU-HYD Report No. 2019-2, Colorado State University, Fort Collins, CO, 1-105.

Felder, S., & Chanson, H. (2015). Phase-detection probe measurements in high-velocity free-surface flows including a discussion of key sampling parameters. *Experimental Thermal and Fluid Science*, 61, 66–78.

Frizell, K. H. & Ruff, J. F. (1994). Air concentration measurements in highly-turbulent flow on a steeply-sloping chute. *Proceedings of the 1994 ASCE National Conference on Hydraulic Engineering*, 999–1003.

Frizell, K. H., Ehler, D. G., & Mefford, B. W. (1994). Developing air concentration and velocity probes for measuring highly-aerated, high-velocity flow. *ASCE Symposium on Hydraulic Measurements and Experimentation*, 1–10.

Frizell, K. W., & Frizell, K. H. (2015). Guidelines for hydraulic design of stepped spillways. *Hydraulic Laboratory Report HL-2015-06*.

Geringer, J.J., & Officer A.K. (1995). Stepped spillway hydraulic research for RCC dams – Quo vadis? *Preprints of the Int. Symposium on RCC Dams*, Santander, Spain, 549-563.

Hager, W. H. (1991). Uniform aerated chute flow. *Journal of Hydraulic Engineering*, 117(4), 528-533.

Hunt, S. L., Kadavy, K. C., Abt, S. R., & Temple, D. M. (2008). Impact of converging chute walls for roller compacted concrete stepped spillways. *Journal of Hydraulic Engineering*, 134(7), 1000-1003.

Matos, J. (2000). Hydraulic design of stepped spillways over RCC dams. *Intl. Workshop on Hydraulics of Stepped Spillways*, 187-194.

Matos, J., & Meireles, I. (2014). Hydraulics of stepped weirs and dam spillways: Engineering challenges, labyrinths of research. *11th National Conference on Hydraulics in Civil Engineering & 5th International Symposium on Hydraulic Structures: Hydraulic Structures and Society-Engineering Challenges and Extremes*, 26-33.

Meireles, I., Matos, J., & Frizell, K. (2007). Measuring air entrainment and flow bulking in skimming flow over steeply sloping stepped chutes.

Ohtsu, I., & Yasuda, Y. 1997. Characteristics of flow conditions on stepped channels. *Proc., 27th IAHR Congress*, *San Francisco*, 583– 588.

Ohtsu, I., Yasuda, Y., & Takahashi, M. (2004). Flow characteristics of skimming flows in stepped channels. *Journal of Hydraulic Engineering*, 130(9), 860-869.

Pegram, G. G., Officer, A. K. & Mottram, S. R. (1999). Hydraulics of skimming flow on modeled stepped spillways. *Journal of Hydraulic Engineering, American Society of Civil Engineers*, Vol. 125(5), 500-510.

Pfister, M. & Chanson, H. (2014). Two-phase air-water flows: Scale effects in physical modeling. *Journal of Hydrodynamics*, Vol. 26, No. 2, pp. 291-298.

Pinto, N. L. de S., Neidert, S. H. (1982). Model prototype conformity in aerated spillway flow. *International Conference on Hydraulic Modeling of Civil Engineering Structures*, BHRA, Paper E6, 1982, pp. 273-284.

Rajaratnam, N. (1990). Skimming flow in stepped spillways. *Journal of Hydraulic Engineering*, 116(4), 587-591.

Schwarzkopf, J. D., Sommerfeld, M., Crowe, C. T., & Tsuji, Y. (2011). *Multiphase flows with droplets and particles*. CRC press.

Straub, L. G., & Anderson, A. G. (1958). Experiments on self-aerated flow in open channels. *Journal of the Hydraulics Division*, 84(7), 1-35.

Takahashi, M., & Ohtsu, I. (2012). Aerated flow characteristics of skimming flow over stepped chutes. *Journal of Hydraulic Research*, 50(4), 427-434.

Van Staden, H. P. (1991). *Wolwedans Dam Spillway Model Study*. Report No. K200/02/DH01, Republic of South Africa Department of Water Affairs & Forestry

Wood, I. R. (1983). Uniform region of self-aerated flow. *Journal of Hydraulic Engineering*, 109(3), 447-461.

Wood, I. R. (1984). "Air entrainment in high speed flows." Proc., Syrup. on Scale Effects in modelling Hydraulic Structures, IAHR, Esslingen, Germany, paper 4.1.

Wood, I.R. (1991). Air entrainment in free-surface flows. IAHR Hydraulic Structures Design Manual 4. Balkema, Rotterdam.

Appendix A FLOW CONDITION PHOTOS

A.1 0.014 $m^3/s < Q < 0.028$ m^3/s

Figure A.1. A photograph of the spillway chute conveying a water discharge in the range of 0.014 $m^3/s < Q < 0.028$ m^3/s.

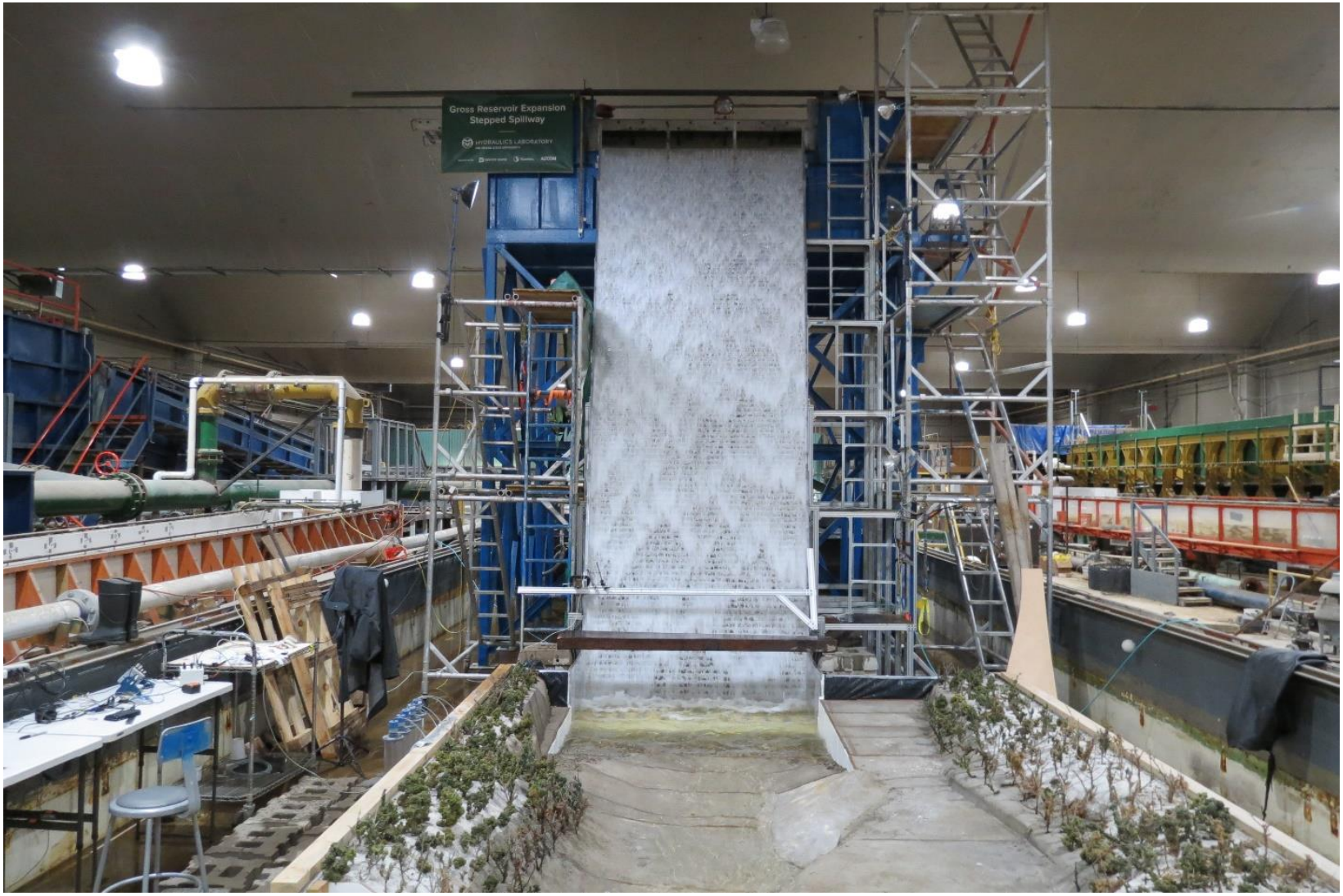

Figure A.2. A photograph of the spillway chute conveying a water discharge in the range of 0.014 $m^3/s < Q < 0.028$ m^3/s.

Figure A.3. A photograph of the spillway chute conveying a water discharge in the range of 0.014 $m^3/s < Q < 0.028$ m^3/s.

A.2 $Q = 0.028$ m^3/s

Figure A.4. A photograph of the spillway chute conveying a water discharge of $Q = 0.028$ m^3/s.

Figure A.5. A photograph of the spillway chute conveying a water discharge of $Q = 0.028$ m^3/s.

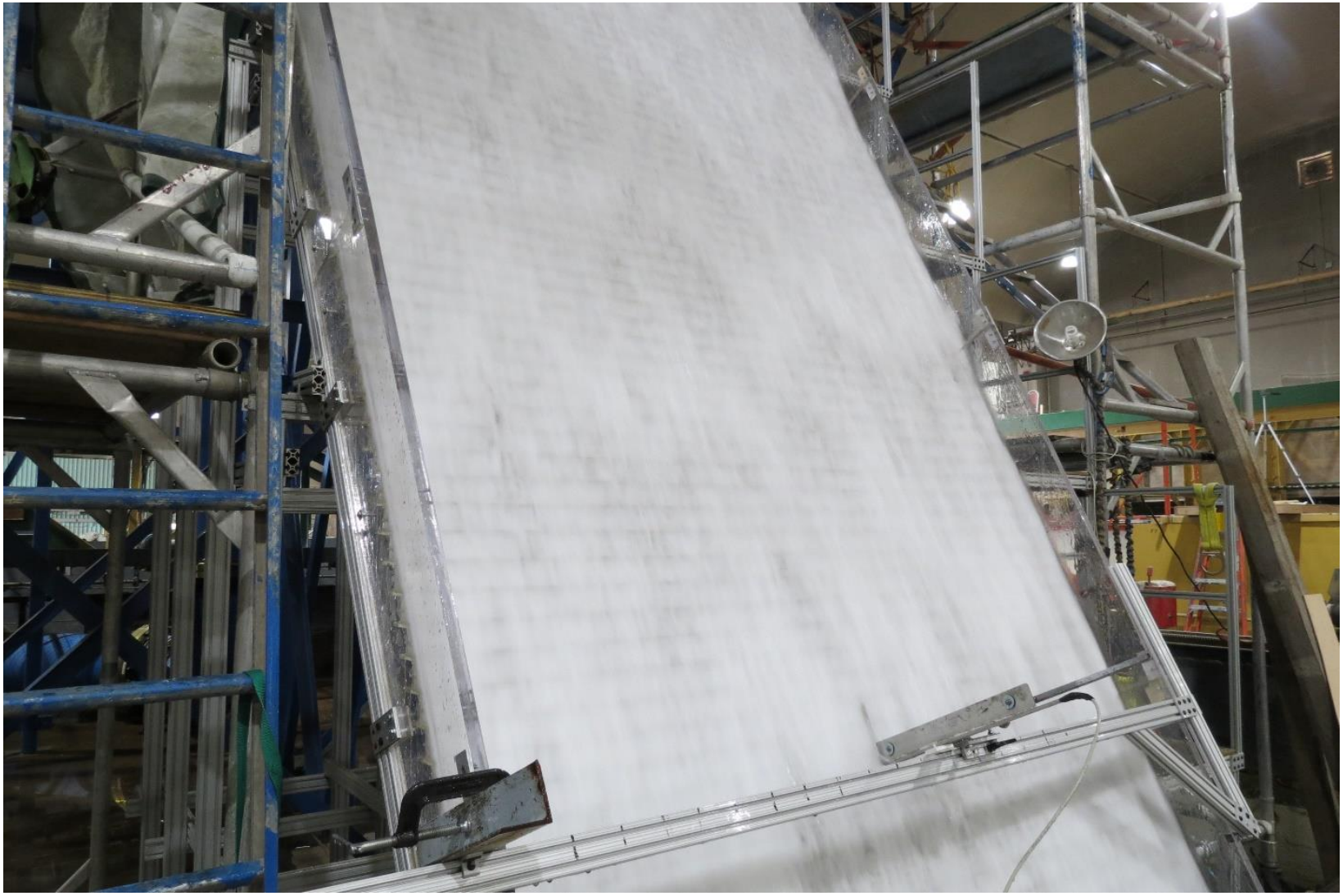

Figure A.6. A photograph of the spillway chute conveying a water discharge of $Q = 0.028$ m^3/s.

Figure A.7. A photograph of the spillway chute conveying a water discharge of $Q = 0.028$ m^3/s.

Figure A.8. A photograph of the spillway chute conveying a water discharge of $Q = 0.028$ m^3/s.

Figure A.9. A photograph of the spillway chute conveying a water discharge of $Q = 0.028$ m^3/s.

Figure A.10. A photograph of the spillway chute conveying a water discharge of $Q = 0.028$ m^3/s.

A.3 $Q = 0.085$ m^3/s

Figure A.11. A photograph of the spillway chute conveying a water discharge of $Q = 0.085$ m^3/s.

Figure A.12. A photograph of the spillway chute conveying a water discharge of $Q = 0.085$ m^3/s.

A.4 Q = 0.133 m^3/s

Figure A.13. A photograph of the spillway chute conveying a water discharge of Q = 0.085 m^3/s.

Figure A.14. A photograph of the spillway chute conveying a water discharge of $Q = 0.085$ m^3/s.

A.5 $Q = 0.142$ m^3/s

Figure A.15. A photograph of the spillway chute conveying a water discharge of $Q = 0.085$ m^3/s.

Figure A.16. A photograph of the spillway chute conveying a water discharge of $Q = 0.085$ m^3/s.

A.6 $Q = 0.170$ m^3/s

Figure A.17. A photograph of the spillway chute conveying a water discharge of $Q = 0.170$ m^3/s.

Figure A.18. A photograph of the spillway chute conveying a water discharge of $Q = 0.170$ m^3/s.

A.7 $Q = 0.198$ m^3/s

Figure A.19. A photograph of the spillway chute conveying a water discharge of $Q = 0.170$ m^3/s.

Figure A.20. A photograph of the spillway chute conveying a water discharge of $Q = 0.170$ m^3/s.

A.8 $Q = 0.227$ m^3/s

Figure A.21. A photograph of the spillway chute conveying a water discharge of $Q = 0.227$ m^3/s.

Figure A.22. A photograph of the spillway chute conveying a water discharge of $Q = 0.227$ m^3/s.

A.9 $Q = 0.255$ m^3/s

Figure A.23. A photograph of the spillway chute conveying a water discharge of $Q = 0.255$ m^3/s.

Figure A.24. A photograph of the spillway chute conveying a water discharge of $Q = 0.255$ m^3/s.

A.10 $Q = 0.283$ m^3/s

Figure A.25. A photograph of the spillway chute conveying a water discharge of $Q = 0.283$ m^3/s.

Figure A.26. A photograph of the spillway chute conveying a water discharge of $Q = 0.283$ m^3/s.

A.11 $Q = 0.311$ m^3/s

Figure A.27. A photograph of the spillway chute conveying a water discharge of $Q = 0.311$ m^3/s.

Figure A.28. A photograph of the spillway chute conveying a water discharge of $Q = 0.311$ m^3/s.

A.12 Q = 0.347 m^3/s (the design discharge)

Figure A.29. A photograph of the spillway chute conveying a water discharge of Q = 0.347 m^3/s.

Figure A.30. A photograph of the spillway chute conveying a water discharge of Q = 0.347 m^3/s, with the conductivity probe elevated to the definitional water surface ($Y_{0.90}$).

Figure A.31. A photograph of the spillway chute conveying a water discharge of $Q = 0.347$ m^3/s, with the conductivity probe elevated to the definitional water surface ($Y_{0.90}$).

Figure A.32. A photograph of the spillway chute conveying a water discharge of $Q = 0.347$ m^3/s, with a view of the profile of incipient flow aeration.

Figure A.33. A photograph of the spillway chute conveying a water discharge of $Q = 0.347$ m^3/s, near the point of incipient sidewall-flow aeration.

Figure A.34. A photograph of the spillway chute conveying a water discharge of $Q = 0.347$ m^3/s, near the point of incipient sidewall-flow aeration.

Appendix B FLOW REGIMES IN STEPPED CHUTES

Two general flow regimes occur in stepped spillways – nappe flow, and skimming flow. Typically, nappe flow corresponds with lower water discharges and/or flatter spillway slopes, while the skimming mode prevails for the reverse conditions. At intermediate discharges, a so-called transition flow has been documented in some chutes, fleetingly (e.g., Ohtsu & Yasuda, 1997). For most stepped spillways that are designed to convey high-head flows, the skimming regime is desired because it results in the highest amount of flow aeration, thereby mitigating the risk of cavitation damage to the structure; according to Peterka (1958), if the air concentration along the chute-bottom is about 5%, then cavitation concerns are negligible.

Empirically, the flow regime of a stepped spillway can be inferred by two parameters: the chute slope, h/l (where h and l are the step riser and tread dimensions, respectively); and Y_c/h, a measure of the water discharge (expressed as critical flow depth) relative to h. A plot showing empirical data pertaining to the flow regimes is given in Figure 2.1. In the following sections, the general flow behavior of each mode is described.

B.1 Skimming Flow

The skimming flow regime is characterized by high degrees of turbulence and aeration, and typically corresponds with high values of Y_c/h. The skimming regime is characterized in the upper part of the spillway chute by a clear-water flow region, which at some point downstream transitions into a rapidly-varied, aerated flow region. From here, with downstream distance air is continuously entrained into the water-column at the free-surface; consequently, the water surface bulks as the volume of entrained air increases. The rapidly-varied region then transitions to a gradually-varied region. Eventually, if the chute is sufficiently long, a state of equilibrium aeration is attained.

The channel invert of a stepped spillway conveying skimming flow is represented by a pseudo-bottom which adjoins each step at the risers' upper vertices (see Figure B.1). Flow glides down the chute as a 'coherent' stream atop the pseudo-bottom, though markedly turbulent and ruffled. Beneath the skimming stream, recirculating cavity flow is visible along the length of the chute where flow is aerated. The motion of the eddies within the step cavities is sustained by the transmission of shear stress from the flow passing overhead (Rajaratnam, 1990). Flow energy is

dissipated by momentum exchange between the skimming flow and cavity flow. Form losses contribute to additional flow energy dissipation.

The air-water mixture which typifies skimming flow has a distribution of entrained air which tends to increase consistently with depth over the pseudo-bottom ($Y = 0$). Above the water-column, the air concentration, i.e. vol. air / vol. total (water + air), approaches $C = 1.0$; while at $Y = 0$, the air concentration can be as low as $C = 0$, or as high as $C = 0.40$. Between $Y = 0$ and the flow depth where $C = 1.0$, the buoyant force exerted on entrained air bubbles is generally overpowered by the strong turbulence of the skimming flow; and with downstream distance, the flow turbulence mixes the entrained bubbles vertically: hence, in the non-equilibrium flow region, $\frac{d\bar{C}}{dx} > 0$, where x refers to the longitudinal axis of the spillway.

In the skimming flow regime, the water surface is defined relative to a characteristic flow depth corresponding with a prescribed level of air concentration. Typically, in skimming flows the water surface is defined as $Y_{0.90}$, i.e. $Y(C=0.90)$ (Wood, 1991).

Figure B.1 depicts a typical water-column of skimming flow. Above $Y_{0.90}$ the skimming flow consists of water droplets ejected beyond the free-surface by turbulent velocity fluctuations. Generally, the flow is irregular and visibly turbulent: the streamlines appear chaotic, and interplay between the regions of cavity flow and skimming flow is evident. Figure B.2 shows the longitudinal development of skimming flow along a stepped spillway. A region of clear-water flow is delimited from a region of aerated flow by the ‘Point of inception of air entrainment’, where the thickness of the (turbulent) boundary layer becomes equal with the flow depth, and consequently where the flow becomes sufficiently turbulent to overcome the effects of surface tension and buoyancy.

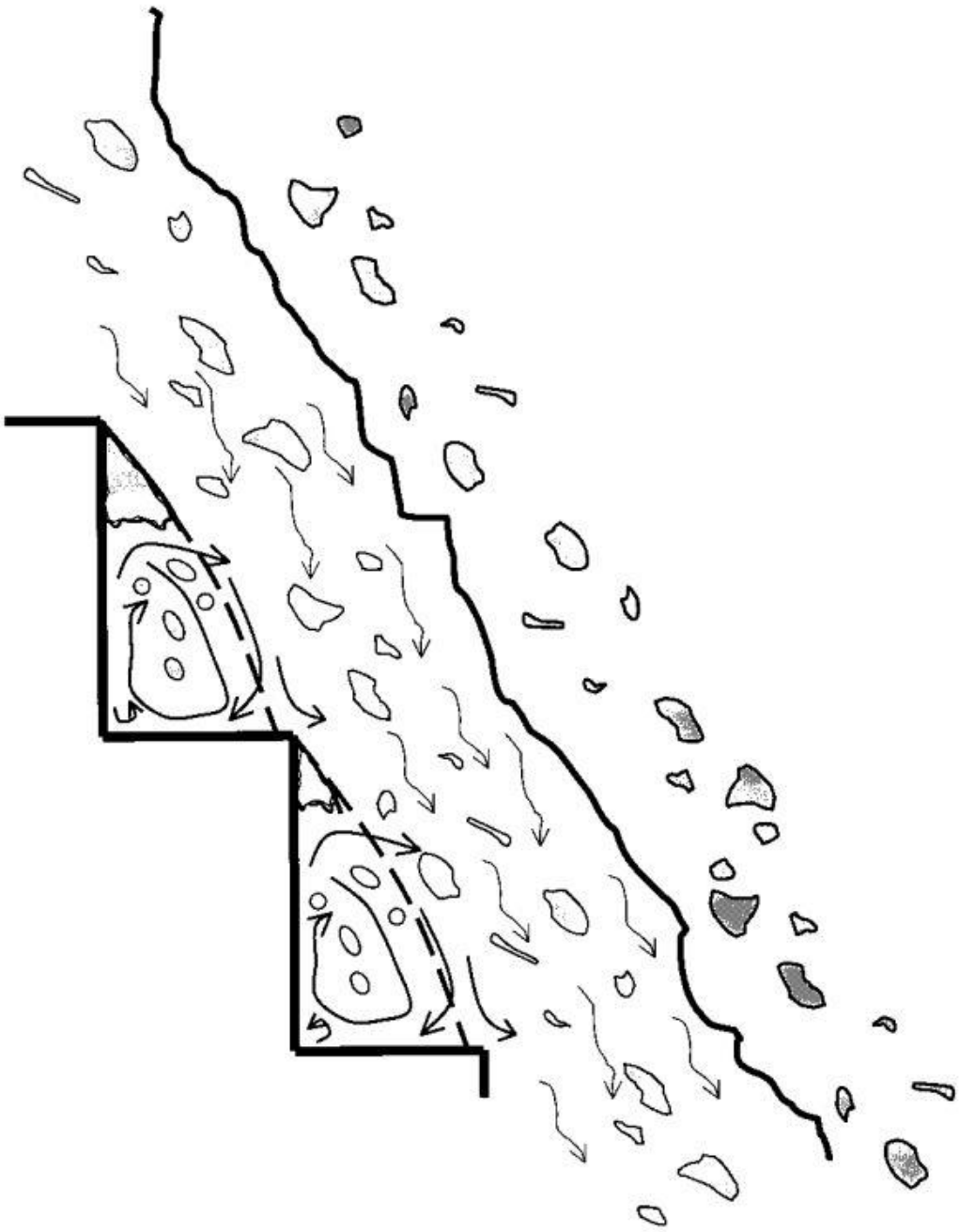

Figure B.1. A schematic of skimming flow along a stepped chute (Pegram et al., 1999)

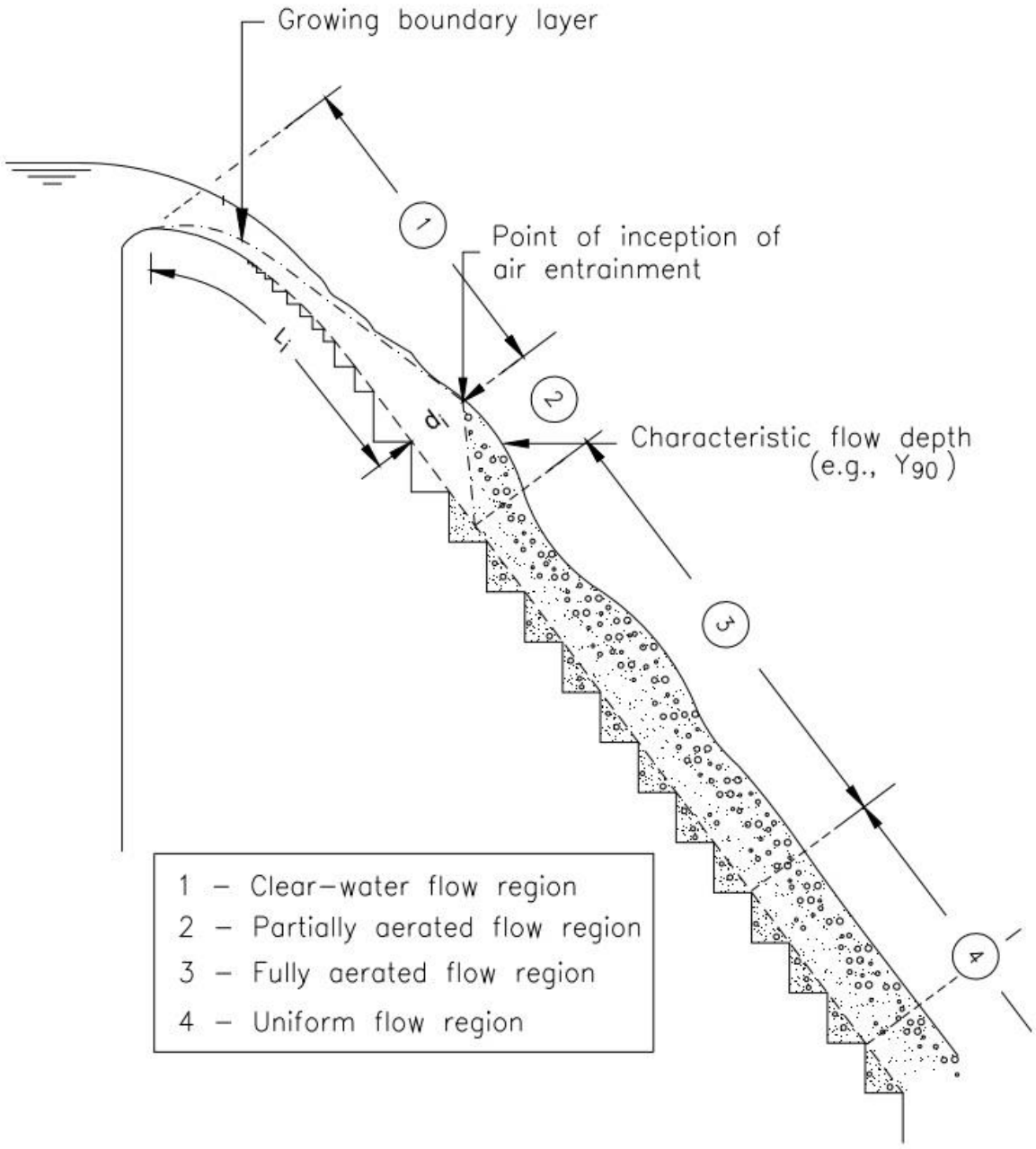

Figure B.2. A schematic of skimming flow regions along a stepped chute (Matos & Meireles, 2014).

B.2 Nappe Flow

The nappe flow regime is characterized by a series of free-falling jets which descend the stepped spillway in a succession of plunges, as shown in Figure B.3. At the interface of the jet and plunge pool, air is entrained into the flow and high amounts of turbulent mixing occurs. Flow energy is dissipated by the formation of miniature hydraulic jumps on the step treads (Rajaratnam, 1991).

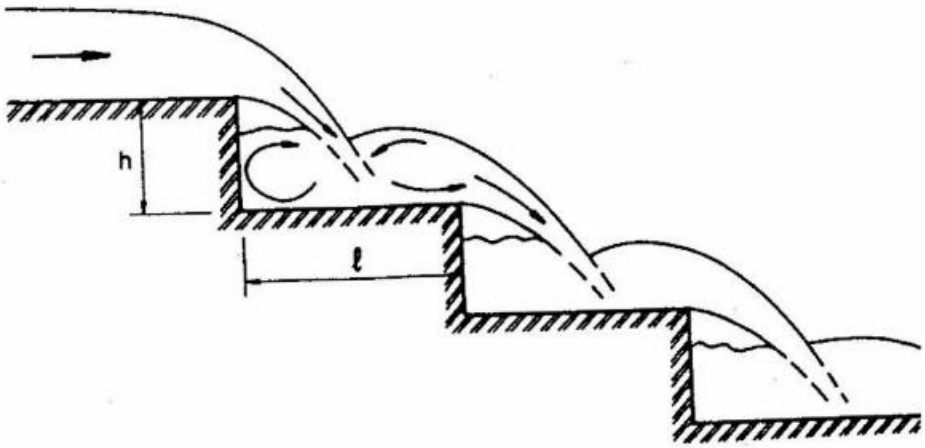

Figure B.3. A schematic of nappe flow along a stepped chute (Chanson, 1994).

If the depth of tail water on a step is greater than the critical flow depth, a fully-developed hydraulic jump forms on the step treads. In this condition, the regime is said to be isolated nappe flow. Between steps, the flow repeatedly transitions from a supercritical state within the nappe to a subcritical state in the tail water beyond the point of impingement. Before being ejected to the next step, the flow is critical near the drop. In the isolated nappe regime, the amount of energy dissipated by each plunge is equal to the step height, and hence the spillway dissipates nearly all flow energy (Peyras et al., 1992).

If the depth of tail water on a step is less than the critical flow depth, a hydraulic jump only partially forms, and the regime is hence termed partial nappe flow. As compared with isolated nappe flow, partial nappe flow is marked by a lesser degree of energy dissipation and the spanning of critical/supercritical flow conditions down the full length of the spillway chute (Peyras et al., 1992). In isolated nappe flow, energy dissipation is quantified in terms of residual energy at the end of the chute.

B.3 Transition Flow

Transition flow exhibits characteristics of both nappe and skimming flow simultaneously along the stepped spillway. At any given moment, in some step cavities the overfalling nappes enclose partially-formed pockets of air, hence appearing as nappe flow; while in other step cavities the entrained air begins to coalesce into eddies (Ohtsu & Yasuda, 1997). Through time, any given step is seen to alternate between being aerated and non-aerated, resulting in hydrodynamic instabilities which can generate wave action along the length of the spillway (Boes & Hager, 2003b; Chanson, 1994). For this reason, transition flow is generally to be avoided in the design and operation of a stepped spillway.

Appendix C OPERATION OF THE CONDUCTIVITY PROBE

C.1 Overview

The resistance of air is one thousand times larger than that of water (Chanson, 2004). Therefore, the conductivity probe, which is essentially a bubble detector, registers the flow's instantaneous void fraction (water or air) by measuring the probe's resistance (in terms of voltage) through time. The probe has a dual tip design, and each tip acts as an independent bubble detector. The upstream tip (leading sensor) is offset by 7.0 mm from the downstream tip (trailing sensor). A sample of a flowing, air-water mixture produces two time-series records of voltage, as Figure C.1 shows. Each voltage record is characterized by sharp (nearly vertical) fronts which indicate changes in the void fraction between high voltage outputs (water) and low voltage outputs (air). (In this example plot, the trailing sensor has been shifted vertically by -2.0 Volts to make the two time-series records more distinguishable; typically, the measured outputs both range from 0 – 4.0 Volts if the GAIN setting has been properly configured).

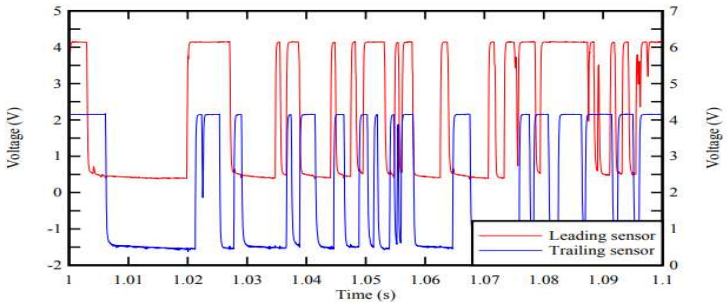

Figure C.1. Example time series of the probe's voltage outputs

Values of air concentration are determined for each probe tip from the voltage time-series, by selecting a voltage threshold (T) to delimit water from air. Typically, if the range of voltage outputs is 0 – 4.0 Volts, then a threshold value halfway between the minimum and maximum outputs, about 2.0 Volts, works well. After selecting a voltage threshold for each of the voltage-output signals, the time series are binarized, resulting in a new function $B(t)$ for each voltage time series. This step converts the voltage time series into a binary time series, where for $V(t) > T \rightarrow B(t) = 0$, and for $V(t) < T \rightarrow B(t) = 1$. Finally, mean values of air concentration are determined across the sample duration, for each tip, by taking the arithmetic mean of each function $B(t)$.

A single value of bulk-flow velocity is determined from the two voltage time-series outputs by performing a cross-correlation analysis. For an idealized (not highly turbulent) case of air-water flow, the two probe tips offset in the streamwise direction should both detect the same sequence of bubbles. In that case, the two time-series records of voltage should be offset along the abscissa by Δt = 7.0 mm / V, where V is the bulk-flow velocity we wish to determine. The mean travel time of the bubble sequence, Δt, is determined from a cross-correlation function which computes a sliding dot product on the two time-series records of voltage. The value Δt which maximizes the cross-correlation function is the mean travel time, from which the bulk-flow velocity is calculated as V = 7.0 mm / Δt.

A MATLAB script is used to automate the tasks of computing a voltage threshold and binarizing the voltage time-series records to determine values of air concentration; and computing the cross-correlation function to determine bulk-flow velocity.

C.2 Probe Setup

The conductivity probe (Figure C.2) connects into the front face of the electronics box (Figure C.5) according to the instructions on the cable tag (Figures C.3 and 4). The grounding wire can be plugged into the top face of the electronics package, in the location indicated in Figure C.10 by a red circle. The electronics package is powered on the back side (Figure C.6) using the power cable (Figure C.7). The cables in Figure C.8 deliver probe outputs from the electronics package to a voltage data acquisition system (e.g., NI 9215, Figure C.9), and are plugged into the electronics package in the locations indicated by the blue, dashed lines in Figure C.10.

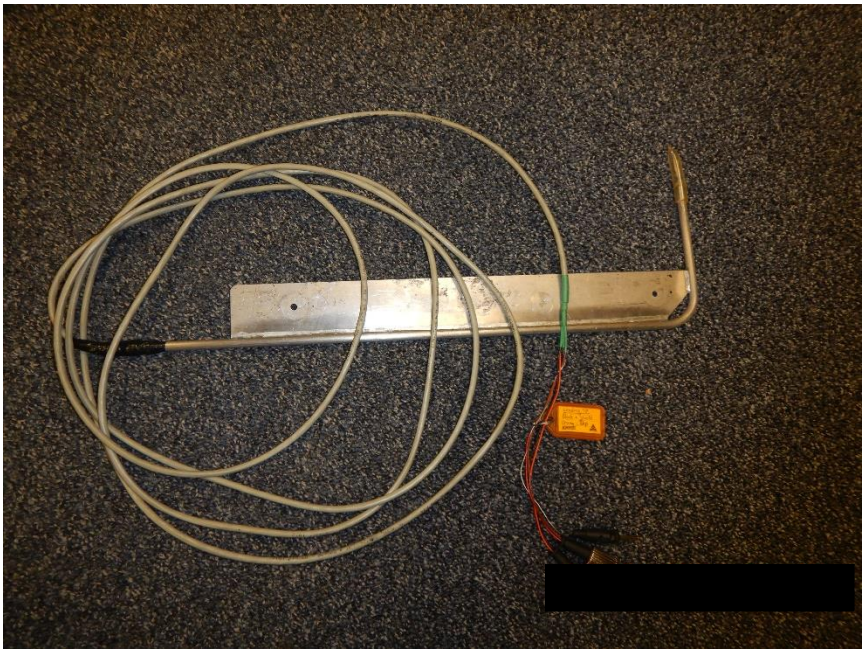

Figure C.2. The conductivity probe and cable, which terminate with 2 output connectors and 1 grounding wire

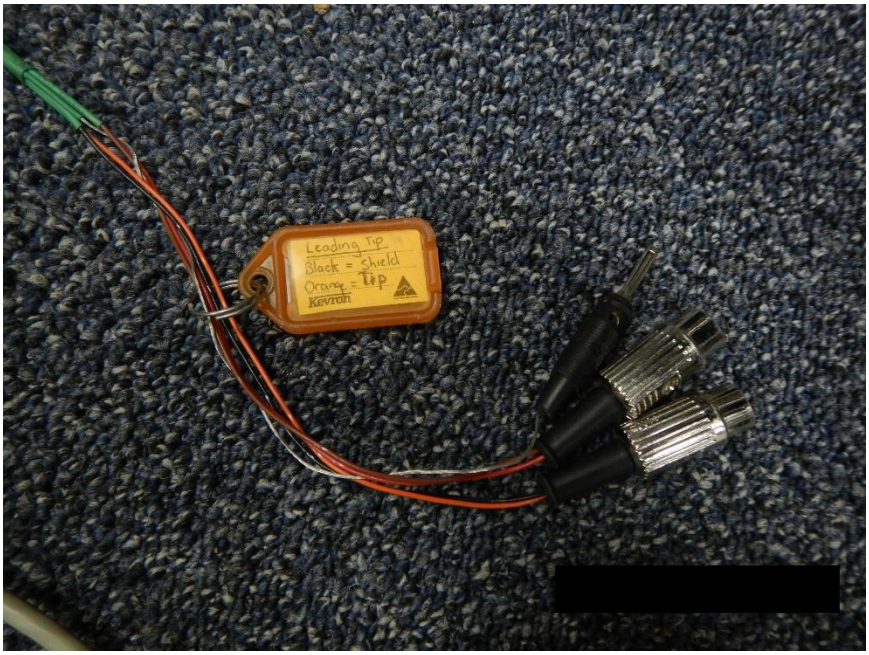

Figure C.3. A cable tag indicating the convention for the Leading Tip output of the probe / Leading Tip input to the electronics package: Leading Tip = Output Connector with Black & Orange wires

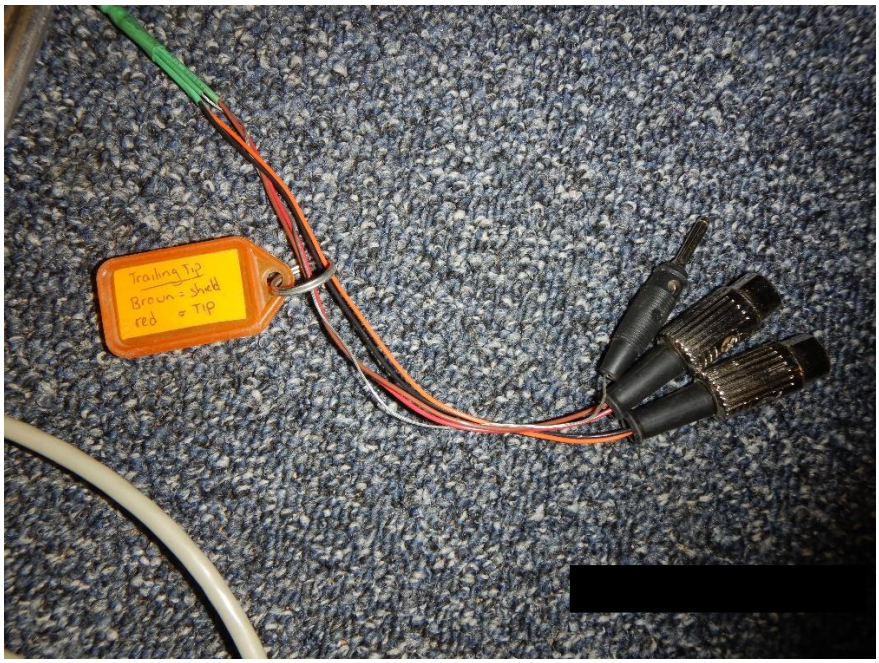

Figure C.4. A cable tag indicating the convention for the Trailing Tip output of the probe / Trailing Tip input to the electronics package: Trailing Tip = Output Connector with Brown & Red wires

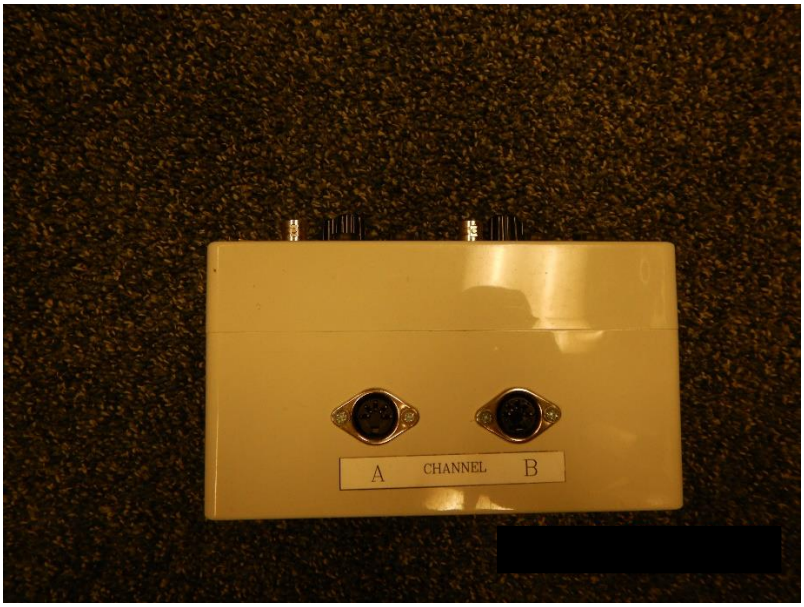

Figure C.5 A front-side view of the electronics package where probe inputs are inserted. Channel A = Leading Tip, Channel B = Trailing Tip

Figure C.6. The back side of the electronics package, where power is input

Figure C.7. The power cable for the electronics package

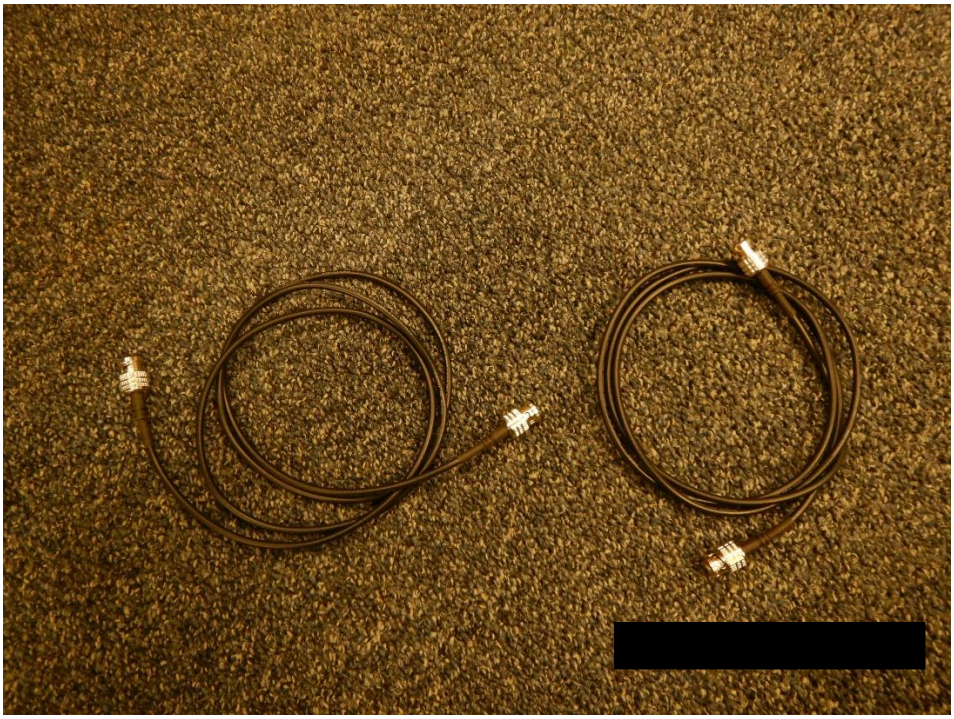

Figure C.8. The output cables for the electronics package which are input to the data acquisition system (DAQ)

Figure C.9. NI 9215, a voltage DAQ used to receive outputs from electronics package

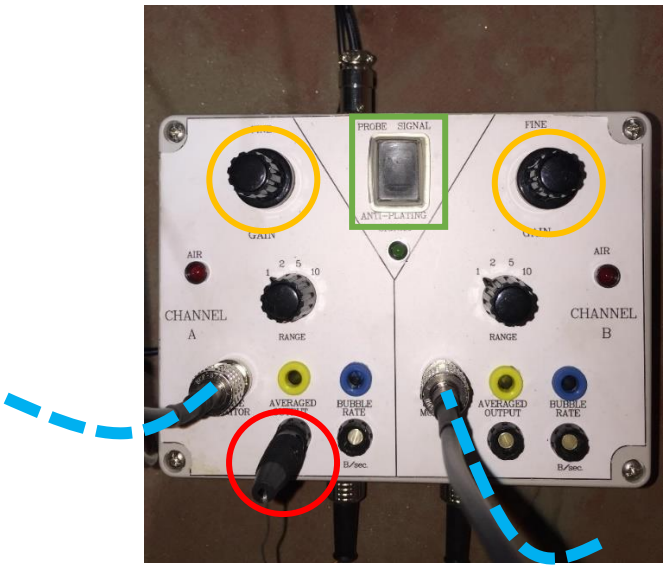

Figure C.10. A top view of the electronics package control module

The GAIN knobs (yellow circles in Figure C.10) stretch the signal outputs vertically to enunciate voltage peaks/troughs while preserving values along the x-axis (time). With the GAIN knobs set to zero (anticlockwise), probe outputs are of the order of millivolts. Prior to collecting data sets, each GAIN knob should be adjusted while the probe is submerged in an aerated flow, and while the probe outputs are being displayed in real time. The GAIN knobs should be turned clockwise until the peaks are 'chopped' at 4.0 Volts. After that initial configuration has been set, the GAIN knobs should be left alone until sampling has concluded, or until, after long use, the probe signal begins to decay. Then, the anti-plating switch (green rectangle in Figure C.10) can be flipped on/off for a few moments, before the GAIN knob is re-configured to the proper setting. The RANGE control should be set to the 1st setting.

C.3 Data Collection

A LabView-project file (courtesy of Stefan Felder of UQ, acquired by Taylor Hogan of CSU) processes the probe's signal output and generates a binary output file. The program interface is shown in Figure C.11. After the DAQ has been connected by USB to the computer, the channel inputs are selected in (1). Then, the sampling frequency is prescribed in (2) in units of Hz. For the Gross Dam spillway chute, a frequency of 60,000 Hz was found to be more than adequate. In (3), the sampling duration is set. For this work, data were recorded for 30.0 or 60.0 sec. Near the top, lever (4) toggles between the 'Acquire data' and 'Show signal' modes.

Data collection and/or display of real-time data (for GAIN adjustments) are initiated along the top toolbar:

- If (4) is set to 'Acquire data', then selecting (5) prompts the user to input a file name, after which the program records a single sample for the prescribed duration, and stops. The time series is then displayed in window (7), with statistics given in (8). Selecting (6) also prompts the user to input a file name. However, (6) will record data on a loop, such that after the first sample has been recorded the user is automatically prompted to input the next file name.

- If (4) is set to ‘Show signal’, then only (6) can be selected. Selecting (6) causes the voltage data to be displayed in real time in window (7), which is useful when dialing in the GAIN setting so that the peaks are ‘chopped’ at 4.0 Volts.

The output files of the LabView program are in binary format and must be converted in .txt files using a Python script file, “Parse.py”.

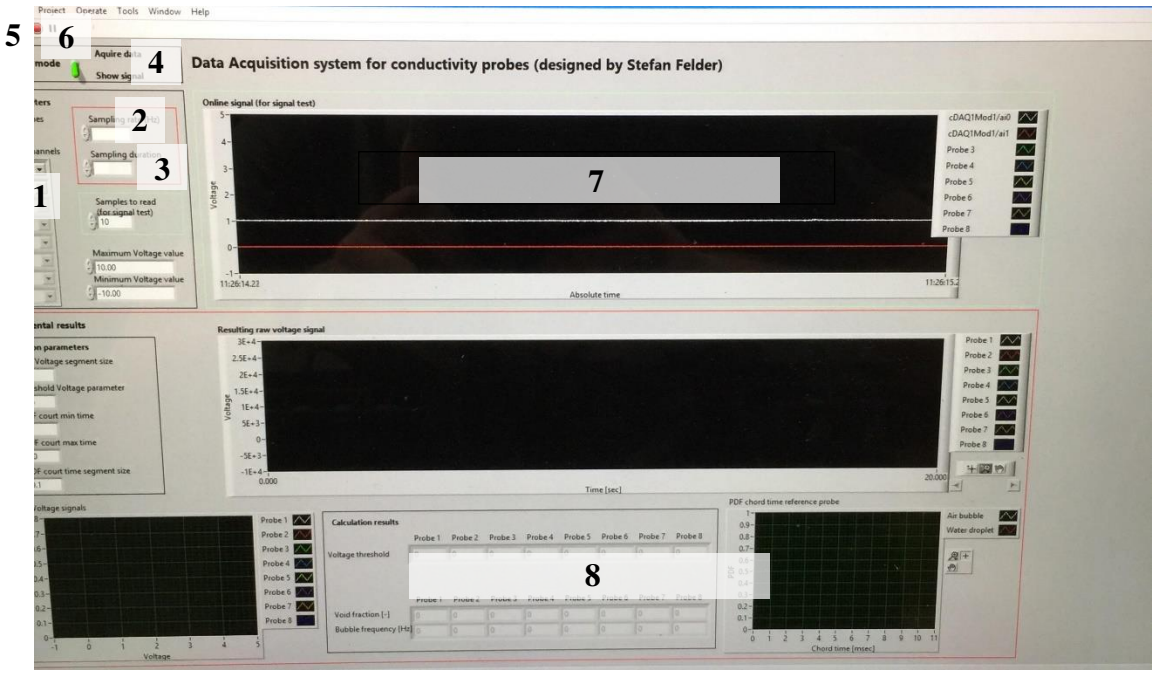

Figure C.11. LabView project file for data acquisition.

C.4 Data Conversion

After binary files have been generated by the LabView program, they can be converted in .txt files using the “Parse.py” file. First, place the “Parse.py” file within the same file directory as the binary file(s) to be converted (Figure C.12). *Note:* The file directory should contain no spaces – use underscores. Before executing the following commands, the “Parse.py” file should be opened in NotePad++, and line 7 should be edited so that ‘*fsamp’* matches the value prescribed in the LabView project file (see (2) of Figure C.11).

Within the file pathway containing the “Parse.py” and binary files, type ‘*cmd’* (Figure C.13). A command prompt will appear (Figure C.14). Then, follow the steps indicated in Figures C.15 and

C.16. After pressing ‘Enter’, the Python script will convert each binary file within the specified directory into a .txt file. All outputs are saved into that same directory.

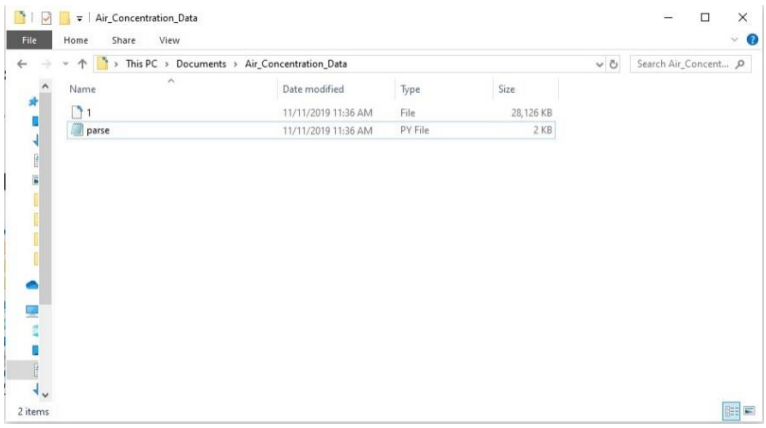

Figure C.12. Binary and ‘Parse.py’ files located in the same file directory

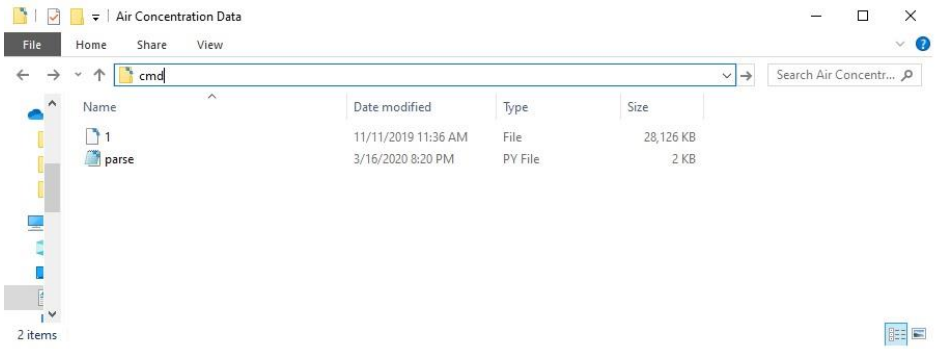

Figure C.13. Initiate ‘*cmd’* command within the file-directory pathway

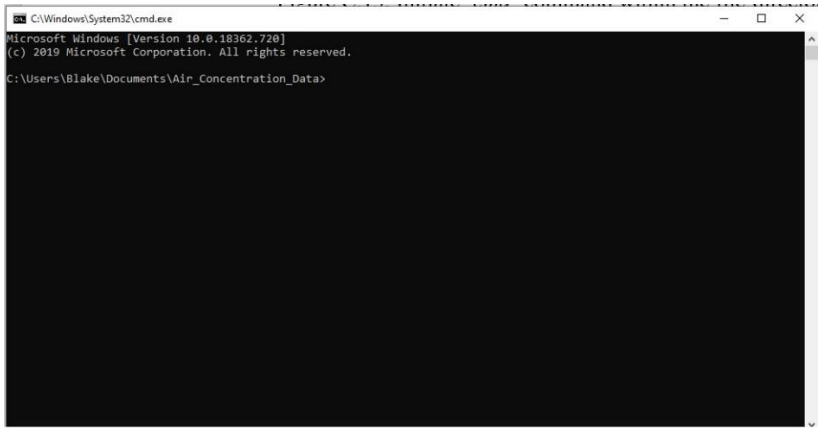

Figure C.14. A command prompt appears

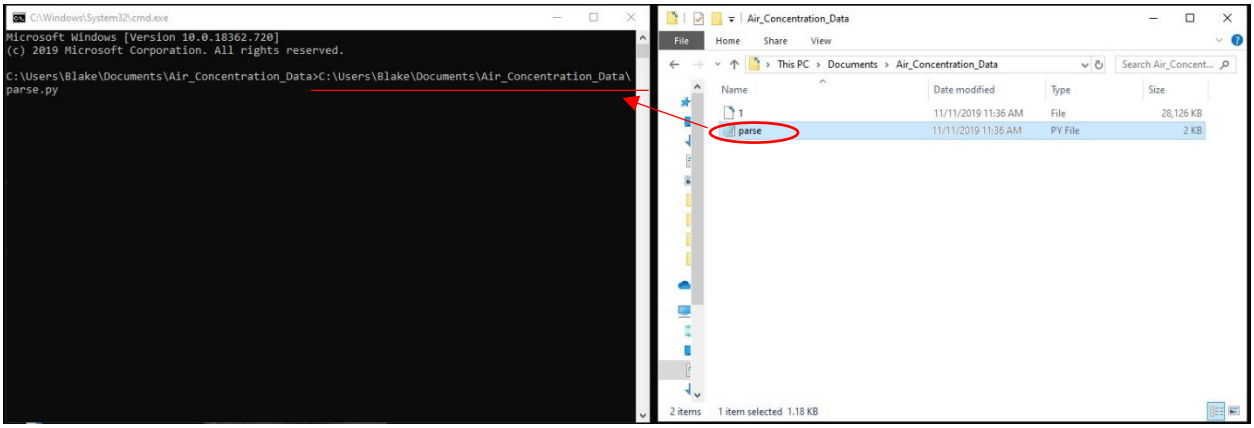

Figure C.15. Drag "Parse.py" file into the '*cmd'* prompt

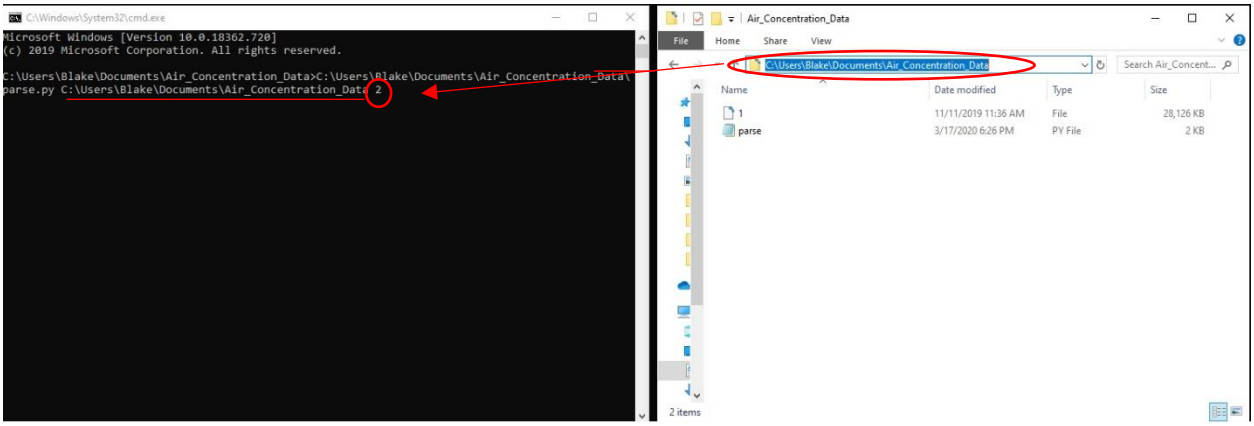

Figure C.16. Place a space after the "Parse.py" entry. Copy the folder directory containing the "Parse.py" and binary file, paste it after the space, followed by an additional space, and '2'.

C.5 Data Processing

The converted .txt file contains three columns of data. The first column represents time, and the second and third columns are the voltage data for the leading and trailing tips, respectively. To process the voltage data using a thresholding technique in the manner previously described, a *for* loop can be implemented after reading the time and voltage data into MATLAB arrays; e.g.:

```
clc; clear all;
FolderAddress = '    ';    % The address of Raw data folder
A = dir([FolderAddress '\*txt']);   % File extension to be read, .txt
LL = length(A);   % Number of files to be converted
ii = 1;
b = A(ii);
c = [FolderAddress '\' b.name];
FileID = fopen(c);
data = textscan(FileID, '%f %f %f', 'headerlines', 1);
fclose(FileID);
T = data{1};
V_l = data{2};    % Read leading tip data
V_t = data{3};    % Read trailing tip data
threshold_l=0.5*(min(V_l)+max(V_l));    % Compute the leading tip voltage threshold
threshold_t=0.5*(min(V_t)+max(V_t));    % Compute the trailing tip voltage threshold


for i=1:length(V_l)        %
   if V_l(i)<threshold_l
       B_l(i)=1;
   else B_l(i)=0;
   end
   if V_t(i)<threshold_t
       B_t(i)=1;
   else B_t(i)=1;
   end
   i=i+1;
end

C_l=mean(B_l)
C_t=mean(B_t)
```

To calculate the bulk-flow velocity, the value Δt which maximizes the cross-correlation of the two voltage signals can be solved for in MATLAB using the `xcorr` function with inputs of `V_l` and `V_t`.

LIST OF UNITS AND ABBREVIATIONS

Unit Abbreviations

cm	centimeter
cms	cubic meters per second
hp	horsepower
Hz	hertz
kHz	kilo hertz
m	meter
rpm	rounds per minute
s	second

General Abbreviations

AECOM	the name of an engineering company
ASCE	American Society of Civil Engineers
CSU	Colorado State University
CVC	conventionally vibrated concrete
GRE	Gross Reservoir Expansion
PMF	probable maximum flood
RCC	roller compacted concrete
USBR	U.S. Bureau of Reclamation
V:H	the ratio of vertical to horizonal step dimensions